

8-1-2012

# Image reconstruction and imaging configuration optimization with a novel nanotechnology enabled breast tomosynthesis multi-beam X-ray system

Weihua Zhou

*Southern Illinois University Carbondale*, arayzhou@gmail.com

Follow this and additional works at: <http://opensiuc.lib.siu.edu/dissertations>

---

## Recommended Citation

Zhou, Weihua, "Image reconstruction and imaging configuration optimization with a novel nanotechnology enabled breast tomosynthesis multi-beam X-ray system" (2012). *Dissertations*. Paper 540.

This Open Access Dissertation is brought to you for free and open access by the Theses and Dissertations at OpenSIUC. It has been accepted for inclusion in Dissertations by an authorized administrator of OpenSIUC. For more information, please contact [opensiuc@lib.siu.edu](mailto:opensiuc@lib.siu.edu).

IMAGE RECONSTRUCTION AND IMAGING CONFIGURATION OPTIMIZATION WITH  
A NOVEL NANOTECHNOLOGY ENABLED BREAST TOMOSYNTHESIS  
MULTI-BEAM X-RAY SYSTEM

by

Weihua Zhou

Ph.D., Southern Illinois University, 2012

A Dissertation  
Submitted in Partial Fulfillment of the Requirements for the  
Doctor of Philosophy

Department of Electrical and Computer Engineering  
in the Graduate School  
Southern Illinois University Carbondale  
August 2012

DISSERTATION APPROVAL

IMAGE RECONSTRUCTION AND IMAGING CONFIGURATION OPTIMIZATION WITH  
A NOVEL NANOTECHNOLOGY ENABLED BREAST TOMOSYNTHESIS  
MULTI-BEAM X-RAY SYSTEM

by

Weihua Zhou

A Dissertation Submitted in Partial

Fulfillment of the Requirements

for the Degree of

PhD.

in the field of Electrical and Computer Engineering

Approved by:

Ying Chen, Chair

Nazeih Botros

Gupta Lalit

Ramanarayanan Viswanathan

Mengxia Zhu

Graduate School  
Southern Illinois University Carbondale  
March 8<sup>th</sup>, 2012

## AN ABSTRACT OF THE DISSERTATION OF

Weihua Zhou, for the Doctor of Philosophy degree in ELECTRICAL AND COMPUTER ENGINEERING, presented on March 8<sup>th</sup>, 2012, at Southern Illinois University Carbondale.

TITLE: IMAGE RECONSTRUCTION AND IMAGING CONFIGURATION OPTIMIZATION WITH A NOVEL NANOTECHNOLOGY ENABLED BREAST TOMOSYNTHESIS MULTI-BEAM X-RAY SYSTEM

MAJOR PROFESSOR: Dr. Ying Chen

Digital breast tomosynthesis is a new technology that provides three-dimensional information of the breast and makes it possible to distinguish the cancer from overlying breast tissues. We are dedicated to optimizing image reconstruction and imaging configuration for a new multi-beam parallel digital breast tomosynthesis prototype system.

Several commonly used algorithms from the typical image reconstruction models which were used for iso-centric tomosynthesis systems were investigated for our multi-beam parallel tomosynthesis imaging system. The representative algorithms, including back-projection (BP), filtered back-projection (FBP), matrix inversion tomosynthesis reconstruction (MITS), maximum likelihood expectation maximization (MLEM), ordered-subset maximum likelihood expectation maximization (OS-MLEM), simultaneous algebraic reconstruction technique (SART), were implemented to fit our system design. An accelerated MLEM algorithm was proposed, which significantly reduced the running time but had the same image quality. Furthermore, two statistical variants of BP reconstruction were validated for our tomosynthesis prototype system. Experiments based on phantoms and computer simulations show that the prototype system

combined with our algorithms is capable of providing three-dimensional information of the objects with good image quality and has great potentials to improve digital breast tomosynthesis technology.

Four methodologies were employed to optimize the reconstruction algorithms and different imaging configurations for the prototype system. A linear tomosynthesis imaging analysis tool was used to investigate blurring-out reconstruction algorithms. Computer simulations of sphere and wire objects aimed at the performance of out-of-plane artifact removal. A frequency-domain-based methodology, relative NEQ(f) analysis, was investigated to evaluate the overall system performance based on the propagation of signal and noise. Conclusions were made to determine the optimal image reconstruction algorithm and imaging configuration of this new multi-beam parallel digital breast tomosynthesis prototype system for better image quality and system performance.

## ABBREVIATIONS

CT: Computed Tomography

FEM: Finite Elements Modelling

ROI: Region Of Interest

BP: Back Projection

FBP: Filtered Back Projection

PCA: Principal Component Analysis

MITA: Matrix Inversion Tomosynthesis

MLEM: Maximum Likelihood Expectation Maximization

OS-MLEM: Ordered Subset – Maximum Likelihood Expectation Maximization

SART: Simultaneous Algebraic Reconstruction Technique

NP: Number of Projection Images

VA: View Angle

MTF: Modulation Transfer Function

NPS: Noise Power Spectrum

NEQ: Noise Equivalent Quantum

CNR: Contrast to Noise Ratio

SNR: Signal to Noise Ratio

## ACKNOWLEDGMENTS

During my Ph.D. study at Southern Illinois University Carbondale, I have been fortunate to meet many wonderful people who have directly or indirectly helped me in this project. I wish to take this opportunity to convey my appreciation to them.

I would like to thank my advisor Dr. Ying Chen, without whose help I would have never been able to finish what I have done today. Her guidance has been invaluable. I also thank many professors in Southern Illinois University Carbondale. I learned professional knowledge and skills from them.

I greatly appreciate my collaborators at the University of North Carolina. Dr. Otto Zhou and Dr. Xin Qian provided me great suggestions to conduct experiments and analyze the results. Andrew Tucker at North Carolina State University helped me acquire tomosynthesis datasets and adjust imaging configurations.

I would like to thank my wife, Dan and my daughter, Jacey. They bring great happiness to my life. My parents are here greatly supporting me.

Finally, I want to appreciate my friends, Jian Fang, Linlin Cong, Shiyu Xu, Apuroop Bella and many other students. With their help and encouragement, I could have enjoyed my four years of life in Carbondale.

Note: This work was supported by NIH/NCI R01 CA134598-01A1.

## TABLE OF CONTENTS

<u>CHAPTER</u>	<u>PAGE</u>
ABSTRACT .....	i
ABBREVIATIONS .....	iii
ACKNOWLEDGMENTS.....	iv
LIST OF TABLES.....	viii
LIST OF FIGURES.....	ix
CHAPTERS	
CHAPTER 1 – Introduction.....	1
1.1. Clinical motivation .....	2
1.2. Current technology of breast cancer detection .....	4
1.3. History of tomosynthesis .....	7
1.4. Current state of digital breast tomosynthesis .....	8
1.5. System design of digital breast tomosynthesis imaging systems .....	9
1.5.1. Current DBT prototype systems .....	11
1.5.2. A novel multi-beam parallel digital breast tomosynthesis prototype system .....	14
1.6. Image quality assessment .....	16
CHAPTER 2 – Image reconstruction algorithms for a multi-beam parallel digital breast tomosynthesis system .....	18
2.1. Back Projection (BP) .....	21
2.1.1. Point-by-point BP .....	21
2.1.2. Ray-tracing BP .....	23

2.2. Filtered back-projection (FBP) .....	23
2.2.1. Radon transform, Fourier-slice theorem and 2D parallel-beam filtered back projection .....	24
2.2.2. Implementation of FBP for a multi-beam parallel digital breast tomosynthesis system .....	28
2.3. Matrix inversion tomosynthesis algorithm (MITS) .....	29
2.4. Statistical iterative reconstruction algorithms .....	30
2.4.1. Maximum likelihood expectation maximization (MLEM) .....	32
2.4.2. Ordered-subset MLEM (OS-MLEM) .....	40
2.5. Algebraic iterative reconstruction algorithms.....	41
2.5.1. Linear attenuation equations .....	41
2.5.2. Simultaneous algebraic reconstruction technique (SART) .....	42
2.6. Validity of ray-tracing-based reconstruction algorithms.....	43
2.7. Image reconstruction with an ACR training phantom .....	44
2.8. Image reconstruction with a breast biopsy training phantom .....	47
CHAPTER 3 – Statistical variants of point-by-point back-projection reconstruction algorithm .....	54
3.1. Statistical variants of point-by-point back-projection algorithm .....	54
3.2. Image reconstruction with a breast biopsy training phantom .....	55
3.3. Sphere simulation experiment .....	57
3.4. NPS measurement .....	60
3.5. MTF measurement .....	61
3.6. Summary .....	62

CHAPTER 4 – Optimization of image reconstruction and imaging configuration for a multi-beam parallel digital breast tomosynthesis system	64
4.1. Linear tomosynthesis imaging analysis	66
4.2. Sphere simulation	74
4.3. Wire simulation	82
CHAPTER 5 – Relative NEQ (f) analysis of a multi-beam parallel digital breast tomosynthesis system	90
5.1. MTF	91
5.1.1. Projection MTF(f)	92
5.1.2. Reconstruction MTF(f)	93
5.2. NPS	95
5.3. Relative NEQ(f) analysis	97
5.3.1. Relative NEQ(f) analysis for different reconstruction algorithms	98
5.3.2. Relative NEQ(f) analysis for different imaging configurations	102
CHAPTER 6 – Conclusions	108
REFERENCES	110
VITA	120

## LIST OF TABLES

<u>TABLE</u>	<u>PAGE</u>
Table 1 .....	3
Table 2 .....	13
Table 3 .....	40

## LIST OF FIGURES

<u>FIGURE</u>	<u>PAGE</u>
Figure 1 .....	12
Figure 2 .....	12
Figure 3 .....	14
Figure 4 .....	15
Figure 5 .....	15
Figure 6 .....	22
Figure 7 .....	26
Figure 8 .....	26
Figure 9 .....	27
Figure 10 .....	29
Figure 11 .....	34
Figure 12 .....	36
Figure 13 .....	37
Figure 14 .....	39
Figure 15 .....	39
Figure 16 .....	44
Figure 17 .....	45
Figure 18 .....	46
Figure 19 .....	48
Figure 20 .....	49
Figure 21 .....	50
Figure 22 .....	50

Figure 23 .....	51
Figure 24 .....	53
Figure 25 .....	56
Figure 26 .....	56
Figure 27 .....	59
Figure 28 .....	59
Figure 29 .....	59
Figure 30 .....	61
Figure 31 .....	62
Figure 32 .....	68
Figure 33 .....	71
Figure 34 .....	72
Figure 35 .....	73
Figure 36 .....	73
Figure 37 .....	75
Figure 38 .....	77
Figure 39 .....	78
Figure 40 .....	79
Figure 41 .....	80
Figure 42 .....	81
Figure 43 .....	83
Figure 44 .....	84
Figure 45 .....	85

Figure 46 .....	86
Figure 47 .....	87
Figure 48 .....	88
Figure 49 .....	91
Figure 50 .....	92
Figure 51 .....	94
Figure 52 .....	94
Figure 53 .....	95
Figure 54 .....	97
Figure 55 .....	99
Figure 56 .....	101
Figure 57 .....	103
Figure 58 .....	104
Figure 59 .....	105
Figure 60 .....	106
Figure 61 .....	107

# CHAPTER 1

## INTRODUCTION

Breast cancer is the most prevalent cancer and the second leading cause of cancer-related death in women in the United States (Kopans 1997). Early detection of breast cancer is viewed as the best hope to decrease breast cancer mortality (Kopans 1997). It is universally accepted that mammography is the most effective tool for the early detection of breast cancer (Bassett et al 2005). However, the appearance of overlapping tissue on mammograms brings difficulties to interpret the images. It is particularly difficult for mammography to interpret dense breast tissues, which is common in young women (Holland et al 1982). When suspicious finding appears on the screening mammograms, the follow-up diagnostic mammography, ultrasonography, magnetic resonance imaging (MRI), or biopsy will be conducted to determinate the final diagnosis. This procedure causes anxiety and increases medical cost.

Improving breast imaging technologies may permit breast cancer to be detected at a smaller size and earlier stage, thereby reducing the number of women who die from such cancer. Compared to the standard mammography technique, digital breast tomosynthesis (DBT) enhances the diagnosis by removing the ambiguities of overlapping tissues and providing the depth information. Therefore, it is promising to reduce recall rates, improve the biopsy selection of patients, and increase cancer detection accuracy (Park et al 2007).

Extensive attention from academic communities and industrial vendors has been paid to this promising field. The typical breast tomosynthesis prototype systems acquire projection images with the X-ray tube moving along an arc path. This kind of

implementation can reutilize the traditional mammography design, decrease the cost and reduce the training procedure for the operators. However, the X-ray tube's movement may introduce motion blur to tomosynthesis images as well as cause patients' discomfort.

A novel nanotechnology enabled X-ray source, Invented by Zhou et al, has been investigated for breast tomosynthesis applications (Yang et al 2008, Zhou et al 2010). The breast tomosynthesis system is built up with fixed multi-beam field-emission X-ray (MBFEX) sources based on unique properties of carbon nano-tube electron emitters. It shows great potentials to reduce patients' discomfort and the motion blur associated with X-ray tube's movement in typical digital breast tomosynthesis systems.

In this chapter, we firstly introduce the clinical motivation and current technologies of breast cancer detection, and then discuss about the history and the state of arts in digital breast tomosynthesis development. At last, system design and image quality assessment of digital breast tomosynthesis systems are introduced.

## 1.1. CLINICAL MOTIVATION

Breast cancer accounts for 30 percent of all female cancers in USA and approximately 1 in 9 women in USA gets breast cancer during their lifetime (Kopans 1997). Around one million women worldwide are affected by this cancer. The report from NIH/NCI (National Cancer Institute 2012) estimates that in United States in 2012, there will be 226,870 new female cases and 2,190 new male cases, and 39,510 women and 410 men will die from such cancer.

The risk of developing breast cancer increases as the woman gets older. Table 1 shows the trend of different ages.

Table 1. A woman's chance of being diagnosed with breast cancer (Altekruse et al 2010).

Ages	A woman's chance of being diagnosed with breast cancer
from age 30 through age 39	1 in 233
from age 40 through age 49	1 in 69
from age 50 through age 59	1 in 42
from age 60 through age 69	1 in 29

Early breast cancer usually does not cause symptoms. This is why regular breast exams are important. As the cancer grows, symptoms may appear, including lump, change in the size and shape, fluid coming from the nipple. The doctor will ask the patients about the symptoms and risk factors, and then perform a physical exam. If the doctor learns that the patient does have breast cancer, staging tests will be done to see if the cancer has spread.

Breast cancer stages range from 0 to IV (BreastCancer.org 2012). How well the patient does after being treated for breast cancer depends on many factors. The more advanced the cancer, the poorer the outcome. For women with stage I, II, or III breast cancer, the main goal is to treat the cancer and prevent it from returning. For women with stage IV cancer, the goal is to improve symptoms and help them live longer. In most cases, stage IV breast cancer cannot be cured.

The 5-year survival rate refers to the number of patients who live at least 5 years after their cancer is found. According to the report (American Cancer Society 2012a), the 5-year survival rates for persons with breast cancer who are appropriately treated are as follows: (1) 93% for Stage 0; (2) 88% for Stage I; (3) 81% for Stage IIA; (4) 74%

for Stage IIB; (5) 67% for Stage IIIA; (6) 41% for Stage IIIB; (7) 49% for Stage IIIC; (7) 15% for Stage IV. Breast cancer is more easily treated and often curable if it is found early.

## 1.2. CURRENT TECHNOLOGY OF BREAST CANCER DETECTION

### **Mammography**

Mammography is an X-ray screening and diagnostic technique that is used to create detailed images of the breast. A mammogram can often show a lump before it can be felt. They also can reveal clusters of tiny specks of calcium. Due to the cost effectiveness and its ability to reduce breast cancer mortality, Mammography is the most widely used breast cancer screening tool (Pisano et al 2004).

The breast is pulled away from the body, compressed, and held between two glass plates to ensure that the whole breast is viewed. The appearance of a female breast on a mammogram varies due to the differences in X-ray attenuation in the relative amounts of fat, connective and epithelial tissue (Kopans 1997). Fat appears radiolucent or dark on a mammogram while epithelial and connective tissues are radiographically dense and appear lighter or white in the developed image. Some relevant findings in a mammogram include (Highnam and Brady 1999):

**Soft-tissue lesions** These are recognized as a mass or an architectural distortion. A mass is often defined as a region of increased density usually with a distinct edge, which makes it distinguishable from the surrounding breast tissue. Architectural distortions are irregular breast patterns caused by abnormal tissue.

**Micro-calcifications** These are seen as small calcium deposits in the breast tissue.

They can typically build up in clusters. Depending on their number in a cluster and the overall shape of the cluster they may increase a possible risk of breast cancer.

Mammograms are very good breast cancer detection technology, but they have some significant limitations (Park et al 2009): (1) The compression of the breast during mammography examination can be uncomfortable. (2) The overlapping of the breast tissues in 2D imaging brings difficulty to interpret the mammograms. A breast cancer can be hidden in the overlapping tissue and not show up on the mammogram.

### **Digital Breast Tomosynthesis**

Digital breast tomosynthesis is an emerging technology for early breast cancer detection (Park et al 2007). It creates 3-dimensional slice images of the breast using X-ray imaging and image reconstruction algorithms. Digital breast tomosynthesis acquires multiple x-ray projection images of each breast from limited angles. The breast is positioned the same way as it is in a conventional mammogram, but only much less pressure is applied. A few projection images are acquired during an examination and then sent to a computer, where they are assembled to produce focused 3-dimensional images throughout the breast.

Tomosynthesis may allow doctors to detect smaller lesions or ones that would otherwise be hidden with standard mammograms. Researchers believe that this new breast imaging technique will make breast cancers easier to be diagnosed in dense breast tissue and make breast screening more comfortable (Park et al 2007). Results show digital tomosynthesis is promising to replace the current digital breast

mammography. A commercially available DBT system has been approved by USA FDA (Hologic 2012).

### **Breast Ultrasound**

Ultrasound has become a valuable tool to use along with mammograms because it is widely available, non-invasive, and less expensive than other options. However, the effectiveness of an ultrasound test depends on the operator's level of skill and experience.

Breast ultrasound is sometimes used to evaluate breast problems that are found during a screening or diagnostic mammogram or on physical exam (Radiological Society of North America 2012a). It is not routinely used for screening. Some studies have suggested that ultrasound may be a helpful addition to mammography when screening women with dense breast tissue, which is hard to evaluate with a mammogram.

### **Biopsy**

The only definite method of determining the malignancy of the breast tissue is by a biopsy (American Cancer Society 2012b). The breast biopsy involves removing the tissue sample surgically or with a less-invasive needle core sampling procedure, to determine whether it is cancerous or benign. Most biopsy methods rely on image guidance to help the radiologist or breast surgeon precisely locate the lesion or abnormality within the breast.

### **Magnetic Resonance Imaging (MRI)**

MRI is more expensive than mammography. Breast MRI (Radiological Society of North America 2012b) is not generally recommended as a screening tool by itself,

because although it is a sensitive test, it may still miss some cancers that mammograms would detect. MRI may also be used in other situations, such as to better examine suspicious areas found by a mammogram. MRI can also be used in women who have already been diagnosed with breast cancer to better determine the actual size of the cancer and to look for any other cancers in the breast.

### 1.3. HISTORY OF TOMOSYNTHESIS

Tomosynthesis and computed tomography (CT) belong to the technology of tomographic imaging, which demonstrates important features over conventional projection radiography (Dobbins et al 2003). The tomographic imaging technology enables three-dimensional reconstruction of objects with depth resolution. It improves conspicuity of structures by removing the ambiguities caused by overlapping tissues.

The tomosynthesis technology can be traced back to the work of Radon (Radon 1917), in which mathematic transform was provided to acquire the internal structure of an object from its projection data. Ziedses des Plantes in 1932 stated a method of forming tomography by summing up a set of different projections of the object (Ziedses 1932). Ziedses des Plantes's work started the practical reconstruction of an arbitrary number of slices based on a series of acquired projection images (Dobbins et al 2003). At least in theory, it was possible to generate many tomographic scans from a single, low-dose acquisition procedure.

In 1972, Grant published evidence of a prototype 3D image projector, the first based upon circular image acquisition geometry (Grant 1972). Grant also proposed the term "tomosynthesis", referring to the ability to retroactively create an infinite number of arbitrary tomograms.

In the late 1990s, tomosynthesis research was reignited as a result of several technological advancements (Dobbins et al 2003): the invention of digital flat-panel detectors which are capable of producing high-quality digital images with rapid readout rates; and the high-performance computation which enables tomosynthesis reconstruction and image processing. Digital tomosynthesis has been investigated and applied to various medical imaging clinical applications, including chest imaging, joint imaging, dental imaging, head imaging, breast imaging, etc (Dobbins 1990, Suryanaryannan et al 1999, Warp et al. 2000, Badea et al 2001, Godfrey et al. 2003, Maidment et al 2006, Rakowski et al 2006, Bachar et al 2007, Mertelemeier et al 2007).

#### 1.4. CURRENT STATE OF DIGITAL BREAST TOMOSYNTHESIS

The 2D mammography technology has limitations due to overlapping tissue in the breast that may hide lesions (cancers) or cause benign masses to appear suspicious. DBT may be utilized along with full-field digital mammography (FFDM) in screening for breast cancer and may also be used as a technique for the diagnosis of breast cancer in helping to clarify equivocal mammographic findings (Blue Cross Blue Shield of Rhode Island 2012).

In evaluating DBT, studies must consider diagnosis accuracy (sensitivity and specificity) as well as recall rates (Siemens 2010). In addition, radiation exposure is also a very important consideration. The radiation dose of DBT is slightly higher than it would be with standard digital mammography (Park et al 2007).

It was reported that tomosynthesis can be combined with standard 2D breast imaging to provide a more complete scan. Tomosynthesis is better at spotting masses, while standard 2D imaging is quicker at spotting calcifications (Hayes 2012).

The study on tumor boundaries was conducted by researchers at Lund University in Malmö, Sweden, in cooperation with Siemens Medical Systems (Hayes 2012). It found that tomosynthesis and ultrasound could be used to find tumor volumes 84% and 83% of the time, respectively, in a set of 76 breast cancers. Standard digital mammography could be used to determine cancer outlines just 51% of the time. Breast tomosynthesis had the fewest number of tumors that could not be measured and tended to spot those not visible by ultrasound (Hayes 2012).

The researchers also looked at how the modalities compared on breast density and found that tomosynthesis was the best at showing tumor margins for all three categories (fatty, medium density, and high density). Digital mammography had a high percentage of measureable tumors for fatty breasts but lower levels for intermediate and high-density breasts. The opposite was true for ultrasound. (Hayes 2012)

Overall conclusions is that breast tomosynthesis is superior to 2D mammography in the preoperative staging of tumors.

### 1.5. SYSTEM DESIGN OF DIGITAL BREAST TOMOSYNTHESIS SYSTEMS

Although digital breast tomosynthesis imaging is very similar to CT, it is a very different technique. In CT, the source and the detector make a complete 360° rotation around the patient, obtaining a complete set of data from which images may be reconstructed. In digital tomosynthesis, only small rotation angles with a small number of discrete exposures are used. This incomplete set of data can be digitally processed to yield a series of slices at different depths and with different thicknesses which have with very good in-plane resolution but coarser Z-axis resolution (Wiki 2012).

In order to perform tomosynthesis, the detector has to be able to acquire high-resolution images at a relatively high read-out speed, while maintaining good imaging performance at a low dose per image. The current digital breast tomosynthesis can be considered as an extension to mammography, where it may offer better detection rates with little extra increase in radiation exposure.

Reconstruction algorithms for tomosynthesis are significantly different from those of conventional CT, because the conventional CT reconstruction requires complete sampling. Besides blurring-out reconstruction algorithms like BP and FBP, iterative algorithms are commonly used, but are extremely computationally intensive.

A typical tomosynthesis imaging system can be decomposed into three parts: image acquisition, image reconstruction and image display.

In image acquisition, the projection images are generated by the X-ray imaging systems. X-ray projection images are generated on the detector with high speed read-out rate and sent to the computer station. Accordingly, X-ray emitter and detector are essential.

Tomosynthesis reconstruction is implemented on a computer with high performance computation. The body component or volume is divided into small units (voxels), and each voxel represents one element with the unique homogeneous intensity. The intensity of every voxel is solved based on the reconstruction model.

The reconstruction results are sent to display to be checked by the radiologists. Some functions, including image contrast enhancement and marking, may be provided.

The efficacy of DBT depends on the image quality, for example high DQE detector, accurate reconstruction algorithm and high-definition image monitor.

### 1.5.1. CURRENT DBT PROTOTYPE SYSTEMS

Many healthcare manufacturers are actively developing digital breast tomosynthesis devices. Most of current DBT prototype system designs re-utilize the conventional mammography design with associated mechanical, electrical and sensor techniques (Park et al 2007). The X-ray tube typically rotates along an arc path above the object to acquire projection images at specified positions with limited view angle. This kind of design is called as partial iso-centric, as shown in Figure 1. Figure 2 shows the related imaging geometry. In Figure 2, the breast object is located above the detector surface with compression. SID represents the source-to-imager distance. The X-ray tube moves above the breast object to acquire multiple projection images with limited view angle. The number of project images varies from 11 to 49 for different prototype systems. Tomosynthesis reconstruction algorithms will be applied to those acquired dataset of projection images to generate slice images passing through different portions of the object. In Figure 2, a representative reconstruction slice  $S$  is shown for illustration purpose.

The design of iso-centric rotation can reutilize the traditional mammography design, decrease the cost and reduce the training procedure for the operators. However, the X-ray tube's movement may introduce motion blur to tomosynthesis images and cause patients' discomfort. (Chen et al 2009, Zhou et al 2010)

A detailed report about the digital breast tomosynthesis imaging systems is listed in Table 2.

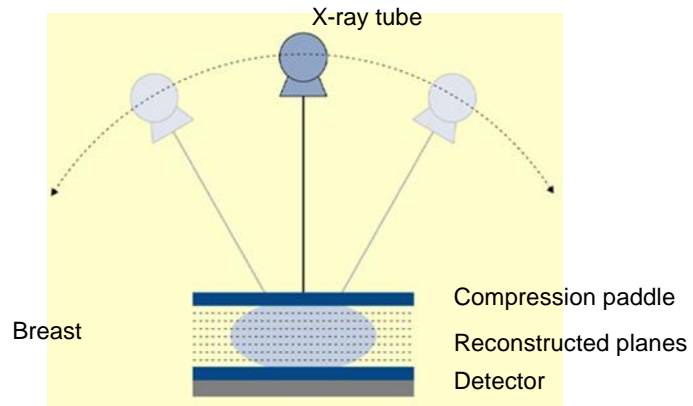


Figure 1. A typical partial iso-centric digital tomosynthesis system design.

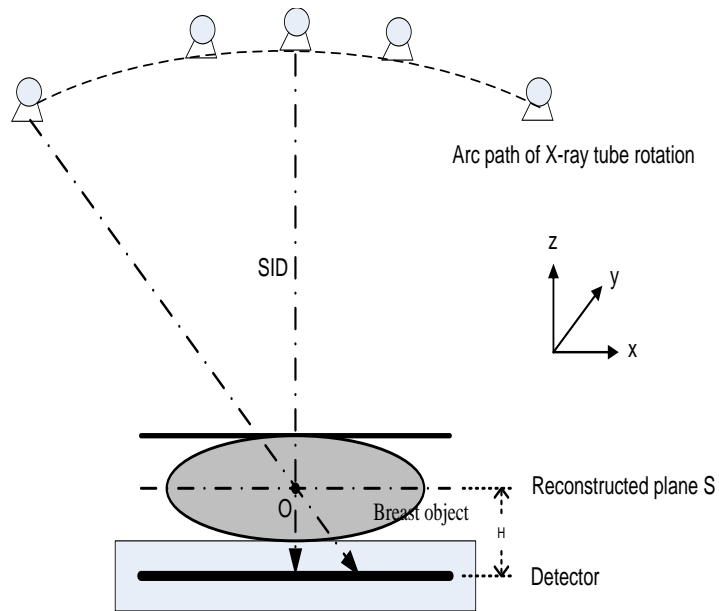


Figure 2. Partial iso-centric tomosynthesis imaging geometry.

Table 2. DBT systems from manufacturers (Zhao et al 2011).

Company	VA	NP	Scanning time (s)	Reconstruction algorithms	Detector
Hologic*	$\pm 7.5^\circ$	11	10	FBP	a-Se, 70 $\mu\text{m}$ 2x2 binning
GE	$\pm 20^\circ$	15	15-23	MLEM SART	CsI/a-Si 100 $\mu\text{m}$
	$\pm 30^\circ$	21	7	SART	
Siemens	$\pm 22^\circ$	25	12.5/20 bin/full	FBP	a-Se, 85 $\mu\text{m}$
Dexela	$\pm 12-20^\circ$	13	30	MLEM	Fiber optic coupled CCD
X-counter	$\pm 13^\circ$	48		FBP iterative	Gas counting 48 slit, 60 $\mu\text{m}$
Sectra	$\pm 5.5^\circ$	21	3-8		Si counting, 21 slit, 50 $\mu\text{m}$

\* means commercially available

In February 2011, the USA FDA approved Hologic, Inc. to market its Selenia Dimensions 2D Full Field Digital Mammography (FFDM) and Digital Breast Tomosynthesis (DBT) system (Figure 3) (Hologic 2012). This DBT system is the first commercially available mammography system that provides 3D images of the breast for breast cancer screening and diagnosis.

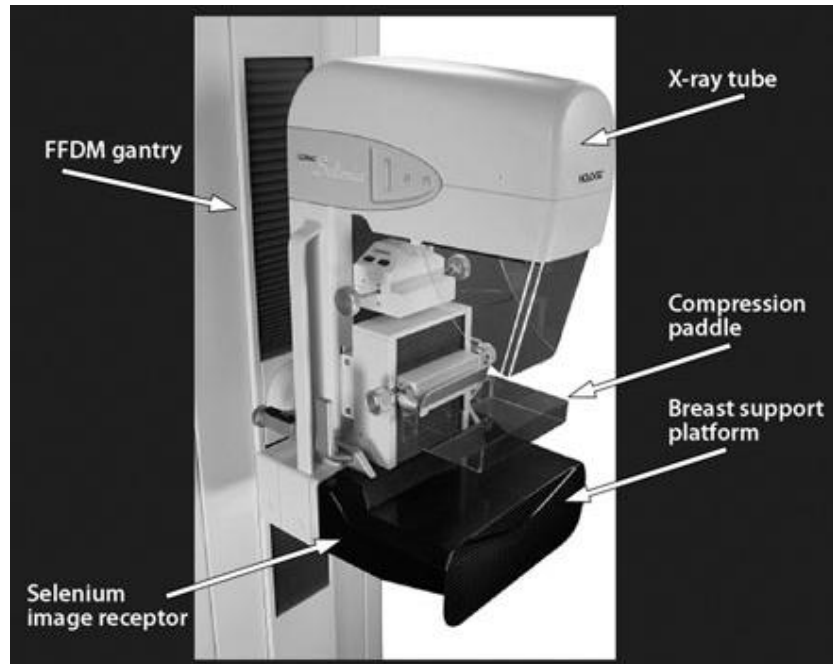


Figure 3. Hologic Selenia Dimensions 2D. Image source: American Roentgen Ray Society (<http://www.ajronline.org/content/189/3/616.full>). This is the only FDA-approved commercially available DBT system.

### 1.5.2. A NOVEL MULTI-BEAM PARALLEL DIGITAL BREAST TOMOSYNTHESIS PROTOTYPE SYSTEM

The rotation of X-ray tube in the current commercial DBT systems may cause motion blur, which will influence the image quality. In additions, the rotation will increase the time of image acquisition.

Recently, a new digital breast tomosynthesis imaging design was developed. Figure 4 shows a picture of the prototype system. Fixed multi-beam field emission tomosynthesis imaging technique was invented with parallel imaging geometry (Lalush et al 2006, Yang et al 2008, Zhou et al 2010). The X-ray tubes were developed based on carbon nanotube techniques and fixed along a line that is parallel to the detector plane. This system design has great potentials to eliminate the motion blur and patients' discomfort associated with partial iso-centric design of typical DBT prototype systems. It

is proposed that the imaging acquisition speed may also be faster compared with that of other designs. In our system setting with 15 projection images and  $14^\circ$  view angle, it takes around 6 seconds in total for image acquisition.

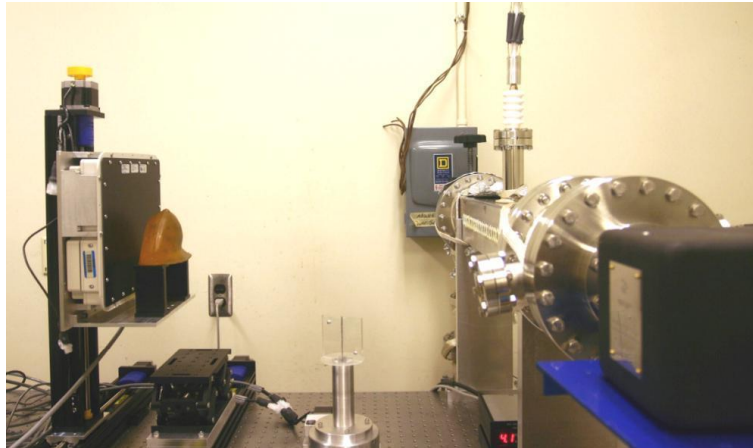


Figure 4. A multi-beam parallel digital breast tomosynthesis system.

Figure 5 illustrates this new parallel tomosynthesis imaging configuration. One can see that multiple X-ray sources are fixed along a line parallel to the detector. No X-ray tube's motion exists. Control signals are triggered to activate each X-ray tube to make projection image one following another to acquire a whole dataset of tomosynthesis projections.

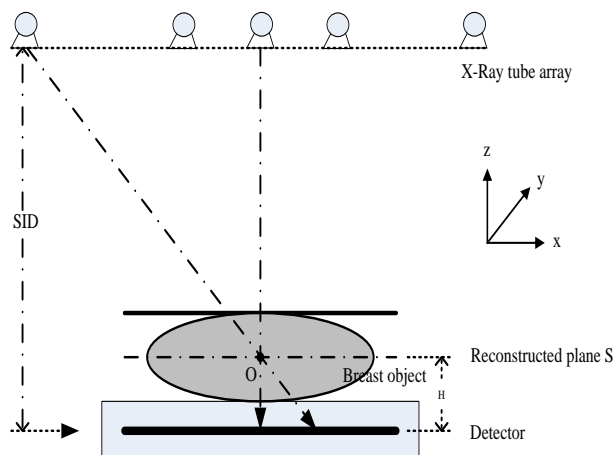


Figure 5. Multi-beam parallel imaging geometry.

## 1.6. IMAGE QUALITY ASSESSMENT

Like in the variety of medical imaging modalities, the objective of creating tomosynthesis images is to diagnose abnormal conditions and guide therapeutic procedures (Sprawls 2012). This subsection will discuss image quality in both spatial domain and frequency domain.

The major image quality issue is the visibility of objects (Sprawls 2012). The visibility of an object is essentially dependent on its physical contrast relative to its surrounding tissue. Image blur may reduce the contrast and visibility of small objects and detail. Image noise, representing a textured or grainy appearance, will influence boundary between visible and invisible objects and reduce object visibility. Artifacts create image features that do not represent a body structure or object and they may be mistakenly interpreted as anatomical features. A good medical image should also provide an accurate representation of the size, shape, and relative positions of tissue.

In many situations, we cannot adjust each imaging variable to maximize object visibility. On one hand, the variables that affect object visibility also affect factors such as radiation exposure, image acquisition time and allocated storage. We hope to minimize the radiation dosage and reduce resource consumption. On the other hand, some image quality factors are adversely affected. If we improve one, the other factor may decrease. A good trade-off has to be carefully kept. A detailed guide about medical image quality can be referred to Sprawls 2012.

Technically, we should have a handful of quantitative specifications to evaluate the image quality (Saunders and Samei 2003, Webb 2003, Saunders et al 2005,

Sprawls 2012). To evaluate the image quality of our new digital breast tomosynthesis prototype system, the main effort is put on the propagation of signal and noise.

In spatial domain, to quantitatively compare image quality, SNR (signal to noise ratio), the spatial resolution and contrast to noise ratio (CNR) are often measured. SNR (Andrew 2002) is a direct measurement regarding the conspicuity of the object. CNR (Andrew 2002) is the measure of separation in terms of average intensity between two tissues of interest. A high value of each of these parameters means a better imaging system, but often compromises among the parameters have to be made.

Compared to the traditional spatial domain analysis tools of image quality, the frequency domain analysis is universal and versatile. With the development of computational technologies, Fourier transform has been stochastically researched with fast computation (Nishikawa 2011). Signals of objects can be decomposed into the combination of sine waves with different amplitudes, frequencies and phases to be evaluated in the frequency domain (Nishikawa 2011). In frequency domain, modulation transfer function (MTF), noise power spectrum (NPS) and noise equivalent quanta NEQ(f) are important image quality factors and used frequently to characterize the performance of medical imaging systems and digital detectors. Physical measurements and computational analysis of MTF, NPS and NEQ are well published in literatures (Dobbins 2000, Samei et al 2006, Dobbins et al 2006, Chen 2007c).

For a typical digital breast tomosynthesis system, image acquisition (X-ray source, detector, etc.), image reconstruction algorithm, and image display constructs the main factors which influence the resulted image quality.

## CHAPTER 2

### IMAGE RECONSTRUCTION ALGORITHMS FOR A MULTI-BEAM PARALLEL DIGITAL BREAST TOMOSYNTHESIS SYSTEM

Tomosynthesis reconstruction algorithms translate two-dimensional projection images into three-dimensional slice images. Many achievements from CT reconstruction inspire the advancement of tomosynthesis reconstruction. However, due to incomplete sampling and low-dosage radiation detection, tomosynthesis reconstruction has many unique properties.

Shift-and-add (SAA) reconstruction algorithm (Niklason et al 1997, Chen et al 2007a) put an important role in the early stage of tomosynthesis imaging. In SAA, the average of the shifted projection images based on the shift amount of the center was calculated to acquire the reconstructed images. It generates limited image quality due to out-of-plane blurring. Back-projection improves the image quality by considering the shift amount of each pixel on the projection image (Chen et al 2007a).

The out-of-plane blur of objects obscured detail in the plane of interest and limited the contrast enhancement of the slices (Dobbins 2003). Great efforts were made to reduce out-of-plane artifacts through the application of filters to back-projection tomosynthesis reconstructions. Currently, filtered back-projection is one of the most commonly used methods (Matsuo et al 1993, Lauritsch and Haerer 1998).

Ghosh used a different method to remove out-of-plane blur (Ghosh Roy et al 1985). The blurring functions were proposed to exactly solve the out-of-plane blur problem generated by the planes immediately adjacent to the plane of interest. Later, Dobbins extended it to the entire set of conventionally reconstructed planes, and

attempted to find the exact solution of in-plane structures from a complete set of tomosynthesized planes (Dobbins et al 1987, Dobbins 1990).

Blurring-out reconstruction algorithms don't calculate the attenuation of X-ray penetration. If we divide the reconstructed object into a great number of small non-overlapping regions (voxels) with constant attenuation coefficients, the other perspective can be proposed to explain the reconstructed images. Firstly, Beer-Lambert Law tells us

$$T = I \cdot e^{-ul} \quad (\text{Eq. 1})$$

where  $T$  is the transmitted X-ray intensity,  $I$  is the incident X-ray intensity,  $u$  is the attenuation coefficient, and  $l$  is the path length where the X-ray projection line passes through the voxel. The pixel value on the reconstruction image represents the attenuation coefficient for the tomosynthesis imaging process.

Lange and Carson (Lange and Carson 1984) introduced statistically iterative reconstruction methods to calculate the attenuation coefficients. The proposed maximum likelihood model maximizes the probability of acquiring the measured projections from the incident X-ray and the current imaging parameters. Lange and Fessler (Lange and Fessler, 1995) presented three methods to solve the ML equations. Wu et. al. (Wu et al 2003) investigated Lange and Fessler's expectation maximization with an iso-centric digital breast tomosynthesis prototype system and further compared MLEM with BP and FBP in their paper (Wu et al 2004). They summarized that BP provided the best SDNR for low-contrast masses but the conspicuity of the feature details was limited by inter-plane artifacts; FBP provided the high edge sharpness for micro-calcifications but the image quality of masses was poor; the information of both

the masses and the micro-calcification were well restored with balanced quality by the MLEM algorithm.

Algebraic reconstruction methods make another way to calculate attenuation coefficients. Based on the exponential relationship between the incident and transmitted intensity, a series of linear equations are modeled. The difficulty of directly solving the large equations leads researchers to explore the iterative numeric methods. Andersen (Andersen and Kak, 1984; Andersen, 1989) proposed simultaneous algebraic reconstruction technique (SART) by fitting the previous solutions to every projection images. Zhang (Zhang et.al., 2006) proved its validity with an iso-centric digital breast tomosynthesis prototype system and further compared SART with BP and MLEM, concluding that the BP method provided very smooth reconstructed images with low background noise, while the SART and MLEM methods considerably enhanced the contrast and edges of the features but simultaneously amplified the image noise; BP method had blurring artifacts in the x-ray source motion direction that obscured the contrast-detail objects, while the other two methods could significantly improve object conspicuity.

In summary, we categorize the reconstruction algorithms into four classes: (1) mathematical reconstruction algorithms, including SAA and BP; (2) filter-based reconstruction algorithms, including FBP and MITS; (3) statistical reconstruction algorithms, for example, MLEM; (4) algebraic reconstruction algorithms, for example, SART. This chapter will explain our implementation and improvement when applying them to our new multi-beam parallel digital breast tomosynthesis system.

## 2.1. BACK PROJECTION (BP)

### 2.1.1. Point-by-point BP

Back projection (Chen et al 2007a, Chen 2007c) is a common mathematic reconstruction algorithm. It is quite similar to Shift-And-Add (SAA) algorithm. During SAA reconstruction, in order to reconstruct 3D slices of the breast, each projection image should be shifted by an amount appropriate for the plane of reconstruction. The shift amount can be calculated based on projected positions from central points of each reconstruction plane. The shifted planes are added together to emphasize structures in the in-focus plane and blur out structures in other planes. In fact, because the different pixels on the reconstruction plane have their unique locations, the shift amounts in SAA should be different.

In order to improve the reconstruction of the single pixel on a reconstruction plane at certain height above the detector, the shift amount should be calculated along both  $x$  and  $y$  directions for each pixel on the reconstruction plane. This idea is called point-by-point back projection.

With the point-by-point BP, shift amounts for every pixel location on each reconstructed plane are computed, taking into account the two-dimensional projection of reconstructed objects in each plane.

In Figure 6,  $A(A_x, A_y, A_z)$  represents coordinate the of the object on the reconstruction plane  $R$ .  $B(B_x, B_y, B_z)$  represents projection coordinate of the point  $A$  on the detector plane.  $R(R_x, R_y, R_z)$  represents the coordinate of the X-ray

source  $R$ . One can find  $A$ 's pixel value by referring to its projected point  $B$ . The location relationship can be written as

$$B_x = R_x + \frac{R_z}{R_z - A_z} \cdot (A_x - R_x)$$

$$B_y = R_y + \frac{R_z}{R_z - A_z} \cdot (A_y - R_y)$$

(Eq. 2)

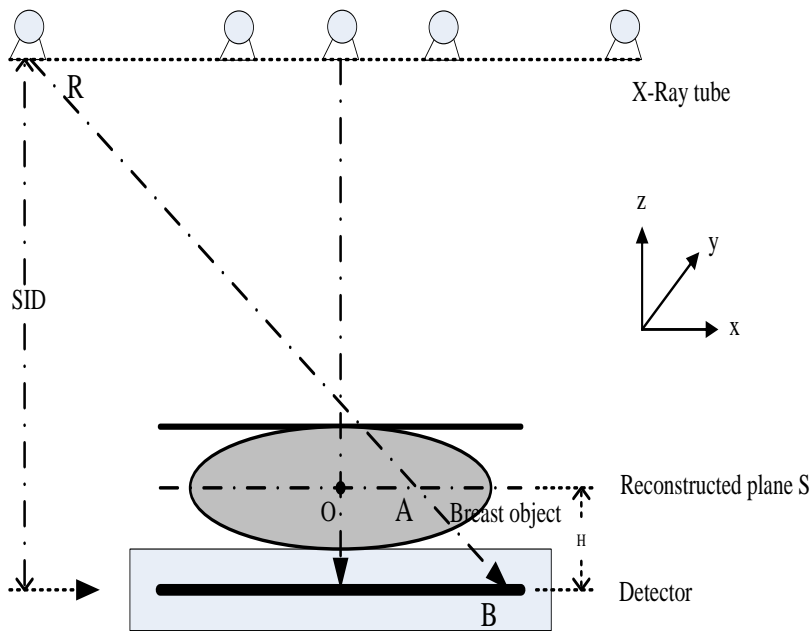


Figure 6. BP reconstruction for a multi-beam parallel breast tomosynthesis system.

The back projected pixels represent the estimation about the internal structure of the object. For each projection image, we can acquire a corresponding estimation. The actual structure can be approximated from all the estimations. An intuitive way to approximate is using the mean values, which is called standard BP for convenience.

The final pixel value of point  $A$  in the standard BP reconstruction is calculated as followed

$$s = \frac{1}{N} \sum_{i=1}^N I(B_i) \quad (\text{Eq. 3})$$

$I(B_i)$  is the back projected pixel value based on Eq. 2 for the pixel  $A$  and the  $i^{\text{th}}$  projection image (X-ray source), and  $N$  is the total number of projection images.

### 2.1.2. Ray-tracing BP

In the linear attenuation equation, the total intensity attenuation depends on both attenuation coefficients as well as path lengths.

A ray-tracing back-projection was proposed based on this fact (Zhang et.al., 2006). The general equation can be written as

$$u_j = \frac{\sum_{i=1}^M l_{ij} \left( \frac{y_i}{L_i} \right)}{\sum_{i=1}^M l_{ij}} \quad (\text{Eq. 4})$$

This equation takes into account of the proportion of different path lengths.  $i$  is the index of the  $i^{\text{th}}$  projection line,  $j$  is the index of  $j^{\text{th}}$  voxel.  $L_i$  is the total path of the  $i^{\text{th}}$  projection line.  $y_i$  is the detected x-ray intensity.

## 2.2. FILTERED BACK-PROJECTION (FBP)

Filtered back-projection (Stevens et al 2001, Mertelemeier et al 2006), is transplanted form CT imaging. It considers the projection and back projection based on Radon transform and Fourier slice theorem. Of many image reconstruction methods in X-ray imaging, FBP has been a classic one.

## 2.2.1. Radon transform, Fourier-slice theorem and 2D parallel-beam filtered back projection

### Radon transform

Radon transform (Radon 1917, Gonzalez and Woods, 2008) presents the integral relationship between the original object and its projection. It can be written as

$$g(s, \theta) = \int_{-\infty}^{+\infty} \int_{-\infty}^{+\infty} f(x, y) \delta(x \cos \theta + y \sin \theta - s) dx dy \quad (\text{Eq. 5})$$

where  $x, y, s$  and  $\theta$  are variables.  $\delta$  is impulse function. If we fix  $\theta$  and let  $S$  vary, this equation simply sums the pixels of  $f(x, y)$  along the line defined by the specified values of the two parameters  $x$  and  $y$ . Incrementing through all values of  $p$  required to span the images (with  $\theta$  fixed) yield one projection. Changing  $\theta$  and repeating the foregoing procedure yields another projection, and so forth.  $f(x, y)$  is the object function.  $g(s, \theta)$  is the projection.

By summing up Radon projection along all angles passing the same pixel, the back projection can be written as

$$\tilde{f}(x, y) = \int_0^\pi g(x \cos \theta + y \sin \theta, \theta) d\theta \quad (\text{Eq. 6})$$

$\tilde{f}(x, y)$  is an approximation to the image from which the projection was generated.

The sampling rates have a profound influence on image reconstruction results. There are two sampling considerations: The first is the number of rays used, which determines the number of samples in each projection. The second is the number of rotation angle increments, which determines the number of projection images. Under-

sampling may result in artifacts in the reconstruct image, such as streaks. Figure 7 shows the image reconstruction results by inverse Radon transform. As view angle and number of projection images increase, the reconstructed images reveal the structures of object with shaper edges and less artifact.

### Fourier-slice theorem

Fourier-slice theorem (Gonzalez and Woods, 2008) states that the Fourier transform of a projection is a slice of the 2D Fourier transform of the region from which the projection was obtained. As Figure 8 shows, the 1-D Fourier transform of an arbitrary projection is obtained by extracting the value of  $F(u, v)$  along a line oriented at the same angle as the angle used in generating the projection.

### 2D parallel-beam filtered back projection

The 2D inverse Fourier transform of  $F(u, v)$  is

$$f(x, y) = \int_{-\infty}^{+\infty} \int_{-\infty}^{+\infty} F(u, v) e^{j2\pi\omega(u x + v y)} du dv \quad (\text{Eq. 7})$$

In polar coordinates, if let  $u = \omega \cos \theta$  and  $v = \omega \sin \theta$ , the equation becomes

$$f(x, y) = \int_0^\pi \left[ \int_{-\infty}^{+\infty} |\omega| G(\omega, \theta) e^{j2\pi\omega\rho} d\omega \right]_{\rho=x\cos\theta+y\sin\theta} d\theta \quad (\text{Eq. 8})$$

In the inner expression,  $|\omega|$  is a ramp filter. It is not integrable because its amplitude extends to infinite in both directions, so the inverse Fourier Transform is undefined. In practice, the method is to window the ramp so it becomes zeros outside of a defined frequency interval. (Gonzalez and Woods, 2008)

VA \ NP	15	29	91	181
14°				
28°				
56°				
112°				
180°				
Figure 7. Image reconstruction by inverse Radon transform.				

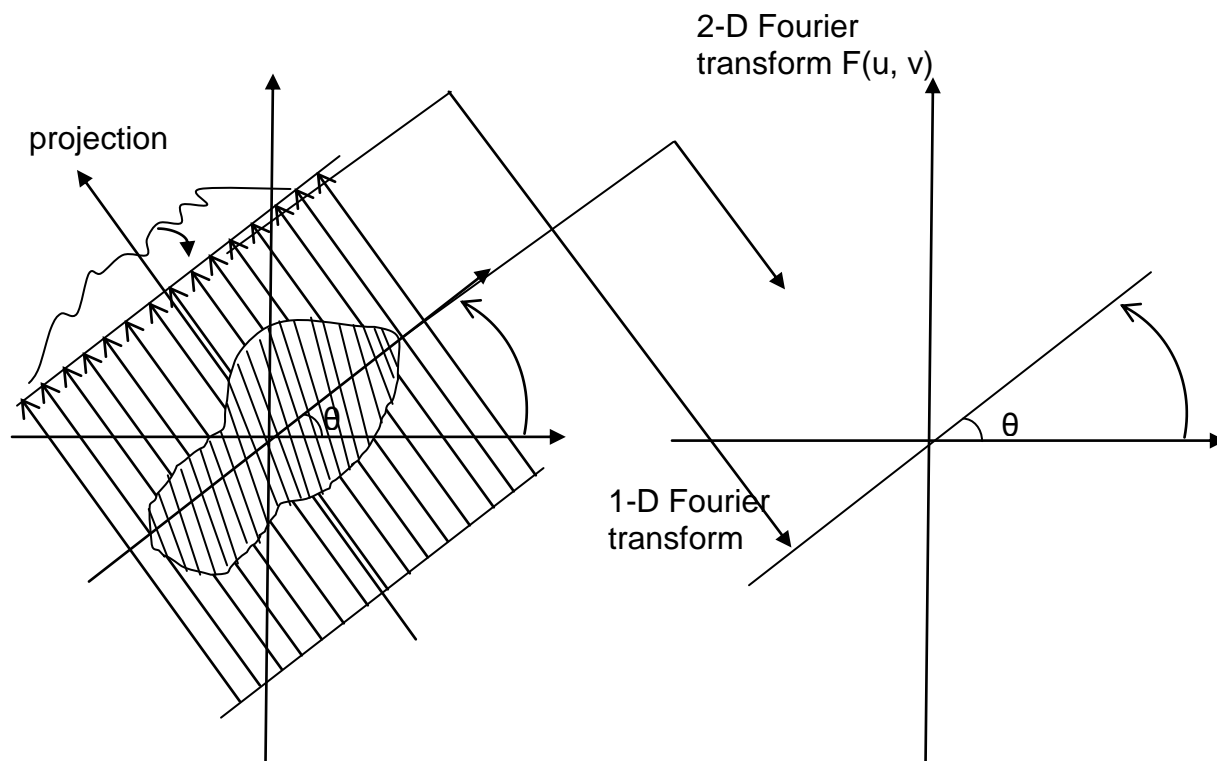


Figure 8. Fourier slice theorem.

Unfortunately, the ramp filter causes noticeable ringing artifacts. A Han window is often used in this situation. Please refer to Gonzalez and Woods 2008 for more details.

Accordingly, a complete back-projection image reconstruction algorithm with filters is obtained. Figure 9 compares the reconstructed results with different filtering settings. The blur artifact in Figure 9(a) is very serious; after we use ramp filter, as shown in Figure 9(b), the objects become much clearer, but there is ring artifact. Han filter contributes to the suppression of ring artifact as shown in Figure 9(c).

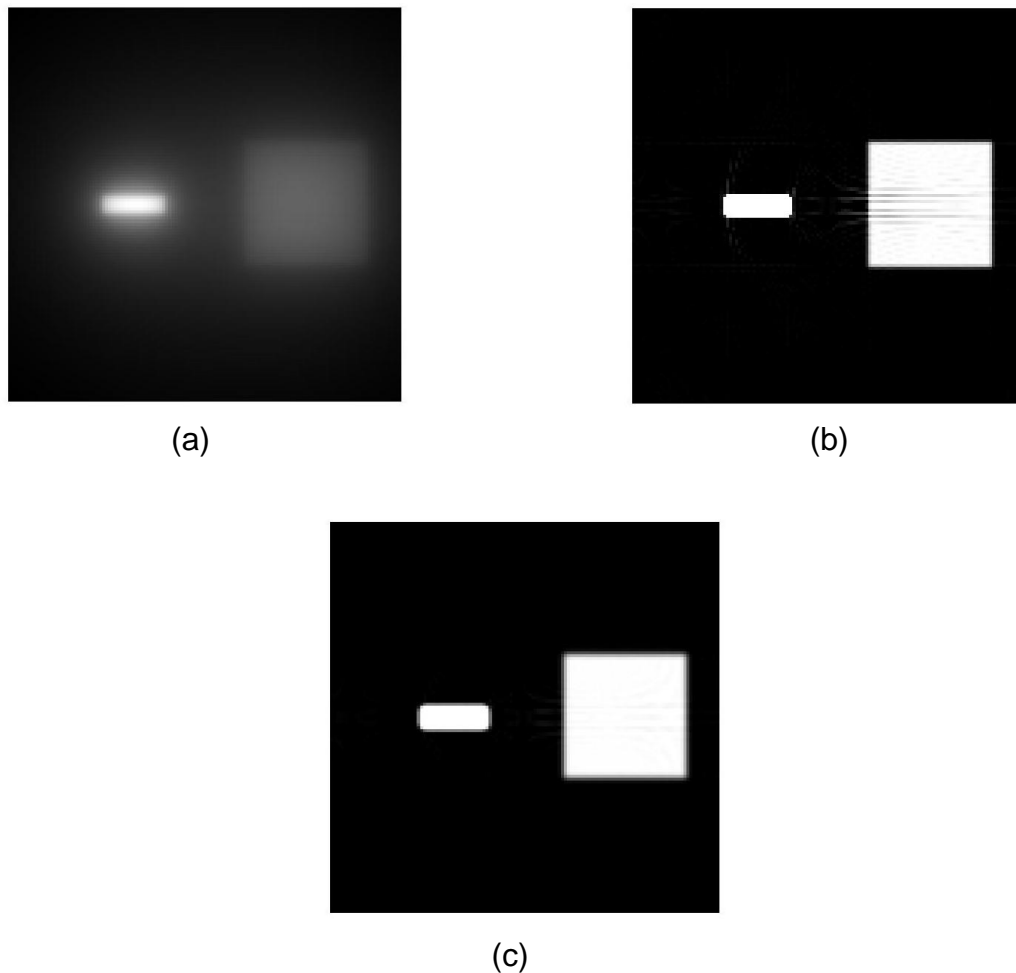


Figure 9. Inverse Radon transform. (a) without any filter. (b) with ramp filter. (c) with ramp and Han filter.

## 2.2.2. Implementation of FBP for a multi-beam parallel digital breast tomosynthesis system

A filtering workflow in our FBP reconstruction algorithm is created. Figure 10 shows the shapes of filters.

### Ramp filter

Ramp filter reflects the sampling geometry of the scanning process. It was designed based on the sampling density. It can be written as:

$$H_{Ramp}(\omega_x, \omega_y, \omega_z) = \sqrt{\omega_x^2 + \omega_z^2} \quad (\text{Eq. 9})$$

$w$  is frequency bin.

### Han filter

A Han filter is used to change the frequency response of ramp-filtered BP reconstruction. With realistic, noisy data, it can also smoothen the image. It can be written as ( $\omega_N$  is the total frequency bin number in  $X$  direction) :

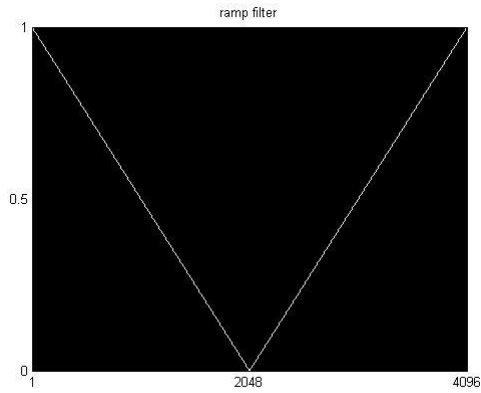
$$H_{Ham} = 0.5(1 + \cos(\frac{\pi\omega_x}{\omega_N})) \quad (\text{Eq. 10})$$

### Gaussian filter

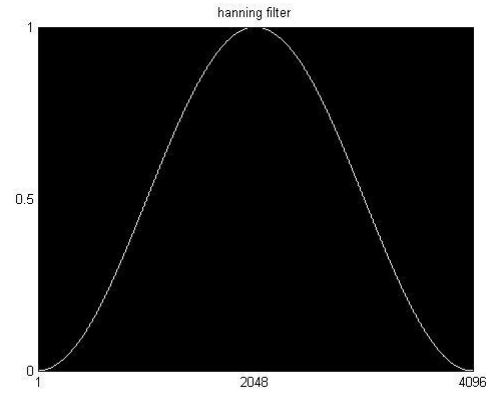
In order to control the high frequency noise amplification in FBP, a Gaussian filter is also applied:

$$H_{Gaussian} = e^{-\frac{u^2}{k^2}} \quad (\text{Eq. 11})$$

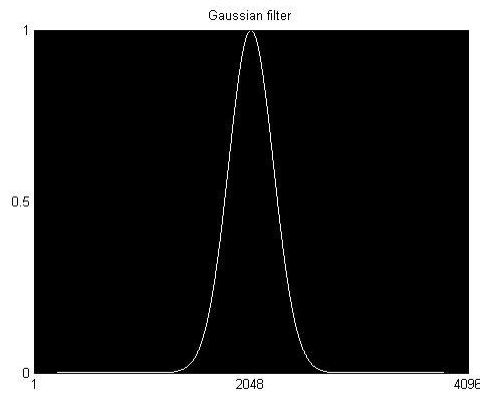
where  $u$  is the individual frequency bin and  $k$  is the kernel size.  $k = 30$  is set in our implementation.



(a)



(b)



(c)

Figure 10. Filters in FBP. Here we suppose our frequency size is 4096. (a) Ramp filter. (b) Han filter. (c) Gaussian filter.

### 2.3. MATRIX INVERSION TOMOSYNTHESIS ALGORITHM (MITS)

MITS (Chen et al 2004, Dobbins and Powell 1987, Dobbins 1990, Godfrey et al 2001, Godfrey and Dobbins 2002, Godfrey et al 2003, Godfrey et al 2006, Warp et al 2000) uses linear algebra to solve for the relative blur in each plane. Mathematically, if the structures in the  $i^{th}$  plane are defined as  $p_i$ , then the tomosynthesized images  $s_i$  may be described as

$$\begin{aligned}
s_1 &= p_1 \otimes f_{11} + p_2 \otimes f_{12} + \dots + p_n \otimes f_{1n} \\
s_2 &= p_1 \otimes f_{21} + p_2 \otimes f_{22} + \dots + p_n \otimes f_{2n} \\
&\dots \\
s_n &= p_1 \otimes f_{n1} + p_2 \otimes f_{n2} + \dots + p_n \otimes f_{nn}
\end{aligned}
\tag{Eq. 12}$$

where  $f_{ij}$  is the blurring function for the structures in the plane  $j$  that appear in the tomosynthesized image of plane  $i$ . The convolutions of the above equations become simply multiplications in Fourier space. In matrix form, it will be

$$S = M \times P \tag{Eq. 13}$$

where  $M$  is the matrix of Fourier transforms of blurring functions.

By multiplying each side of the equation by the inverse of the matrix  $M$ , the patient structure  $P$  in Frequency space can be acquired. Then by taking the inverse Fourier transform, we can get the patient structure.

$$P = M^{-1} \times S \tag{Eq. 14}$$

#### 2.4. STATISTICAL ITERATIVE RECONSTRUCTION ALGORITHMS

In statistics, for a fixed set of data and underlying statistical model, the method of maximum likelihood selects values of the model parameters that produce a distribution that gives the observed data the greatest probability, i.e., parameters that maximize the likelihood function.

In X-ray imaging physics, the relationship between the incident X-ray intensity, detected X-ray intensity and X-ray attenuation follows Poisson distribution ([Webb 2003]). Only a fraction of the photons successfully travel from source to detector along a given path (projection line) during tomosynthesis imaging. Statistical reconstruction attempts to maximize the likelihood of getting the detected X-ray intensity from the incident intensity and X-ray attenuation model.

The likelihood function can be written as

$$L(u | (x_1, x_2, \dots, x_n)) = f(x_1, x_2, x_n | u) = \prod_i^n f(x_i | u) \quad (\text{Eq. 15})$$

$f$  is the probability density function,  $u$  is the free variable.  $x_1, \dots, x_n$  are observed values.

The statistical reconstruction model divides the object into small voxels with constant attenuation coefficient  $u$ . The detected x-ray intensity constitutes the observed data for statistical reconstruction.

The intensity attenuation can be written as

$$\bar{Y}_i = D_i e^{-\langle l, u \rangle_i} \quad (\text{Eq. 16})$$

The original ML function can be written as

$$L = \prod_i \{P_i(Y_i | u)\} = \prod_i \left\{ \frac{e^{-\bar{Y}_i} \bar{Y}_i^{Y_i}}{Y_i!} \right\} \quad (\text{Eq. 17})$$

$i$  is the  $i^{\text{th}}$  X-ray projection line. The linear attenuation coefficients  $u$  is defined for each pixel in the reconstruction volume. Since  $u$  is the probability of photon capture per unit length of voxel  $j$ , one has the physical constraint  $u \geq 0$ . The Poisson nature of X-ray generation implies that the various projections are independent.

#### 2.4.1. Maximum likelihood expectation maximization (MLEM)

##### (1) Algorithm

Expectation maximization is a commonly used solution of maximum likelihood problem. Lange and Fessler also provided two other methods, including Gradient Algorithm and Convex Algorithm (Lange and Fessler 1995). This dissertation focuses on MLEM method.

Expectation maximization algorithm provides an easily implemented method for searching maximum likelihood solution. It has two steps:

$$\text{E-step: calculate } L(u | u^{(t)}) \quad \text{using } Y \text{ and } u^{(t)} \quad (\text{Eq. 18})$$

$$\text{M-step: find } u^{(t+1)} = \arg \max \{ L(u | u^{(t)}) \}$$

According to related literatures (Wu et al 2003, Wu et al 2004, Zhang et al 2006), the iterative procedure to acquire the attenuation coefficient  $u$  is shown as below:

$$u_j^{(t+1)} = u_j^{(t)} + \Delta u_j^{(t)} = u_j^{(t)} + \frac{u_j^{(t)} \sum_i l_{ij} \left( I_i e^{-\langle l, u^{(t)} \rangle_i} - T_i \right)}{\sum_i \left( l_{ij} \langle l, u^{(t)} \rangle_i I_i e^{-\langle l, u^{(t)} \rangle_i} \right)} \quad (\text{Eq. 19})$$

$$\langle l, u \rangle_i = \sum_j l_{ij} u_j$$

where  $T_i$  is the transmitted X-ray intensity or detected pixel value on the detector for the X-ray projection line  $i$ .  $j$  is the individual voxel in the three-dimensional attenuation model.  $\langle l, u \rangle_i$  means the total attenuation of the X-ray projection line  $i$ .  $I_i$  is the incident X-ray intensity to pixel  $i$ . Usually, we can replace  $I_i$  with the flat image.  $l_{ij}$  is the path length of the intersection between the voxel  $j$  and the X-ray projection line from the x-ray source to the pixel  $i$  on the detector.

## (2) Direct implementation

To solve Eq. 19, a direct workflow is presented as in Figure 11. For convenience we call it standard MLEM implementation.

It is not difficult to estimate that the most inner statement (Line 6) will run  $t^*j^*i^*$  times. The time complexity is  $O(t^*j^*i^2)$ . It will take much time to finish the computation. Accordingly, reducing loop complexity will contribute to the improvement of computation efficiency.

```
1 for each iteration  $t$ 
2   for each voxel  $j$ 
3     for each X-ray projection line  $i$ 
4       calculate the path length where x-ray  $i$  passes through voxels
5       for each X-ray projection line  $i$ 
6         calculate the total intensity attenuation
7       end
8       calculate  $\Delta u_j$ 
9     end
10  end
11  for each voxel  $j$ 
12    update  $u_j$ 
13  end
14 end
```

Figure 11. Direct workflow of MLEM implementation.

### (3) Acceleration

#### **A novel data structure based on sparse matrix ray-tracing method (Zhou, 2008)**

Since the statement in Line 6 of Figure 11 is executed for many times, how to solve the path length  $l_{ij}$  and create the indices between each X-ray projection line and corresponding voxels is very important to enhance the efficiency of the procedure. We introduced a simplified and equivalent implementation with a novel data structure for ray-tracing method.

Ray tracing is a frequently used method to solve the length of the path where each X-ray projection line passes through each voxel (Chen 2007c). In fact, on every reconstruction plane, for each X-ray projection line  $i$ , only a few voxels are passed through. This results in the sparse matrix condition. The sparse condition is involved in the strategy of managing the relationship between the X-ray projection line  $i$ , the voxel  $j$ , and the path length  $l_{ij}$ . Here we adopted the combination of the array and linked lists. All voxels penetrated by the X-ray projection line  $i$  were simply organized into a linked list. The linked list was then mounted to the X-ray projection line array.

Figure 12 illustrates the data structure. It utilizes the feature of the sparse matrix to save allocated memory for path  $l_{ij}$  calculation. It is convenient to visit the voxels which are penetrated by the X-ray projection line  $i$ . This linked list based on sparse matrix serves as the foundation of loop order adjustment.

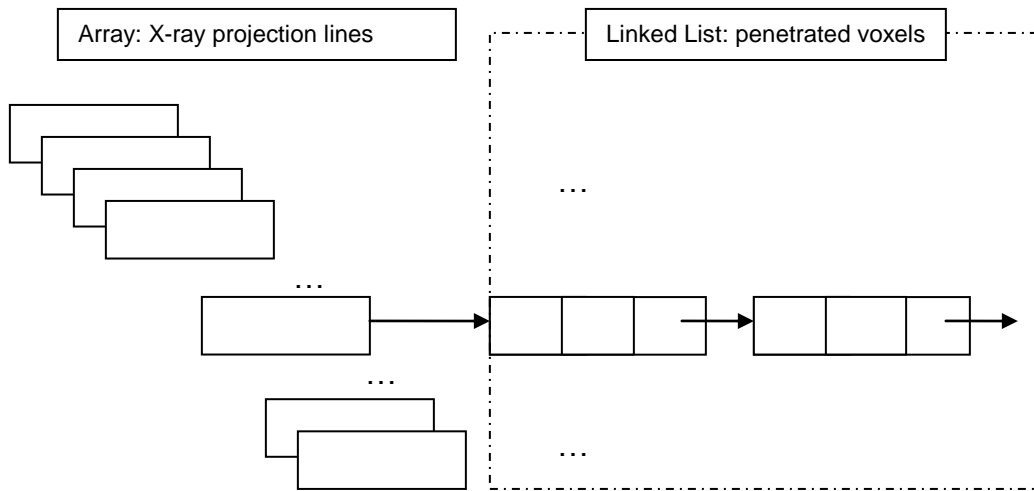


Figure 12. Combined data structure of managing the relationship between x-ray projection lines and voxels.

### Loop order adjustment

Since the length of the path  $l_{ij}$  is fixed during the total iteration, it can be extracted and calculated before the iteration. As illustrated before, Line 6 in Figure 11 runs many times. Line 6 can be put into the initial procedure.

Now we are able to prepare all parameters for the update of  $u$ . In Eq. 19, the update of  $u$  can be divided into two parts correspondingly, and the whole procedure can be adjusted as shown in Figure 13.

Because of the combination of array and linked lists, the statements of Line 5 and Line 10 in Figure 13 will be speeded up significantly.

```

1 calculate  $l_{ij}$  by ray-tracing method
2 for each iteration  $t$ 
3   for each X-ray projection line  $i$ 
4     for each voxel which is affiliated to  $i$  in Figure 12
5       calculate the total intensity attenuation when passing through voxels
6     end
7   end
8   for each X-ray projection line  $i$ 
9     for each voxel which is affiliated to  $i$  in Figure 2
10      calculate the nominator and denominator of  $\Delta u_j$ 
11    end
12  end
13  for each voxel  $j$ 
14    update  $u_j$ 
15  end
16 end

```

Figure 13. Accelerated MLEM implementation workflow.

#### (4) Time complexity and image quality

Two main factors should be taken into account to evaluate the time complexity of our accelerated implementation of MLEM algorithm: (1) computing the path length  $l_{ij}$  when the X-ray projection line passes through voxels; (2) iterating and updating the attenuation coefficient of each voxel.

We assume that the variable  $p$  represents the total number of reconstructed planes. As mentioned before, the X-ray projection line  $i$  denotes the X-ray projection line and  $j$  denotes the voxel on reconstruction object. For the calculation of path length  $l_{ij}$ , the required time complexity is  $O(i \cdot p)$ . For reconstruction iteration, the required time complexity is estimated as  $O(t \cdot i \cdot \eta)$  ( $t$  is the iteration number), where  $\eta$  is not greater than the maximum number of the voxels associated with X-ray  $i$ . The relationship is sparse and  $\eta \ll j$ , therefore the time complexity decreases from  $O(t \cdot j \cdot i^2)$  to  $O(t \cdot i \cdot \eta)$  for our accelerated MLEM algorithm.

Figure 14(a) and 14(b) show the in-focus impulse responses reconstructed by standard MLEM and our accelerated MLEM implementation respectively. Figure 14(c) shows the subtraction of impulse responses of Figure 14(a) and 14(b). One can see that both standard MLEM implementation and our accelerated one can reconstruct the impulse by showing sharp response on in-plane reconstruction. There is no difference between the impulse responses when comparing Figure 14(a) and 14(b) by subtraction as shown in figure 14(c).

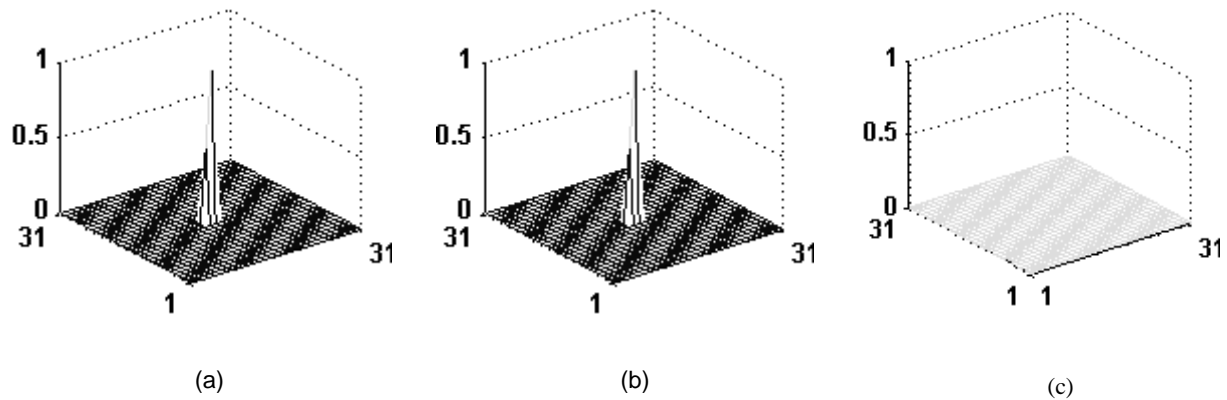


Figure 14. Comparison of results reconstructed by standard MLEM and accelerated MLEM implementations. (a) Impulse response of standard MLEM ( $H=10\text{mm}$ ). (b) Impulse response of accelerated MLEM. (c) Subtraction results.

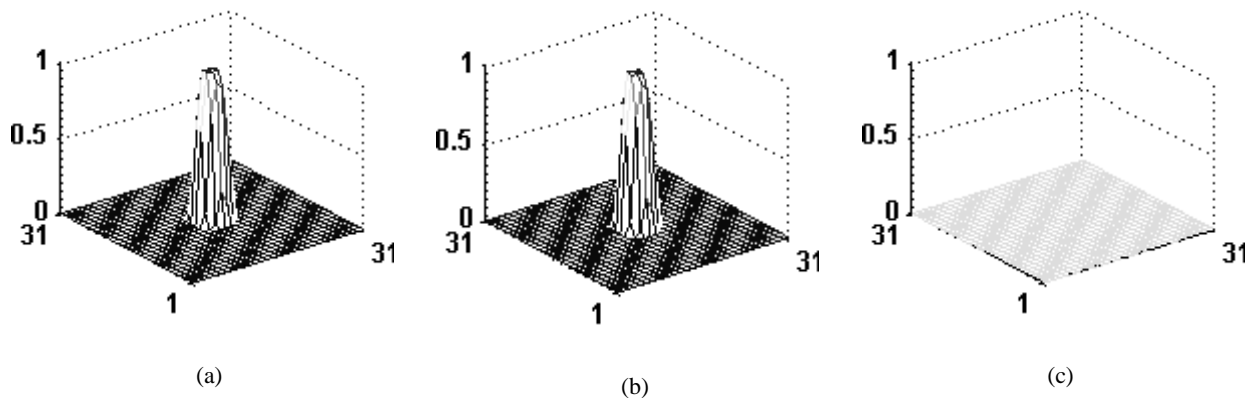


Figure 15. Comparison of results reconstructed by standard MLEM and accelerated MLEM implementations. (a) Impulse response of MLEM ( $Z=10\text{mm}$ ). (b) Impulse response of accelerated MLEM. (c) Subtraction results.

Figure 15(a) and 15(b) show the in-focus reconstruction responses of simulated spherical object. Figure 15(c) shows the subtraction of Figure 15(a) and 15(b). Both standard MLEM implementation and accelerated one can reconstruct the three-dimensional spherical object by showing response correctly on in-plane reconstructions. There is no difference between the performance of standard MLEM and accelerated MLEM when compared Figure 15(a) and 15(b) by subtraction as shown in Figure 15(c).

Table 3 shows the running time required to reconstruct a single reconstruction plane. Image sizes of 256×256 pixels, 512×512 pixels and 1024×1024 pixels (full size) were investigated. Iteration numbers of 3, 8 and 20 were tested. A 2.4G HZ desktop computer with 3G memory was used to run our algorithms coded in Visual C++. One can find that the typical computation time with 8 iterations was only 97 seconds with accelerated MLEM implementation to reconstruct a single slice of the size 1024×1024.

Table 3. Running time (seconds) of accelerated MLEM implementation.

Image size Iteration	256×256	512×512	1024×1024
3	2	10	52
8	3	15	97
20	6	33	210

In summary, a fast MLEM implementation for 3D image reconstruction in digital breast tomosynthesis was developed. Compared to the standard MLEM implementation, the accelerated MLEM implementation is capable of producing the same image quality with much faster running speed.

#### 2.4.2. Ordered-subset MLEM (OS-MLEM)

Ordered subset MLME (Erdogan et al 1999) algorithm has enjoyed considerable interest for tomosynthesis image reconstruction due to its acceleration of the MLEM algorithm. OS-MLEM has the following advantages (Erdogan et al 1999):

(1) OS-MLEM provides order-of-magnitude acceleration over MLEM. The MLEM converges very slowly because it greedily absorbs all the projection view information in each iteration. In OS-MLEM, only a subset of the projection image dataset is used for each iteration.

(2) Good reconstruction images can be acquired.

(3) OS-MLEM is easily implemented by slightly modifying the original MLEM algorithm.

However, because OS-MLEM uses part of the projection views when updating the attenuation coefficients, it is not stable when reaching the convergence.

Our implementation is very intuitive. We used a direct transform of MLEM and changed the original update into projection-by-projection view update. To improve the convergence, we designed a special update order to maximize the angle separation (Li et al 1993) between the successive absorbed projection views.

## 2.5. ALGEBRAIC ITERATIVE RECONSTRUCTION ALGORITHMS

In algebraic iterative reconstruction algorithms (Szepessy 2012), the procedure of estimating the attenuation coefficients, generating a new set of projection images from the estimate, comparing the simulated images to real projection data, then smearing the difference back to generate a new estimate is iteratively called.

### 2.5.1. Linear attenuation equations

The Beer-Lambert Law in Eq. 1 can be re-written as

$$\sum_j^J l_{ij} u_j = D_i \quad i = 1, 2, \dots, M \quad (\text{Eq. 20})$$

where  $D_i = \log \frac{I_i}{T_i}$

$M$  is the total number of projection lines,  $J$  is the total voxel number, and  $l_{ij}$  is the fractional area of the  $j^{\text{th}}$  voxel intercepted by the  $i^{\text{th}}$  projection line.

If  $M$  and  $J$  were small, we could use conventional matrix theory methods to invert the equations. However, in practice  $M$  and  $J$  may be huge (more than 10000). It is impossible to solve direct matrix inversion.

An iterative solution can be used. If we simplify Eq. 20 to an equation group including only two equations, the computational procedure for searching the solution consists of first starting with an initial guess, projecting this initial guess on the first equation, reprojecting the resulting point on the second equation, and then projecting back onto the first equation, and so forth. If a unique solution exists, the iterations will always converge to that solution (Szepessy 2012).

### 2.5.2. Simultaneous algebraic reconstruction technique (SART)

In our SART implementation, the solution for the attenuation coefficients is expressed as (Zhang et al 2006)

$$u_j^{(t+1)} = u_j^{(t)} + \Delta u_j^{(t)} = u_j^{(t)} + \frac{\sum_i l_{ij} \left( \frac{D_i - \sum_j l_{ij} u_j^{(t)}}{\sum_j l_{ij}} \right)}{\sum_i l_{i,j}} \quad (\text{Eq. 21})$$

where  $D_i = \log \frac{I_i}{T_i}$ .

We developed an accelerated SART implementation with a novel data structure and corresponding loop adjustment like in accelerated MLEM.

## 2.6. VALIDITY OF RAY-TRACING-BASED RECONSTRUCTION ALGORITHMS

The ray-tracing BP, MLEM, OS-MLEM and SART commonly use ray-tracing model to calculate X-ray intensity attenuation. A finite elements modelling (FEM) simulation was used to evaluate the validity of these four reconstruction algorithms.

Two balls were simulated with the different attenuation coefficients of 0.2 and 0.038 mm<sup>-1</sup> to imitate the mass and micro-calcification. A FEM method was used to create the volume. Then the ray-tracing method was used to generate the projection images. The reconstruction algorithms of ray-tracing BP, MLEM, OS-MLEM and SART were used to reconstruct projection data. Then, attenuation error and mean square error were calculated.

The attenuation error is calculated based on the linear attenuation equation, i.e.

$$AttenuationError = \sum_i |T_i - I_i \cdot e^{-\langle l, u \rangle_i}| \quad (\text{Eq. 22})$$

for all the X-ray projection lines.

The mean square error between the real finite elements volume and the reconstructed volume is defined as

$$MSEError = \frac{\sum_{j=1}^J |u_j - \hat{u}_j|}{J} \quad (\text{Eq. 23})$$

for all the voxels.

In Figure 16, based on the curves of these two evaluation functions, we have these conclusions:

(1) OS-MLEM and SART provide minimal reconstruction and attenuation error for the specified iteration number. This shows that they converge faster.

(2) Ray-tracing BP can be a good initialization for iterative reconstruction algorithms.

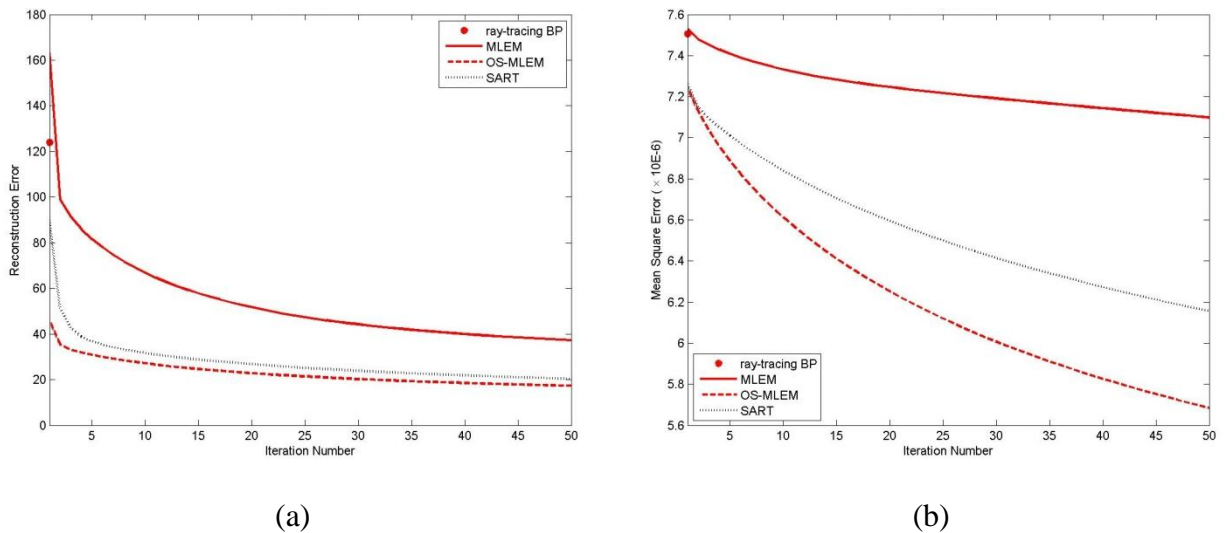


Figure 16. Comparison of ray-tracing-based reconstruction algorithms. (a) Attenuation error. (b) Mean square error.

## 2.7. IMAGE RECONSTRUCTION WITH AN ACR TRAINING PHANTOM

To evaluate different reconstruction algorithms, an ACR training phantom was used. Figure 17 shows the embedded objects (Zhang et al 2006) and the low dose middle projection image.

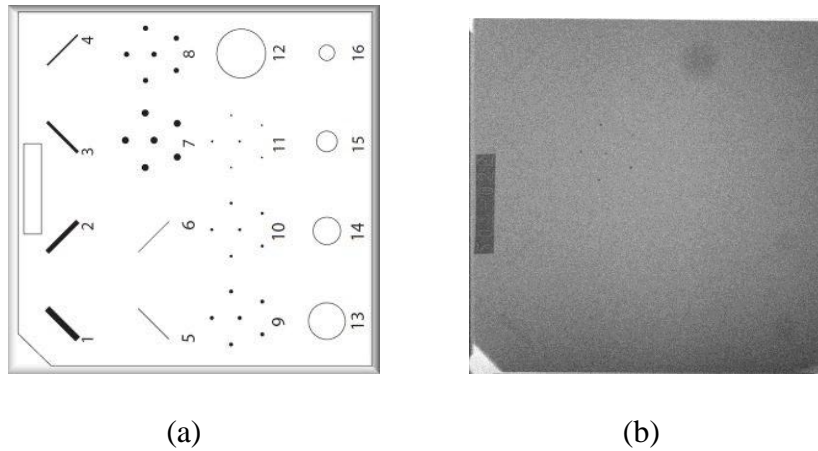


Figure 17. ACR phantom. (a) Embedded objects. (b) Low-dose middle projection image.

Figure 18 shows reconstructed planes with different heights by five algorithms including BP, FBP, MITS, MLEM, and SART respectively.

In Figure 18,  $Z=61.0$  is the focus plane. With the increase of plane height, the objects get blurred, and it greatly presents the three-dimensional information.

Accordingly, the investigated five algorithms are capable of providing the reconstruction of the phantom with three-dimensional localization, shape and edge information.

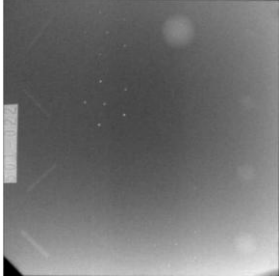
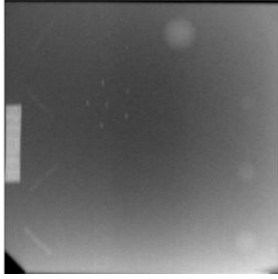
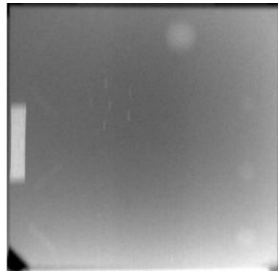
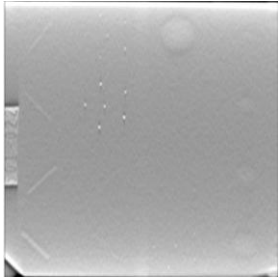
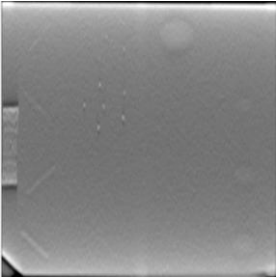
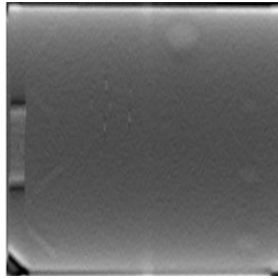
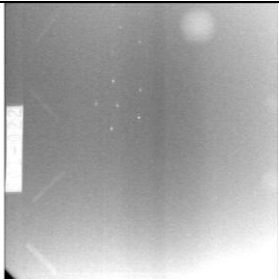
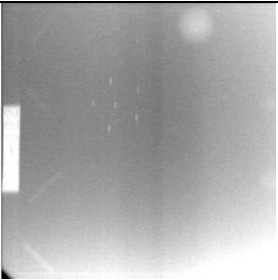
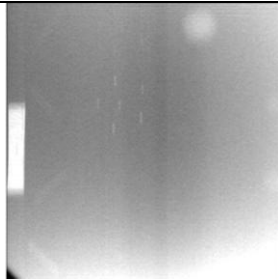
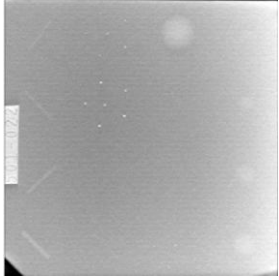
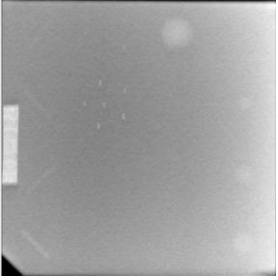
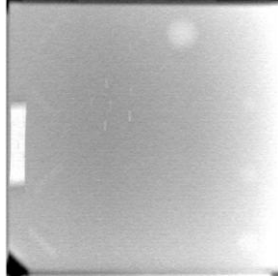
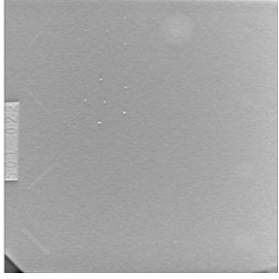
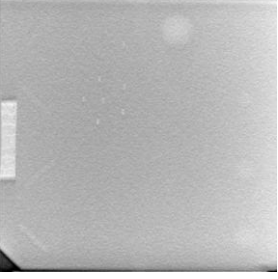
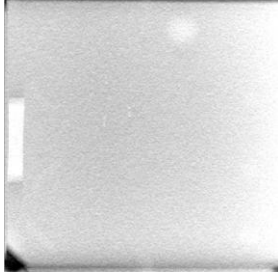
	Z=61.0 mm	Z=66.0 mm	Z=71.0 mm
BP			
FBP			
MITS			
MLEM			
SART			

Figure 18. Reconstructed in-plane ROIs of ACR phantom. Z is the height of reconstructed ROIs.

## 2.8. IMAGE RECONSTRUCTION WITH A BREAST BIOPSY TRAINING PHANTOM

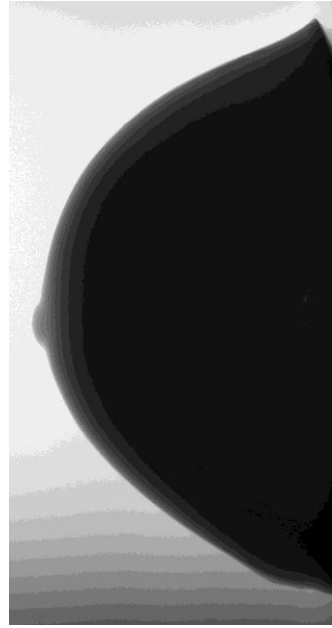
A standard breast biopsy training phantom (CIRS company 2010) was used in the experiment to compare the system performance. Solid masses and micro-calcification clusters were embedded into the phantom as the targets of the evaluation. Figure 19 (a) shows the picture of the phantom. Figure 19(b) shows the low-dosage middle projection image. Figure 20 shows the reconstructed slice images by BP, FBP, MITS, MLEM, OS-MLEM and SART.

One mass and micro-calcification were individually selected as our evaluation targets. Figure 21 shows the ROIs containing the targets on the low dose middle projection image of the training phantom acquired by the tomosynthesis imaging system. The six representative algorithms including BP, FBP, MITS, MLEM, OS-MLEM and SART were investigated to generate reconstruction images and evaluate the image quality of the targets.

Figure 22 shows reconstructed ROIs from the six algorithms including BP, FBP, MITS, MLEM, OS-MLEM and SART respectively. In Figure 21, one can hardly identify the embedded objects (mass and micro-calcification) in the original middle projection image. The margin and shape of the micro-calcification is not visible. In Figure 22, with the six different tomosynthesis reconstructions, the visibility of the objects is much better than that in Figure 21. Margins and shapes are clearer. Figure 23 shows line profiles of reconstructed masses. Accordingly, again, the investigated algorithms are capable of providing the reconstruction of the phantom with three-dimensional localization, shape and edge information.

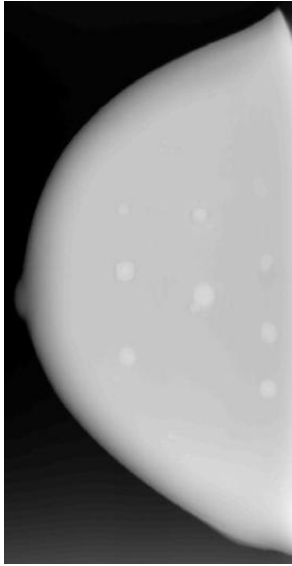


(a)

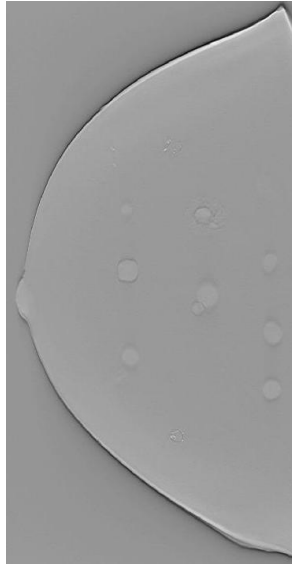


(b)

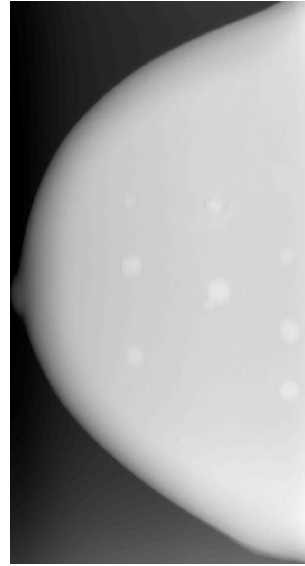
Figure 19. (a) CIRS biopsy training phantom. (b) Low dose middle projection image.



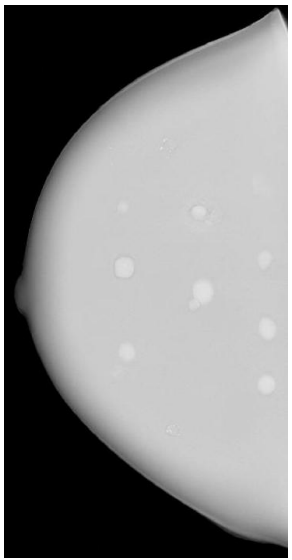
(a)



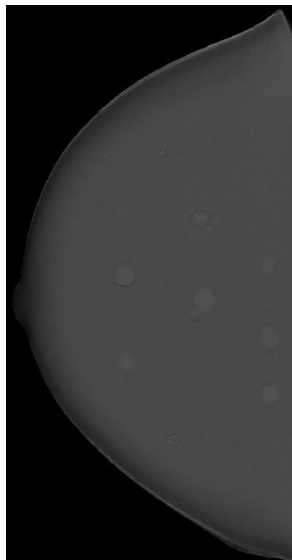
(b)



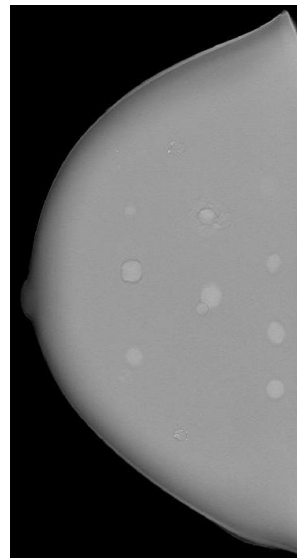
(c)



(d)

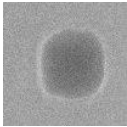


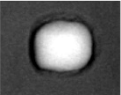
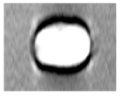
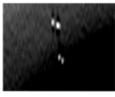
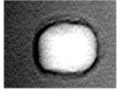
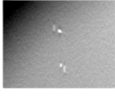
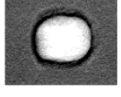
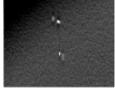
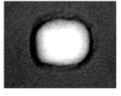
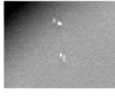
(e)

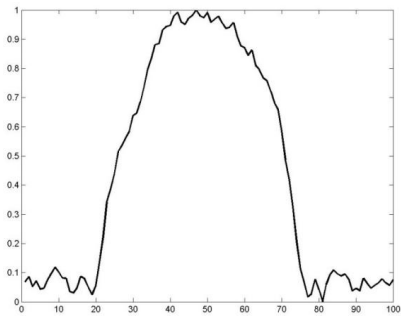


(f)

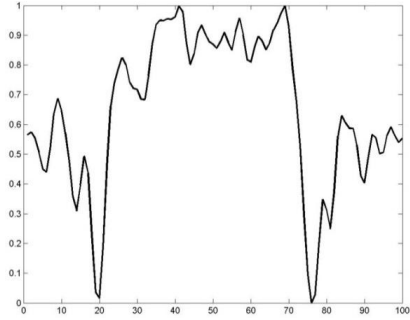
Figure 20. Reconstructed slice images. (a) BP. (b) FBP. (c) MITS. (d) MLEM. (e) OS-MLEM. (f) SART.

Mass	Micro-calcification
	
Figure 21. ROIs in central middle projection image	

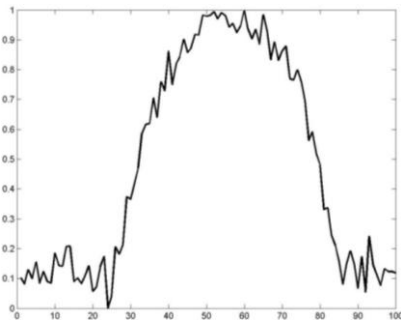
	Mass	Micro-calcification
BP		
FBP		
MITS		
MLEM		
OS-MLEM		
SART		
Figure 22. Reconstructed ROIs by different reconstruction algorithms.		



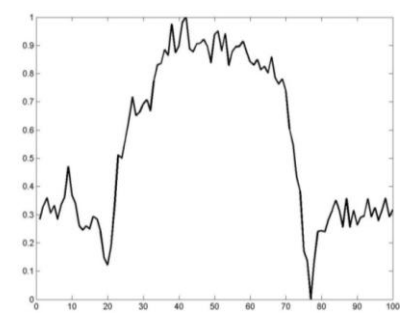
(a)



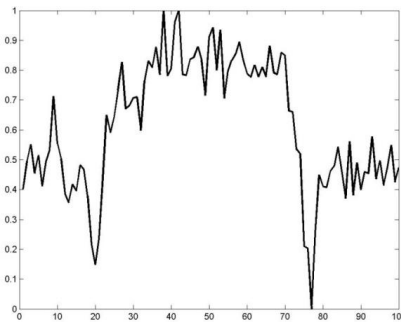
(b)



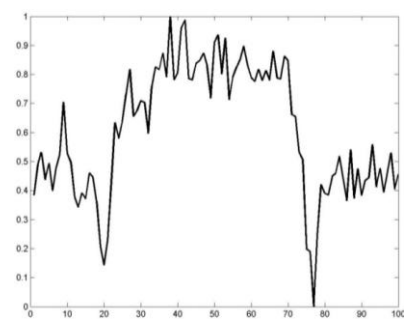
(c)



(d)



(e)



(f)

Figure 23. Line profiles of reconstructed mass ROIs. (a) BP. (b) FBP. (c) MITS. (d) MLEM. (e) OS-MLEM. (f) SART.

The main problem in tomosynthesis imaging is incomplete sampling. In the three-dimensional space,  $Z$  direction (depth) is less sampled than  $X$ - $Y$  direction. However, in order to increase the accuracy of  $Z$  direction, i.e., show the object at its original plane meanwhile remove it in other planes, we hope to eliminate out-of-plane artifact as much as possible.

Artifact spread function (ASF) reflects the ability of blurring out the out-of-plane objects. It has been used to describe the artifact suppression efficacy along the  $Z$  direction in breast tomosynthesis studies by Wu and Zhang (Wu et al 2004, Zhang et al 2006)

ASF is defined as the ratio of the CNR values between the off-focus plane and the in-focus plane:

$$ASF(z) = \frac{CNR(z)}{CNR(z_0)} \quad (\text{Eq. 24})$$

where  $z_0$  is the slice location of the in-focus plane of the object and  $z$  is the location of the other plane. The CNR value (Zhang et.al., 2006) is defined by

$$CNR = \frac{\mu_{object} - \mu_{background}}{\sigma_{background}} \quad (\text{Eq. 25})$$

where  $\mu_{object}$  and  $\mu_{background}$  are the average pixel intensity of the object and image background respectively, and  $\sigma_{background}$  is the root-mean-square noise value of pixel intensity in the image background.

The image background region for noise estimation is chosen as a 40\*40 pixel region far from all objects and the boundaries in the slice images, and at the same slice as the object under consideration. The mean pixel intensity of a mass is calculated in a

40\*40 pixel area enclosed within the relatively uniform central region of the mass. The selected masses were the same as in Figure 22.

The ROI for analysis of mass and micro-calcification, and the image background are the same as those described above for the calculation of CNR. Different algorithms have their implicit or explicit design to remove out-of-plane artifacts. Figure 24 shows the ASF curves for BP, Ray-tracing BP, MLEM, OS-MLEM and SART. OS-MLEM and SART show bigger CNR drop-offs, so they can remove out-out-plane artifacts better.

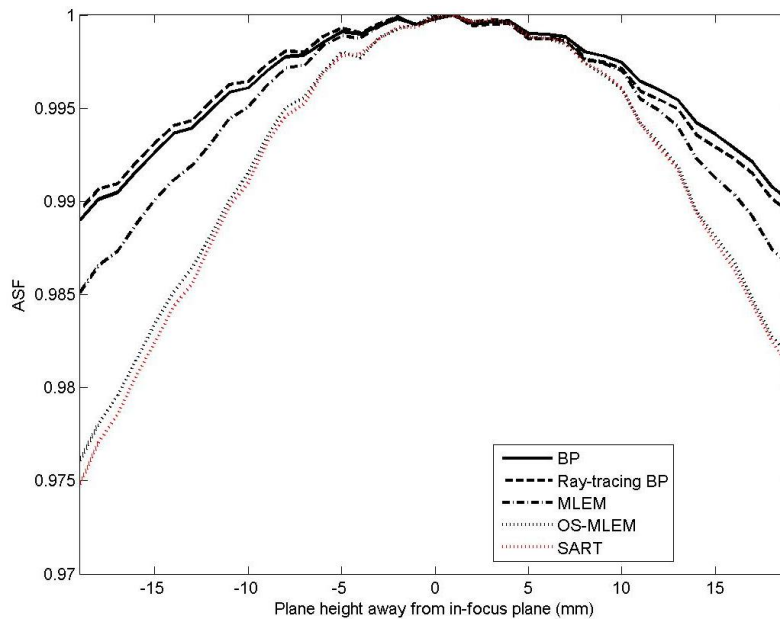


Figure 24. ASF curves of different image reconstruction algorithms with a biopsy training phantom.

## CHAPTER 3

### STATISTICAL VARIANTS OF POINT-BY-POINT BACK-PROJECTION

#### RECONSTRUCTION ALGORITHM

In point-by-point BP reconstruction algorithm, for the point  $p$  in reconstructed volume, when considering each pair of X-ray tube and projection image, we have one pixel value  $s$ . Now after finishing back-projection,  $N$  pixel values are acquired ( $N$  is the number of projection images). Considering the statistical properties of those  $N$  values, some alternative techniques may be utilized to further improve the image quality.

#### 3.1. STATISTICAL VARIANTS OF POINT-BY-POINT BACK-PROJECTION

##### ALGORITHM

##### **$\alpha$ -trimmed BP**

The  $\alpha$ -trimmed BP is removing the "extremity" values in the back-projected pixels. Sort all the pixel values in the back-projection images, remove the  $d/2$  lowest and the  $d/2$  highest gray-level values, and then calculate the mean value. The equation can be written as

$$s = \frac{1}{N-d} \sum_{i=d/2+1}^{N-d/2} I(B_i) \quad (\text{Eq. 26})$$

where the value of  $d$  can range from  $0$  to  $N-1$ . When  $d=0$ , the  $\alpha$ -trimmed method regresses to standard BP. If we choose  $d=N-1$ , it becomes a median BP. This technique is often used to remove noise in digital image processing, and it is called  $\alpha$ -trimmed method (Gonzalez and Woods, 2008). It has advantages in noise removal and near-boundary anti-aliasing.

## PCA-based BP

Principle components analysis (PCA) (Gonzalez and Woods, 2008) inspires us in the other way. It is a transformation from n-dimensional coordinate system to another m-dimensional one (generally  $m < n$ ). It is performed in such a way that a truncation of an input vector in the new coordinate system only causes a minimal square error, i.e. a minimal loss of information. PCA has served as a standard tool for a large diversity of data analysis and information visualization. Its feature of dimensional reduction provides a good way to generate a single reconstruction plane from multiple projection images while extracting the most important information. Naturally, in our task, we need to acquire one dimension from several projection images.

In order to compare these different BP algorithms, we used phantom and computer simulation experiments. For convenience, the point-by-point back projection is called standard BP. In the investigated multi-beam parallel tomosynthesis imaging system, 15 x-ray sources, operated at a voltage of 30 kV, were linearly fixed along a parallel line above the detector. The detector has a pixel pitch of 140  $\mu\text{m}$ . The image size is  $2048 \times 1664$ . The distance from the X-ray tubes to the detector (SID) is about 690 mm. The total view angle  $\theta$  is equal to  $15^\circ$ .

### 3.2. IMAGE RECONSTRUCTION WITH A BREAST BIOPSY TRAINING PHANTOM

A standard breast biopsy training phantom (CIRS company, 2010) as shown in Section 2.8 was used in this preliminary experiment. Low dosage projection images were obtained and reconstructed by different algorithms, including standard BP and its variants. One mass and one micro-calcification were selected as our evaluation samples.

Figure 25 shows reconstructed planes by different algorithms. Figure 26 shows reconstructed ROIs from three algorithms including standard BP,  $\alpha$ -trimmed BP, PCA-based BP respectively.

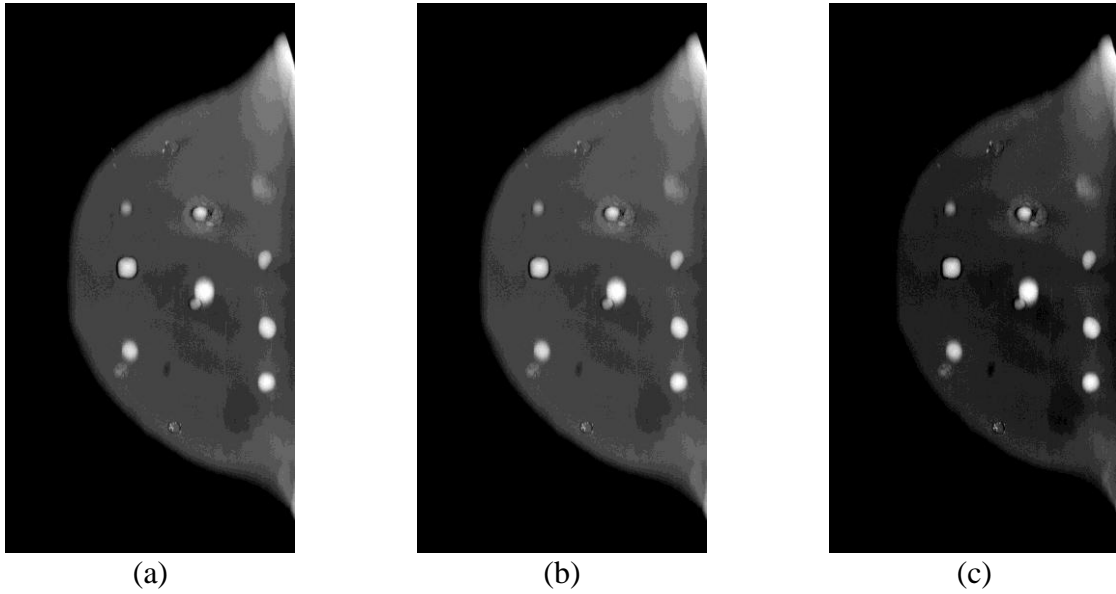


Figure 25. Reconstructed slice images. (a) Standard BP; (b)  $\alpha$ -trimmed BP; (c) PCA-based BP.

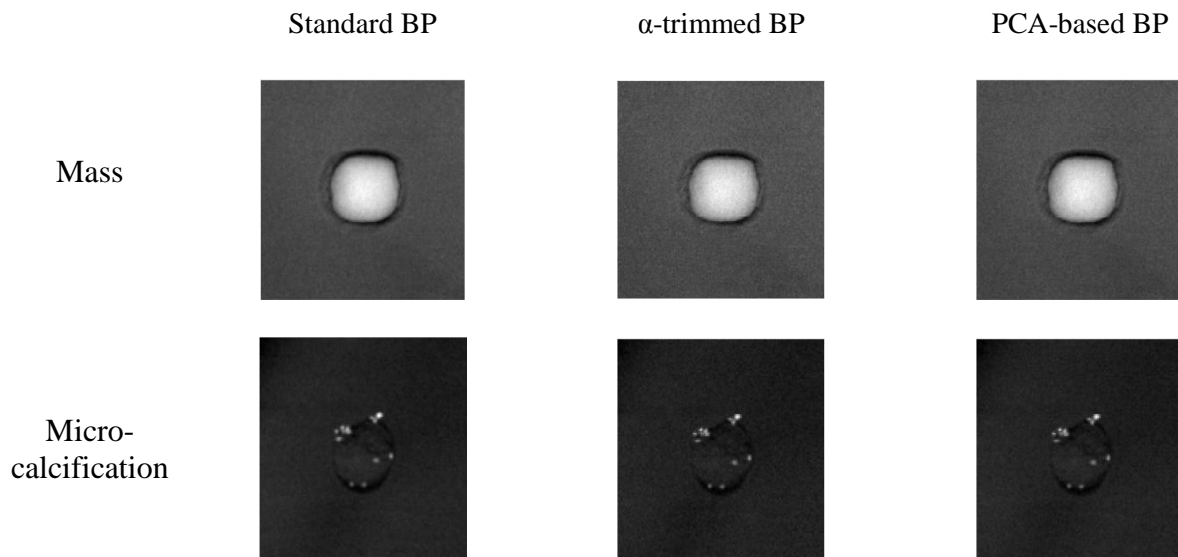


Figure 26. Reconstructed ROIs.

All the three reconstruction algorithms are capable of providing reconstruction of the phantom with the location, shape and edge information. In the micro-calcification cluster, due to the compression, not all the micro-calcification points were at the same planes. Some of them were out-of-plane. This reveals the 3D localization ability of tomosynthesis reconstruction.

### 3.3. SPHERE SIMULATION

A spherical object with the radius of 0.4 mm, placed at the height of 20 mm above the detector, was simulated and embedded in a uniform background as the target to test reconstruction algorithms. The linear attenuation coefficient of the simulated spherical object was set to 0.038 /mm, which referred to the linear attenuation coefficient of carcinoma tissue for 30 KeV photon energy (Guimarães et al 2009). Ray-tracing method was used to model the X-ray attenuation.

Three groups of simulation were conducted to test the response of the algorithms. In our simulation of Group #1, a solid sphere was put in the center above the detector plane. The background was uniform and we didn't add any noise to the simulated data. In our simulation of Group #2, mixed noise was added to each projection image of Group #1 to reveal the performance of noise removal with different reconstruction algorithms. In our simulation of Group #3, a solid sphere was placed near the boundary of reconstruction plane. Because of the limited size of the detector, the sphere may be projected out of the detector for some x-ray sources. This simulation can give us a demonstration for the situation when the object is near the boundary and some portions of the object may go beyond the detector when projected.

The above three BP algorithms were then applied to reconstruct the images acquired from simulated tomosynthesis datasets. A reconstruction plane spacing of 1 mm was used. Normalized in-plane and out-of-plane pixel intensities in the spatial domain were analyzed for the evaluation. The line profiles through the center of the sphere along the horizontal axis were provided to compare the out-of-plane blur and in-focus amplitude.

Figure 27, 28 and 29 are the line profile results from standard BP,  $\alpha$ -trimmed BP and PCA-based BP correspondingly. For each reconstruction algorithm, two line profiles of normalized pixel intensities on the defined reconstruction planes passing through the center of simulated spherical object ( $Z=20$  mm and  $Z=23$  mm away from the detector) were illustrated. Solid lines are the ones that pass through the center of the simulated sphere and are considered as in-plane line profiles. Dotted lines are the ones that are parallel to the in-plane lines but 3mm higher, and they are considered as out-of-plane line profiles. X-axis represents the pixel location on reconstructed plane and an 81-pixel region of interest was shown for clarity. Y-axis represents the pixel intensity on a reconstructed image. For each reconstruction algorithm, the pixel intensities were normalized based on the in-plane ( $Z=20$  mm) reconstruction response.

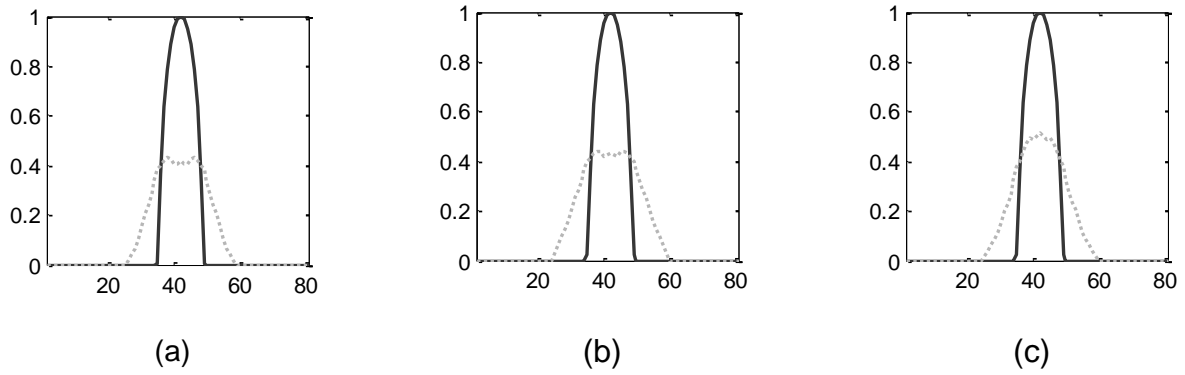


Figure 27. Line profiles of reconstructed spheres in the simulation of Group #1. (a) Standard BP; (b)  $\alpha$ -trimmed BP; (c) PCA-based BP.

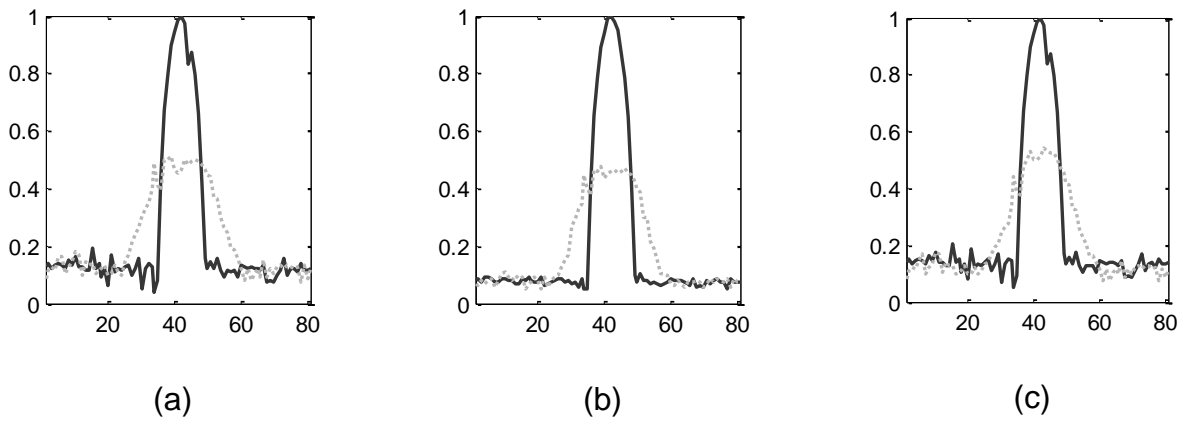


Figure 28. Line profiles of reconstructed spheres in the simulation of Group #2. (a) Standard BP; (b)  $\alpha$ -trimmed BP; (c) PCA-based BP.

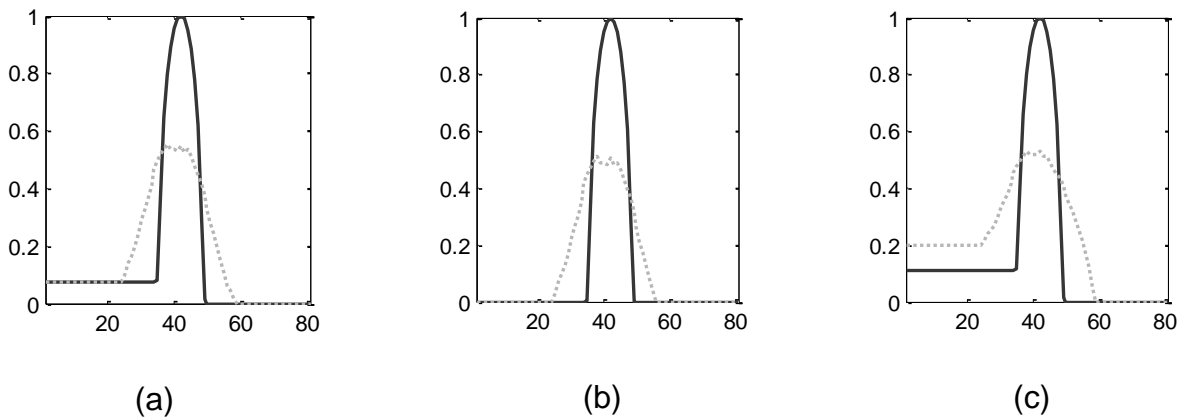


Figure 29. Line profiles of reconstructed spheres in the near-border sphere simulation of Group #3. (a) Standard BP; (b)  $\alpha$ -trimmed BP; (c) PCA-based BP.

As shown in Figure 27, results from  $\alpha$ -trimmed and standard BP are quite similar. The result of PCA-based BP has a little higher out-of-plane blur. In Figure 28, when the noise is present, the in-plane line profile of  $\alpha$ -trimmed BP is much smoother than the ones of standard BP and PCA-based BP. Figure 29 shows that  $\alpha$ -trimmed BP may reserve the shape of near-boundary object, while standard BP and PCA-based BP fail to reveal ambiguities when viewing the objects near the boundary of the reconstruction plane.

### 3.4. NPS MEASUREMENT

To measure the noise propagation in different BP variants as a function of spatial frequency, NPS(f) was tested by acquiring the projection images of a breast tissue equivalent phantom with the DBT prototype system. A standard phantom with the equivalent distribution of attenuation and scatter radiation in breast tissues was placed on the surface of the detector. The projection images were acquired by the multi-beam prototype system and reconstructed by the above three reconstruction algorithms.

In this section, The NPS(f) investigation about different algorithms used a 1D NPS line profile method (Zhang et al 2006). It cut the ROIs with 1024×1024 pixels from the reconstructed planes with the same height above the detector. Each ROI was evenly divided into 63 strips with a size of 1024×32 pixels. The adjacent strips were overlapped. For each strip, a line curve fitting was used to obtain an approximation to the true NPS. Finally, we extracted the frequency components from each strip and formed the smoothed NPS curves.

The reconstructed plane containing the ROI for NPS(f) estimation was 45 mm above the detector. The measurement of the 1D NPS was repeated on ten experiments

of the phantom at the same plane and the average of the repeated measurement was compared.

The average 1D NPS in the same selected area are shown in Figure 30 for the three reconstruction methods. The standard BP and  $\alpha$ -trimmed BP methods produced the essentially indistinguishable NPS( $f$ ) level in the reconstructed slice. PCA-based BP has higher spatial frequency response since it intends to maximize the information retrieval.

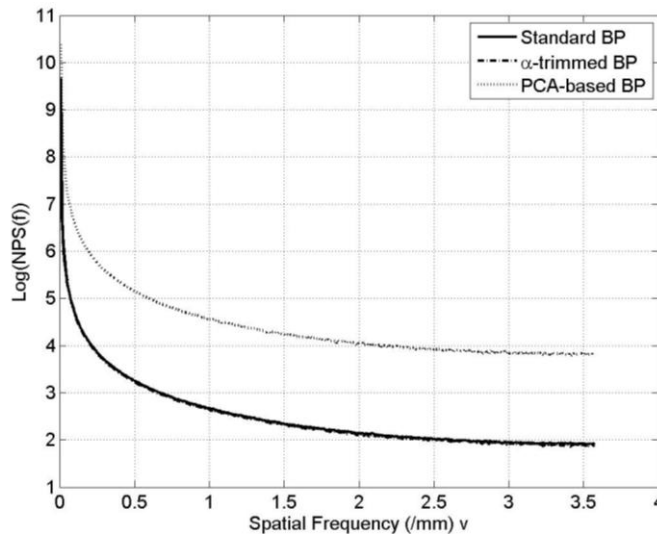


Figure 30. NPS curves of three BP variants.

### 3.5. MTF MEASUREMENT

To characterize signal propagation in different BP variants, MTF( $f$ ) was tested. We used an impulse response simulation method (Chen 2007c). In our measurement, an impulse, located at the center of the plane which is 45.0 mm above the detector, was computer simulated with the imaging configuration of the prototype system and then reconstructed by the above three algorithms. In MTF( $f$ ) calculation, the

reconstructed slices 45.0 mm above the detector were selected. FFT transform of the slices was calculated to extract frequency components and form the MTF curves.

In Figure 31,  $\alpha$ -trimmed BP has the maximal MTF(f) for all the frequencies. The 10% MTF(f) drop-off is 0.99 for traditional BP, 2.08 for  $\alpha$ -trimmed BP, and 1.34 for PCA-based BP. It shows that  $\alpha$ -trimmed BP can improve the sharpness of in-plane objects.

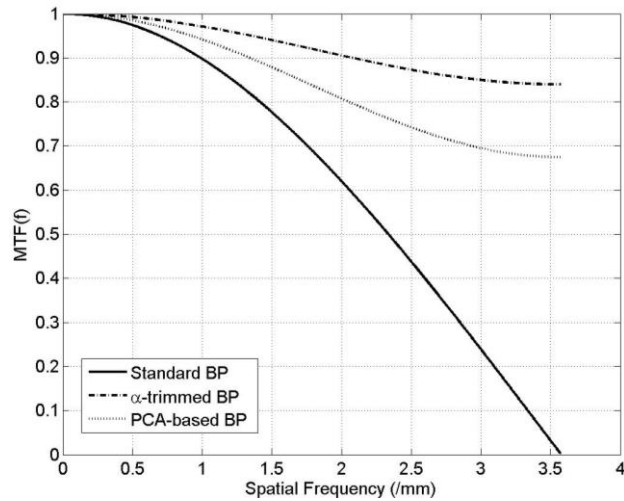


Figure 31. MTF curves of three BP variants.

### 3.6. SUMMARY

All the BP variants can provide clear reconstruction images and therefore provide solutions to breast tomosynthesis imaging. As a direct transformation method, standard BP works well in providing the three-dimensional reconstructed slice images. Standard BP intuitively calculates the mean values,  $\alpha$ -trimmed BP removes the extremity values, and PCA minimizes the information loss.

The  $\alpha$ -trimmed BP improves image quality based on signal and noise propagation analysis. It has the similar NPS(f) curve with standard BP but presents the

best MTF(f) response compared to standard BP and PCA-based BP. When the object in the reconstructed volume is projected beyond the detector,  $\alpha$ -trimmed BP may remove the ambiguity. However, it is important that the threshold of the  $\alpha$ -trimmed method should be carefully selected.

Zhao and Zhao (Zhao and Zhao 2008) investigated the signal and noise propagation of different FBP steps and suggested that BP had important influence on image quality. It is promising that image quality may be improved if we combine our BP variants with the deblurring filters.

## CHAPTER 4

### OPTIMIZATION OF IMAGE RECONSTRUCTION AND IMAGING CONFIGURATION FOR A MULTI-BEAM PARALLEL DIGITAL BREAST TOMOSYNTHESIS SYSTEM <sup>1</sup>

Breast tomosynthesis has caught a lot of attentions from both academia and industries due to its three-dimensional feature localization. With the advancement of tomosynthesis research by the academic communities, many medical imaging manufacturers are actively engaged in designing digital tomosynthesis prototype systems to prepare for the commercial usage and public sale. In order to pursue state-of-the-art technology in this field, new challenges emerge. Manufactures are eager to optimize their designs to produce decent imaging results to improve their competences. Doctors and patients are willing to determine which device and imaging methods are superior. Although the conventional physical measurement techniques of image quality metrics can be applied to the tomosynthesis imaging characterizations, it is urgent and essential to develop appropriate strategies to compare and evaluate tomosynthesis systems and image reconstruction algorithms (Dobbins 2000, Dobbins and Godfrey 2003, Dobbins et al 2006, Chen 2007b).

Currently, both partial iso-centric and parallel tomosynthesis imaging configurations exist in breast tomosynthesis image acquisition field. In other tomosynthesis imaging fields, scientists are developing various designs as well, such as parallel imaging configuration for chest tomosynthesis design and C-arm tomosynthesis for head imaging applications. With specific tomosynthesis application and image

<sup>1</sup> Part of this chapter is from the book chapter by Chen et al 2011.

reconstruction algorithms are very important to provide optimal system performance and image resolution. Especially, for imaging configuration optimization, the imaging configurations typically include a few configurable parameters of number of projection images (NP) and view angle (VA). Combinations of those configurable parameters vary with different systems and should be compared and optimized for system design. In order to compare those different imaging configurations for each tomosynthesis system, one needs to select a methodology to optimize the imaging configuration design to provide better resolution. This becomes an important optimization objective for researchers in digital tomosynthesis imaging field.

Another key objective in digital tomosynthesis imaging is the optimization and comparison of various tomosynthesis reconstruction algorithms. Tomosynthesis reconstruction algorithms take significant roles in transforming two-dimensional projection information into three-dimensional reconstructed object. Arbitrary number of reconstruction images can be generated with appropriate reconstruction algorithms. The main difficulty in developing an ideal tomosynthesis reconstruction algorithm comes from its incomplete sampling of tomosynthesis imaging. With tomosynthesis imaging, only a few limited-angle projection images are available as the foundation to generate reconstructed three-dimensional information. Therefore, in order to improve the solution of this problem of incomplete sampling, dedications to the optimization of reconstruction algorithms never stop.

The options which are considered to optimize our multi-beam parallel digital breast tomosynthesis prototype system include view angle (VA), number of projection images (NP) and reconstruction algorithms. However, several factors play essential

roles in the optimization tasks and some of them are associated together to some extent. The non-linearity property of digital tomosynthesis system brings difficulties to the image quality evaluation to optimize the reconstruction algorithms and imaging configurations. Therefore, it turns to be essential to find an effective methodology to enable scientists to optimize tomosynthesis imaging configurations and reconstruction in breast tomosynthesis imaging field. We will provide clear explanation of our methodologies in this chapter. Firstly, a linear imaging system analysis is applied to estimate MTF. Computer simulations of sphere and wire are then applied to compare the signal propagation, especially out-of-plane artifact removal. In next chapter, a systematic NEQ(f) analysis methodology will be presented to evaluate the system performance in frequency domain.

#### 4.1. LINEAR TOMOSYNTHESIS IMAGING ANALYSIS

In digital tomosynthesis image acquisition, digital detectors are used to record images as discrete arrays with limited intensity range. Spatial and temporal integral of the image irradiance are recorded. A detailed theory about image formation can be found in Barrett et al 2004.

In tomosynthesis reconstruction, reconstruction slices passing through an object are reconstructed based on a tomosynthesis dataset of X-ray projection images. Digital computers are usually used to compute the reconstruction. It is necessary to represent the actual continuous object as discrete set of numbers. A common way for the representation of the discrete small elements is pixels or voxels (Barrett et al 2004).

If ignoring the statistical nature of the imaging process, the mapping from the object  $o$  to a single projection image  $p$  can be written as (Barrett et al 2004):

$$p = h \times o \quad (\text{Eq. 27})$$

The mapping operator  $h$  can be either linear or nonlinear. The property of homogeneity in linear systems makes it easier to analyze than nonlinear ones. Here we begin with the assumption of linearity. In Fourier frequency domain, one can use

$$P = H \times O \quad (\text{Eq. 28})$$

to denote the imaging mapping.  $H$  is the Fourier transform of  $h$  and it represents the transfer function.  $p$  and  $o$  are the Fourier representation of the projection image  $p$  and the object  $o$  respectively.

To simplify the imaging configuration consideration, we extract a parallel pinhole tomosynthesis imaging system as shown in Figure 32. The central point  $o$  is located on the reconstructed plane  $s$ . Here one can consider it as a pinhole aperture. We have the projection image on the detector  $P$ . Under this assumption,  $S$  is a radiopaque plane with a small pinhole  $o$ . This input produces a replica of the X-ray source geometry on the detector with a Z-depth dependent scaling factor (Grant 1972).

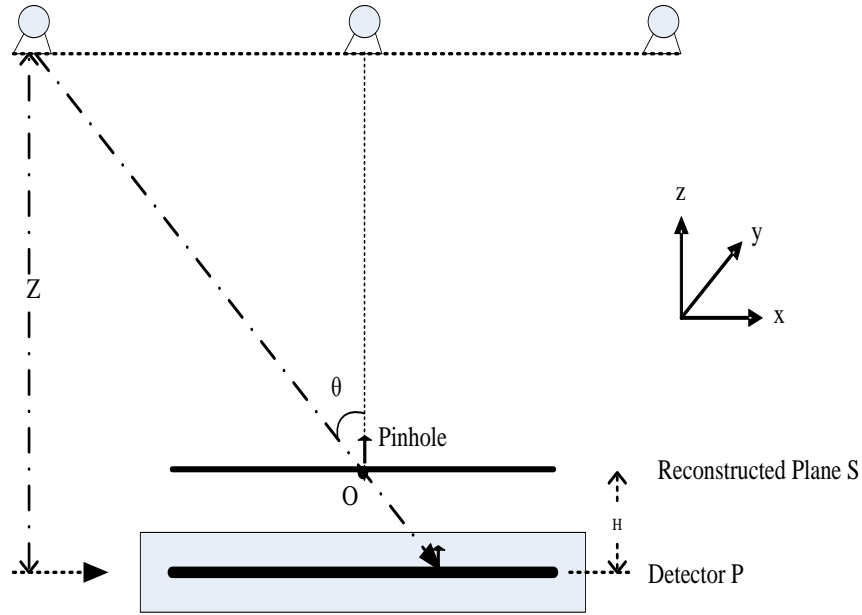


Figure 32. Impulse response imaging in tomosynthesis.

The line length of the replica of impulse-response on the detector is

$$\Delta = 2rZ \tan \theta = dZ \quad (\text{Eq. 29})$$

Where  $r$  is the magnification and  $\theta$  is the half of the total view angle. With the Fourier transform of the impulse-response function, the transfer function in Eq. 28 becomes (Grant 1972):

$$H(w_x | Z) = \frac{\sin(w_x dZ/2)}{(w_x dZ/2)} \quad (\text{Eq. 30})$$

It illustrates below properties (Grant 1972): (1) The blurring from undesirable planes is basically a linear filtering process; (2) The system's impulse response is a scaled replica of the scan configuration; (3) The position of the impulse response on the detector is Z-depth dependent.

For a linear tomosynthesis imaging configuration with N evenly distributed X-ray sources of parallel imaging configurations, the impulse response is simply a series of N infinitesimal points. The corresponding transfer function is extended into (Grant 1972):

$$H^N(w_x | Z) = \frac{1}{N} \frac{\sin N(\frac{\delta w_x}{2})}{\sin(\frac{\delta w_x}{2})} \quad (\text{Eq. 31})$$

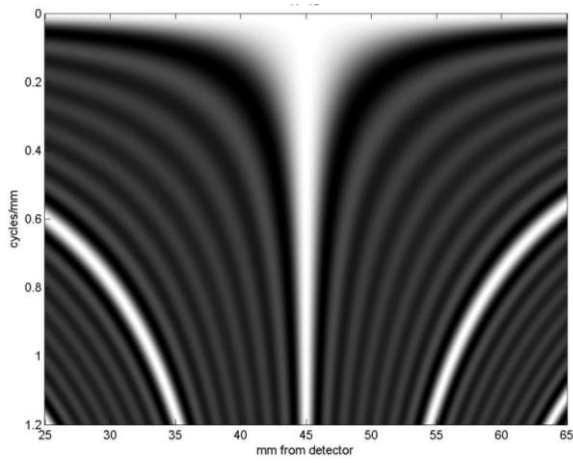
The transfer function becomes a series of peaks occurring at harmonics of the sampling frequency.

The transfer function is a direct quantitative measure of the system's ability to blur undesirable planes and provides a valid method of comparing imaging configurations. It also provides a means of evaluating the effectiveness of particular imaging configuration before setting up the actual measurement (Godfrey et al 2006).

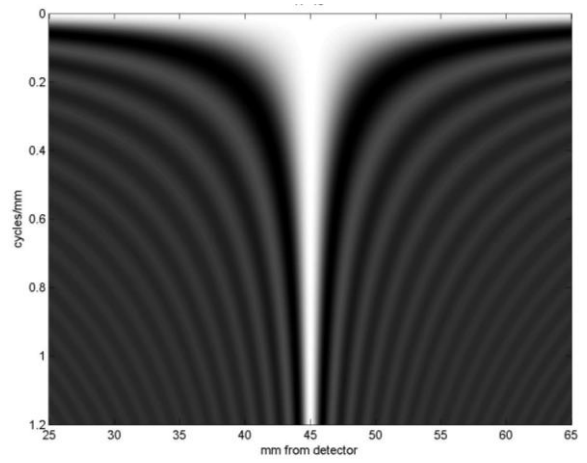
Grant's theory provides a good linear analysis tool to model the signal propagation in blurring-out reconstruction method. Typically, SAA, BP, FBP and MITS can get practical information from this method. Godfrey et al (Godfrey et al 2006) applied Grant's results and presented the MTF analysis results by varying the view angle and plane separation for the optimization of a chest tomosynthesis system. According to Godfrey's analysis, the blurring out algorithms suppress out-of-plan signal by increasing the in-plane signal, so an ideal blurring out algorithm should work like an extreme low-pass filter which keeps only DC frequency components. He demonstrated that out-of-plane artifacts can be suppressed with increased number of projection images.

We applied pin-hole linear tomosynthesis imaging theory to analyze our multi-beam digital breast tomosynthesis system. Figure 33 shows the MTF with  $28^\circ$  view angle and different numbers of projection images. Figure 34 shows the MTF with  $14^\circ$  view angle and different numbers of projection images. In Figure 33, with the increase of number of projection images, contours located off the main MTF peak get suppressed and the middle and high frequencies decrease. In Figure 34, because of very small view angle, the phenomenon is not as obvious as in Figure 33. The results suggest that out-of-plane objects will be better suppressed as number of projection images increase. On the other hand, as shown in the figures, for the same number of projection images, if view angle increases, denser contours appear. These results are coincident with later results of simulation experiments.

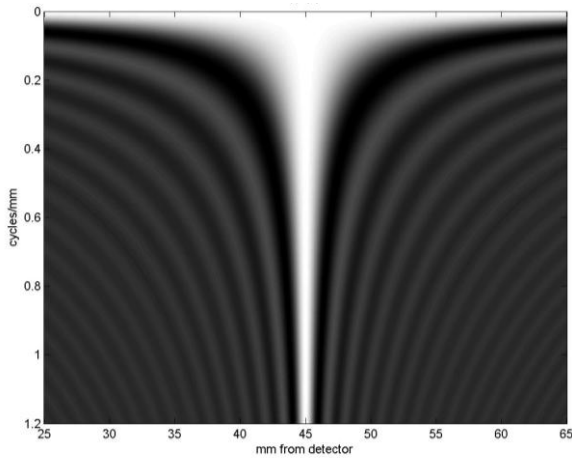
The change of DC components can also be observed from the line profile figures. Figure 35 shows the line profiles for the imaging configuration of projection image number 15 and view angle  $14^\circ$ . The DC decreases with the increase of the sampling frequency in slice thickness. It means that if we decrease the slice thickness, the out-of-plane artifacts will be better reduced. The same conclusion can be drawn from Figure 36.



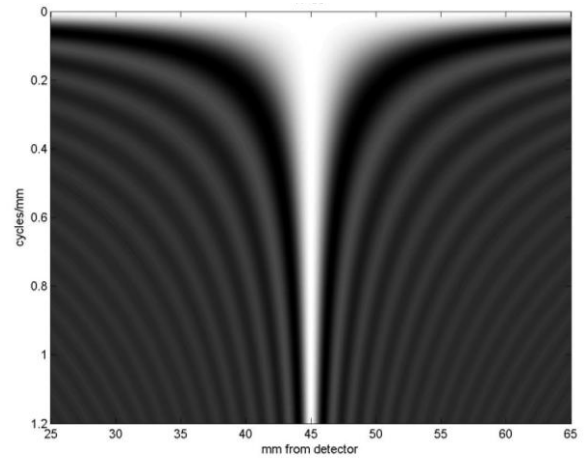
(a)



(b)

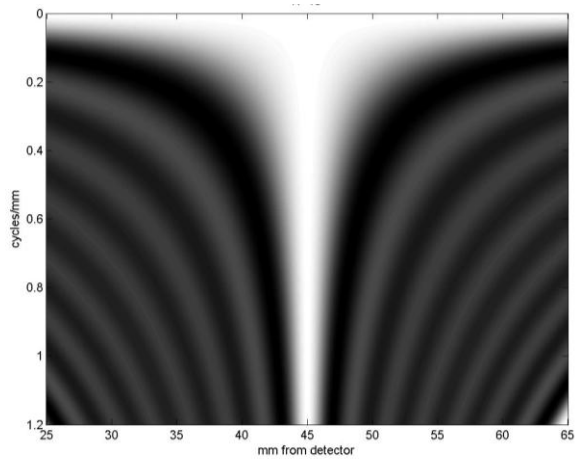


(c)

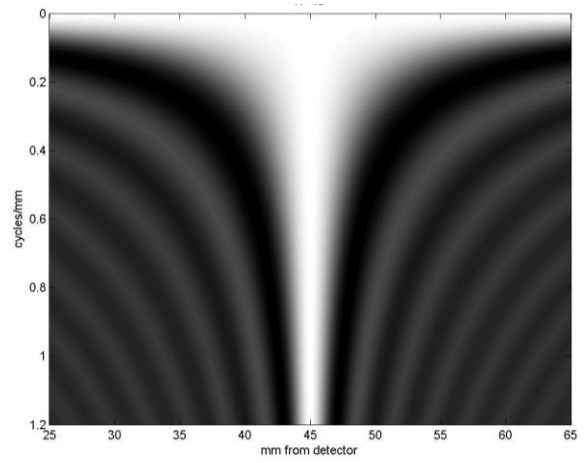


(d)

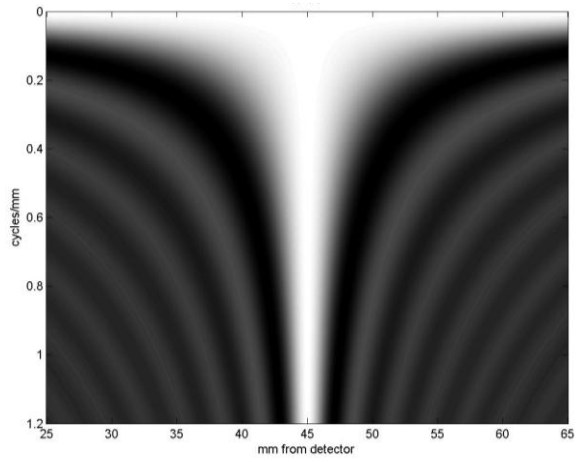
Figure 33. MTFs of different imaging configurations with the same view angle  $28^\circ$ . (a) NP = 15; (b) NP = 43; (c) NP = 71; (d) NP = 99.



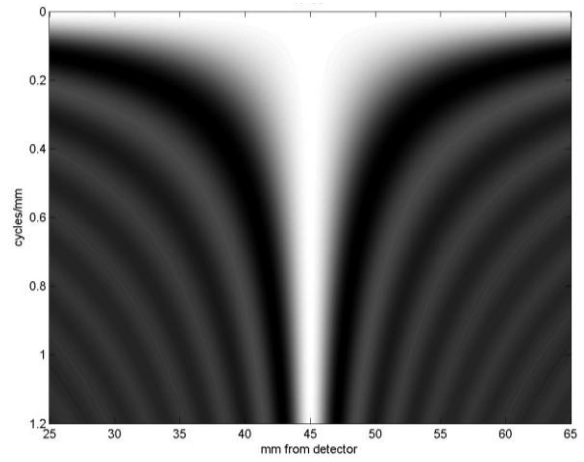
(a)



(b)



(c)



(d)

Figure 34. MTFs of different imaging configurations with the same view angle  $14^\circ$ . (a) NP = 15; (b) NP = 43; (c) NP = 71; (d) NP = 99.

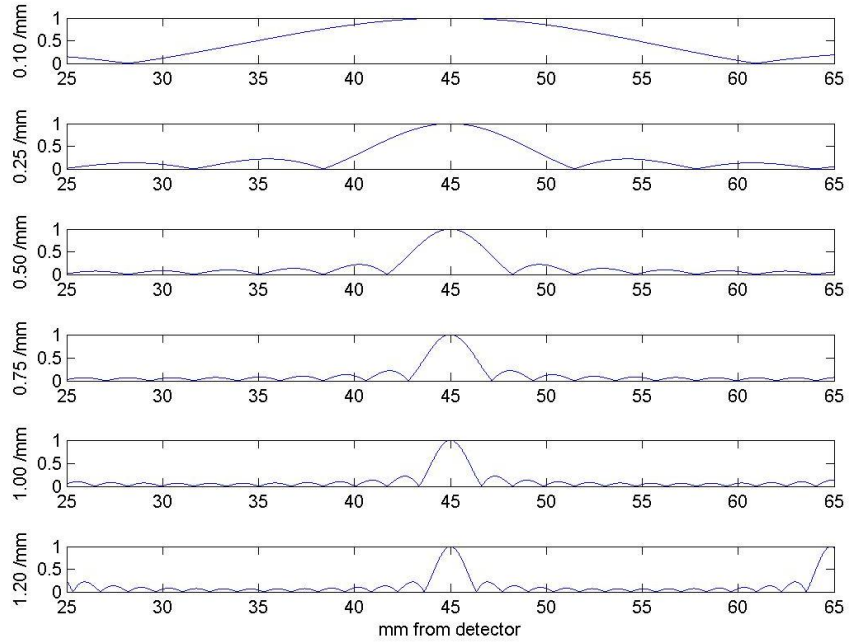


Figure 35. Line profiles of MTF with different slice thickness in the imaging configuration (NP = 15, VA = 14°).

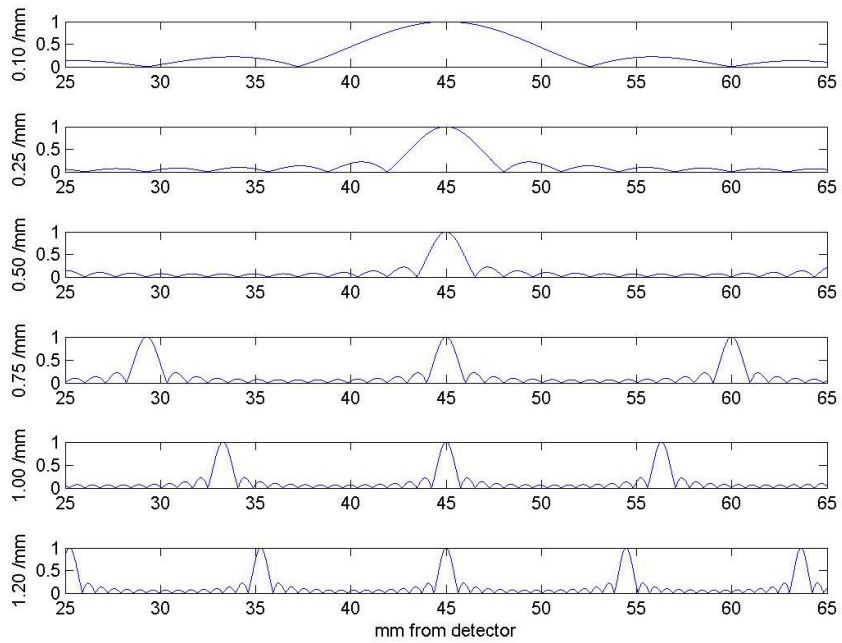


Figure 36. Line profiles of MTF with different slice thickness in the imaging configuration ( NP = 15, VA = 28°).

In the paper (Zhao et al, 2008), a three-dimensional cascaded linear system model of digital breast tomosynthesis was proposed. A flow chart about the propagation of signal and noise was drawn in the paper. Although the DBT system is not strictly linear, the linear system analysis including image acquisition and FBP image reconstruction was employed to estimate the propagation of signal and noise. The characterization analysis based on spatial frequency dependent 3D pre-sampling MTF, NPS and DQE was used to optimize the system design.

Linear analysis of tomosynthesis imaging configuration provides us a practical tool to optimize the system performance. However, we must point out that it also has some limitations. Many detectors are non-linear or approximately linear over a restricted range of inputs (Dobbins 2000). Meanwhile, some reconstruction algorithms are inherently non-linear, for example, MLEM reconstruction algorithm (Wu et al 2003). Nonlinearities may be either global or local. It may appear and influence tomosynthesis design in many aspects. Future investigations are necessary to enhance our development when we utilize these linear system analysis tools (Godfrey et al 2006; Zhou et al 2008; Hu et al 2008).

#### 4.2. SPHERE SIMULATION

This simulation was dedicated to evaluating the removal of out-of-plane artifacts with different imaging configurations and reconstruction algorithms. A spherical object with the radius of 400  $\mu\text{m}$ , placed at the center of a plane with the height of 20 mm above the detector, was simulated and embedded in non-uniform background as the target to evaluate the imaging configuration and reconstruction algorithms. Ray-tracing

method was used to calculate the X-ray attenuation. The imaging geometry follows Figure 37. The X-ray tubes were placed horizontally, and the horizontal blur dominates the blur of the reconstructed planes, so the line profile through the center of the sphere along the horizontal axis was provided to compare the out-of-plane blur and in-focus peak sharpness.

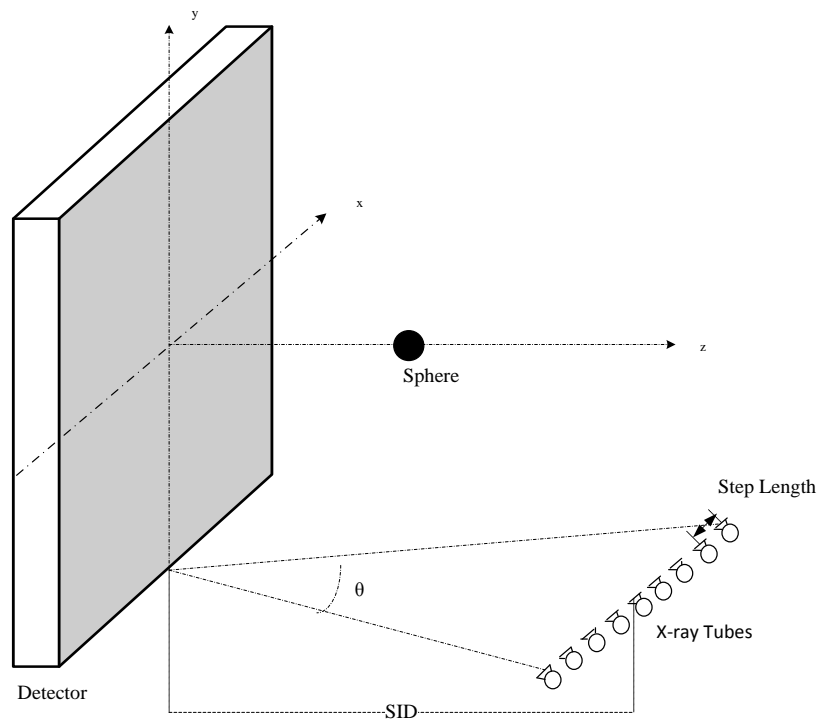


Figure 37. Sphere simulation

The linear attenuation coefficient of the simulated spherical object was 0.38 /cm, which referred to the linear attenuation coefficient of carcinoma tissue for 30 KeV photon energy (Guimarães et al 2009). Different parallel imaging configurations were independently simulated.

The five representative algorithms (BP, FBP, MITS, MLEM and SART) were then applied to simulated tomosynthesis datasets to reconstruct images. A reconstruction plane spacing of 1 mm was used. Normalized in-plane and out-of-plane pixel intensities in the spatial domain were analysed for the evaluation.

Figure 38, 39, 40, 41 and 42 are the line profile results from BP, FBP, MITS, MLEM and SART correspondingly. For each reconstruction algorithm, two line profiles of normalized pixel intensities on the defined reconstruction planes passing through the center of simulated spherical object ( $z=20$  mm and  $z=23$  mm away from the detector plane) were illustrated. Solid lines are the ones that pass through the center of simulated spherical object and they are considered as in-plane line profiles. Dotted lines are the ones that are correspondingly parallel to the in-plane lines but 3mm higher, and are considered as out-of-plane line profiles.

X axis represents the pixel location on reconstructed plane and a 101-pixel region of interest was shown for clarity. Y axis represents the pixel intensity on reconstructed image. For each reconstruction algorithm, the pixel intensities were normalized based on the in-plane ( $z=20$  mm) reconstruction response accordingly.

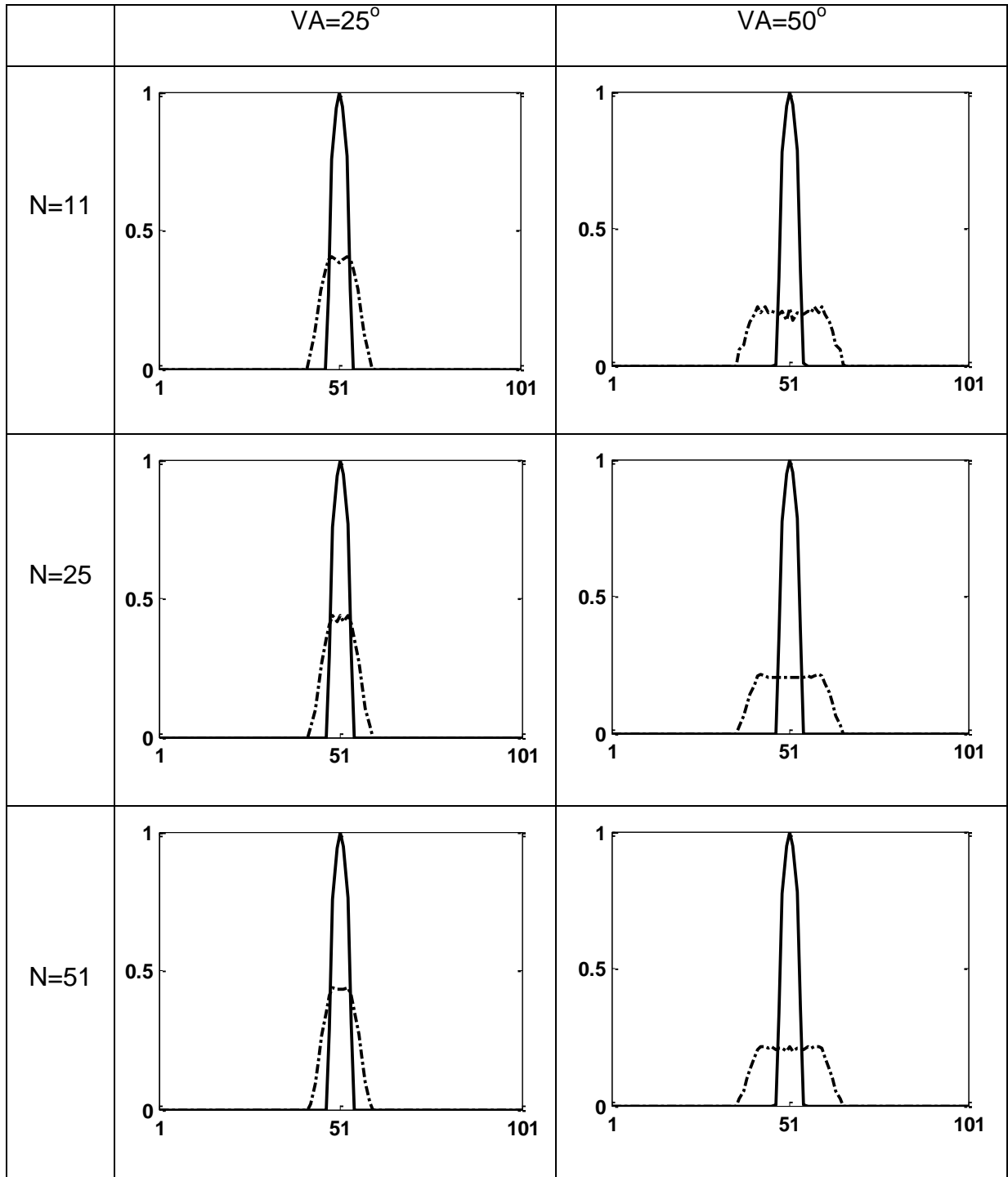


Figure 38. Line profiles of BP reconstructed spheres. Solid lines were extracted from the plane 20 mm above the detector. Dotted lines were extracted from the plane 23 mm above the detector.

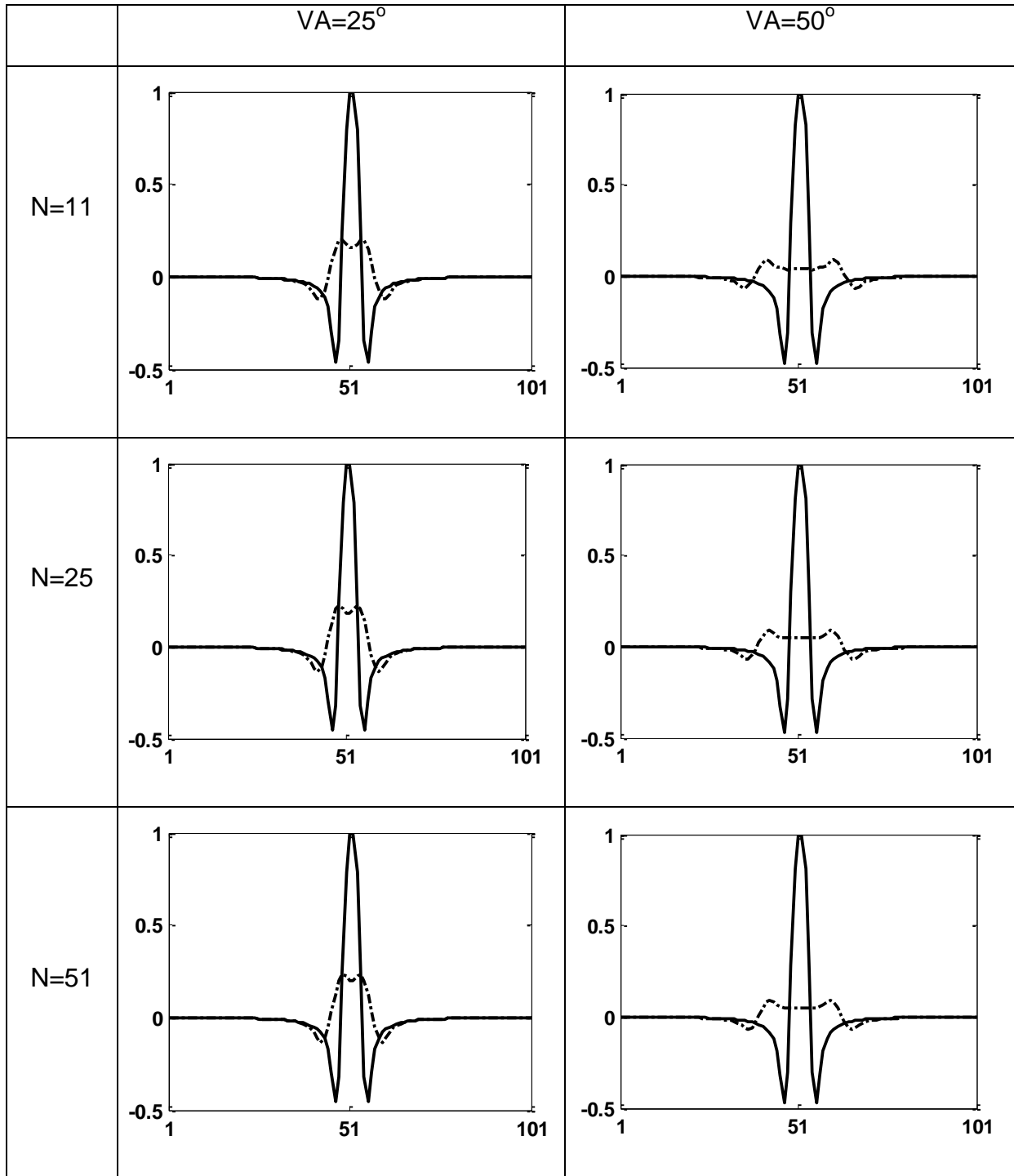


Figure 39. Line profiles at FBP reconstructed spheres. Solid lines were extracted from the plane 20 mm above the detector. Dotted lines were extracted from the plane 23 mm above the detector.

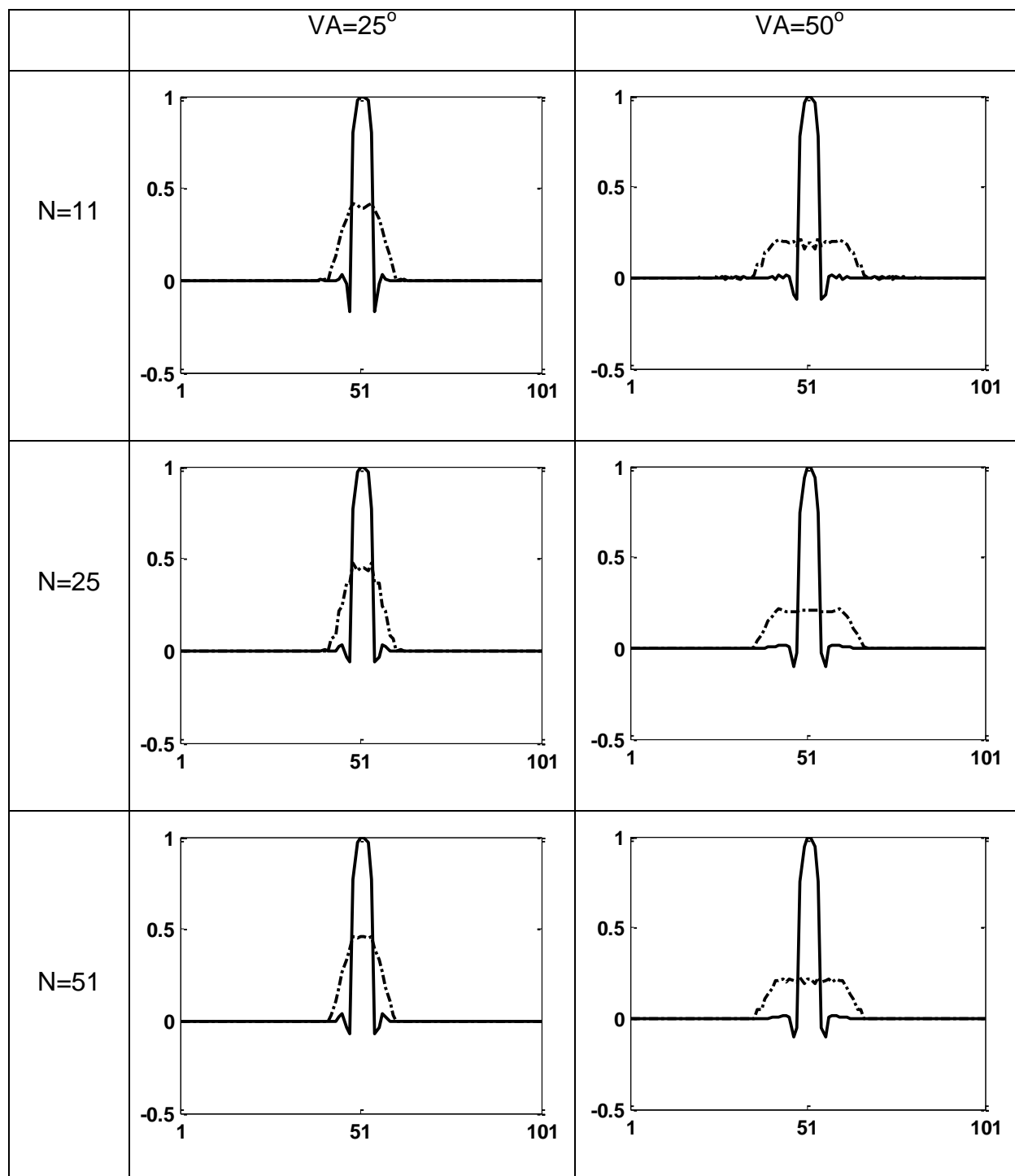
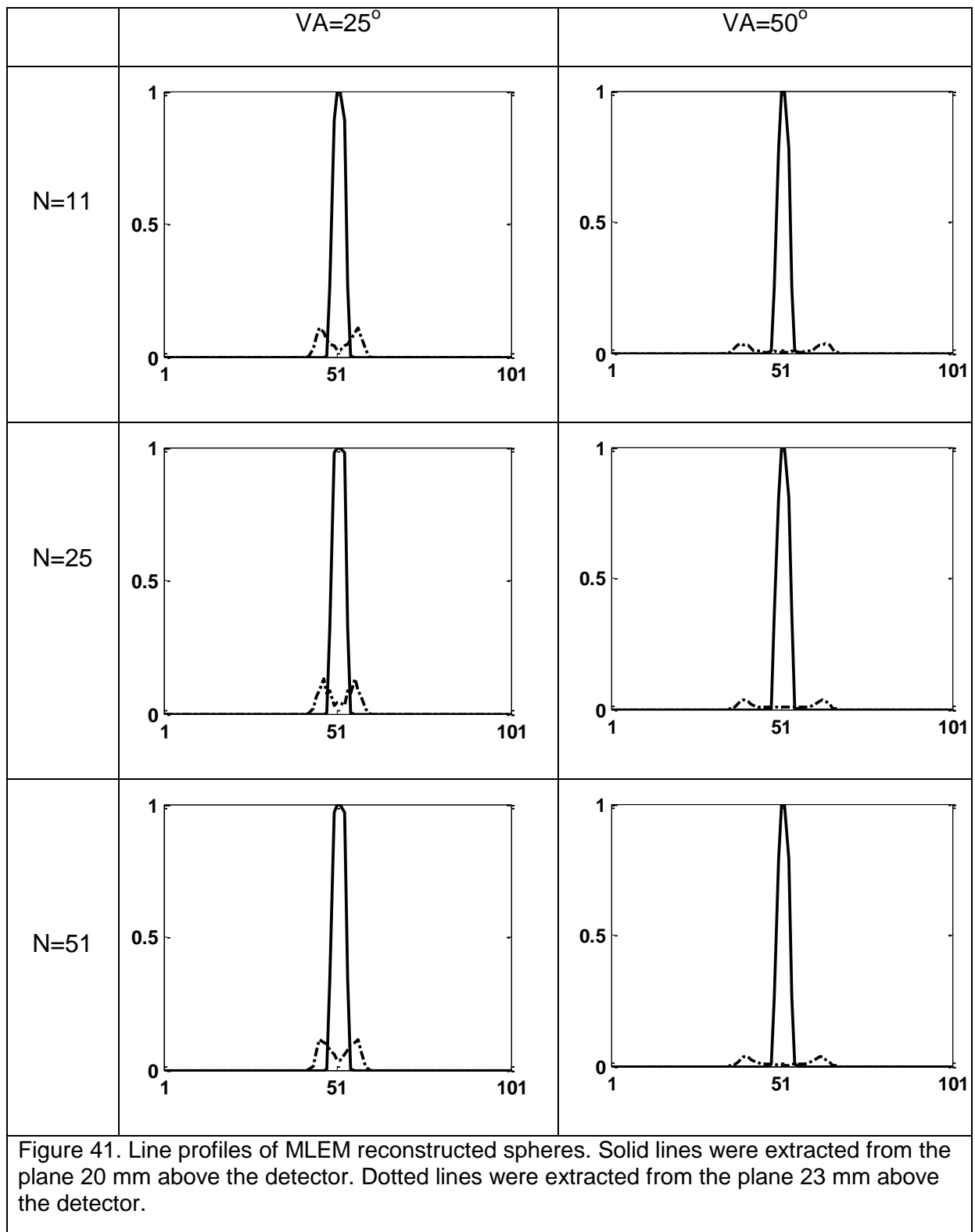


Figure 40. Line profiles of MITS reconstructed spheres. Solid lines were extracted from the plane 20 mm above the detector. Dotted lines were extracted from the plane 23 mm above the detector.



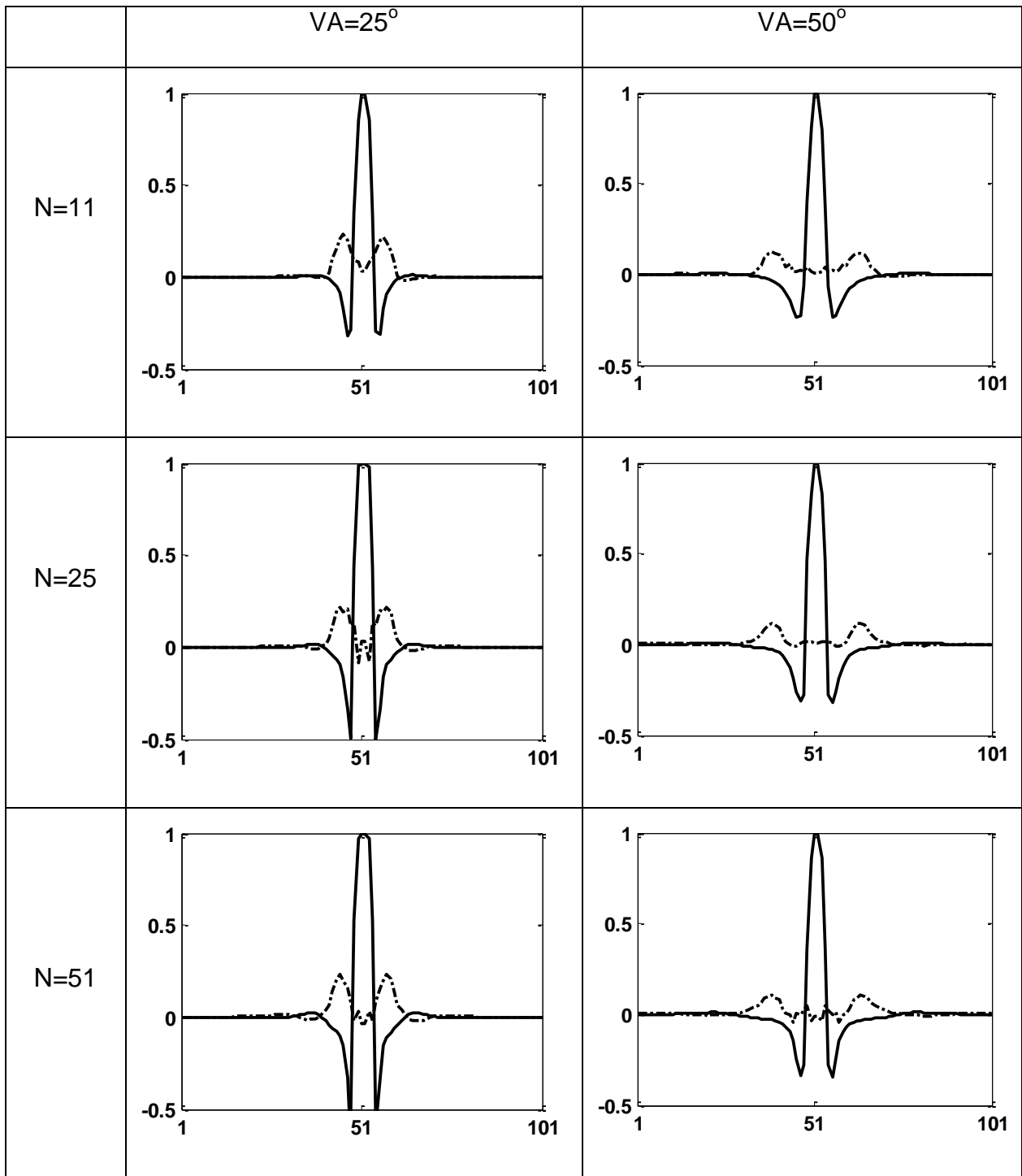


Figure 42. Line profiles of SART reconstructed spheres. Solid lines were extracted from the plane 20 mm above the detector. Dotted lines were extracted from the plane 23 mm above the detector.

As shown in the figures, all five representative algorithms were able to reconstruct three-dimensional information of the simulated object. For in-plane performance with solid lines, FBP, MITS and SART algorithms show edge enhancement phenomena. The edge enhancement also exists for the partial iso-centric tomosynthesis imaging configuration, which is common for the current breast tomosynthesis commercial prototype systems.

For out-of-plane performance with dotted lines, big view angle contributes to suppress the out-of-plane blur.

### 4.3. WIRE SIMULATION

Wire simulation (Balla et al 2010) was done to see how the above reconstruction algorithms and imaging configurations differ from each other based on the impulse response characterization. The experiment referred to the method of optimizing chest tomosynthesis system by Godfrey et. al. (Godfrey et al 2006). To evaluate the effects of variation in VA and NP, 11, 25 and 51 projection images of a very thin wire running vertically through the image space, whose depth varied from  $z=30$  mm to  $z=60$  mm from the bottom to top were simulated. Imaging geometry of Figure 43 was used. Each point on the simulated wire was considered an impulse. Simulated acquisition allowed the generation of the noise-free projection images that contained only a single impulse for each column in the image.

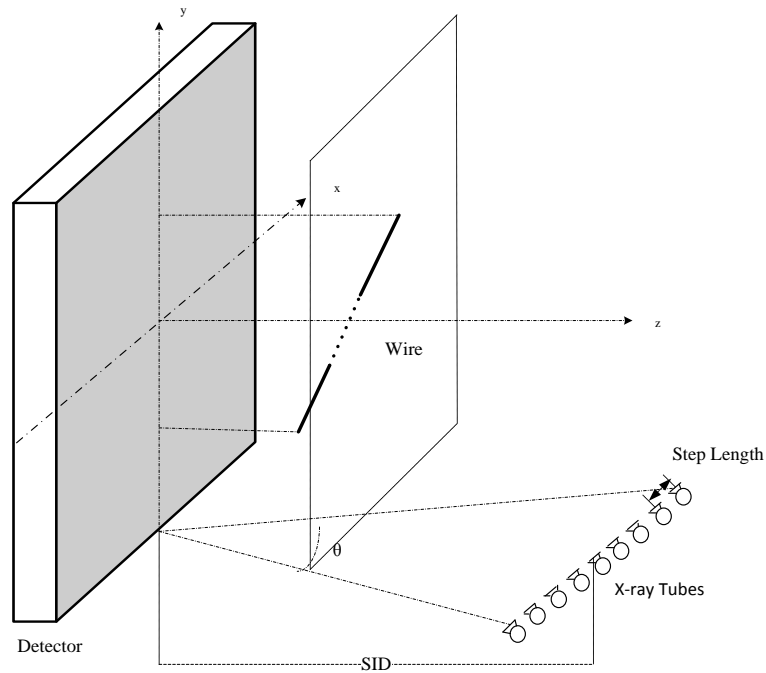


Figure 43. Wire simulation.

The above five reconstruction algorithms were used to reconstruct 30 evenly spacing planes from 30 mm to 59 mm above the simulated detector. On the reconstructed slices, we selected the position of the impulse response of the middle plane 45 mm high as the in-plane response. The impulse responses along the selected rows on all the reconstructed planes were displayed and evaluated.

Figure 44-48 shows the performance with different imaging configurations and reconstruction algorithms. Numbers of projection images are 11, 25 and 51. View angles are  $25^\circ$  and  $50^\circ$ .

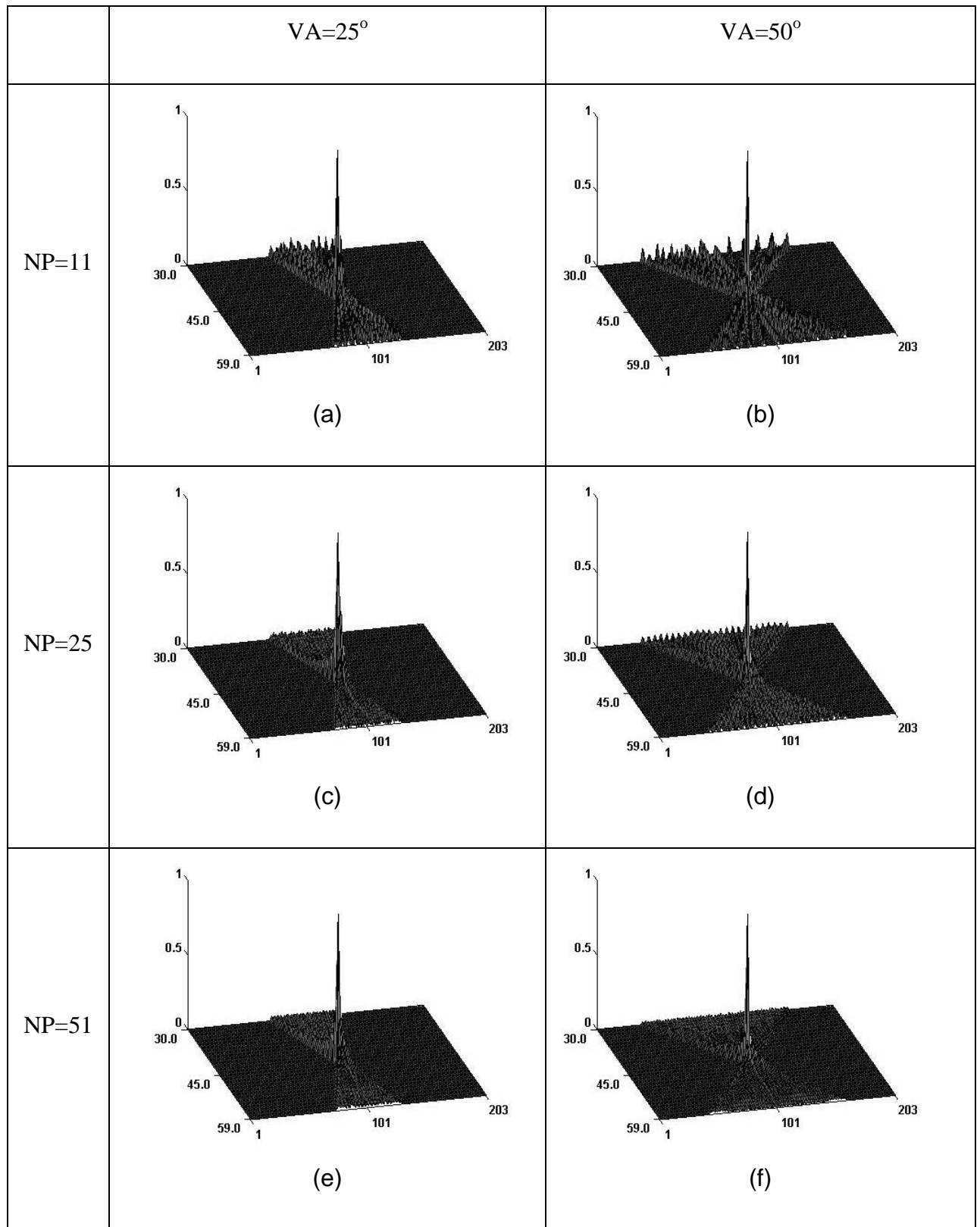


Figure 44. Impulse responses of wire simulation with BP reconstruction.

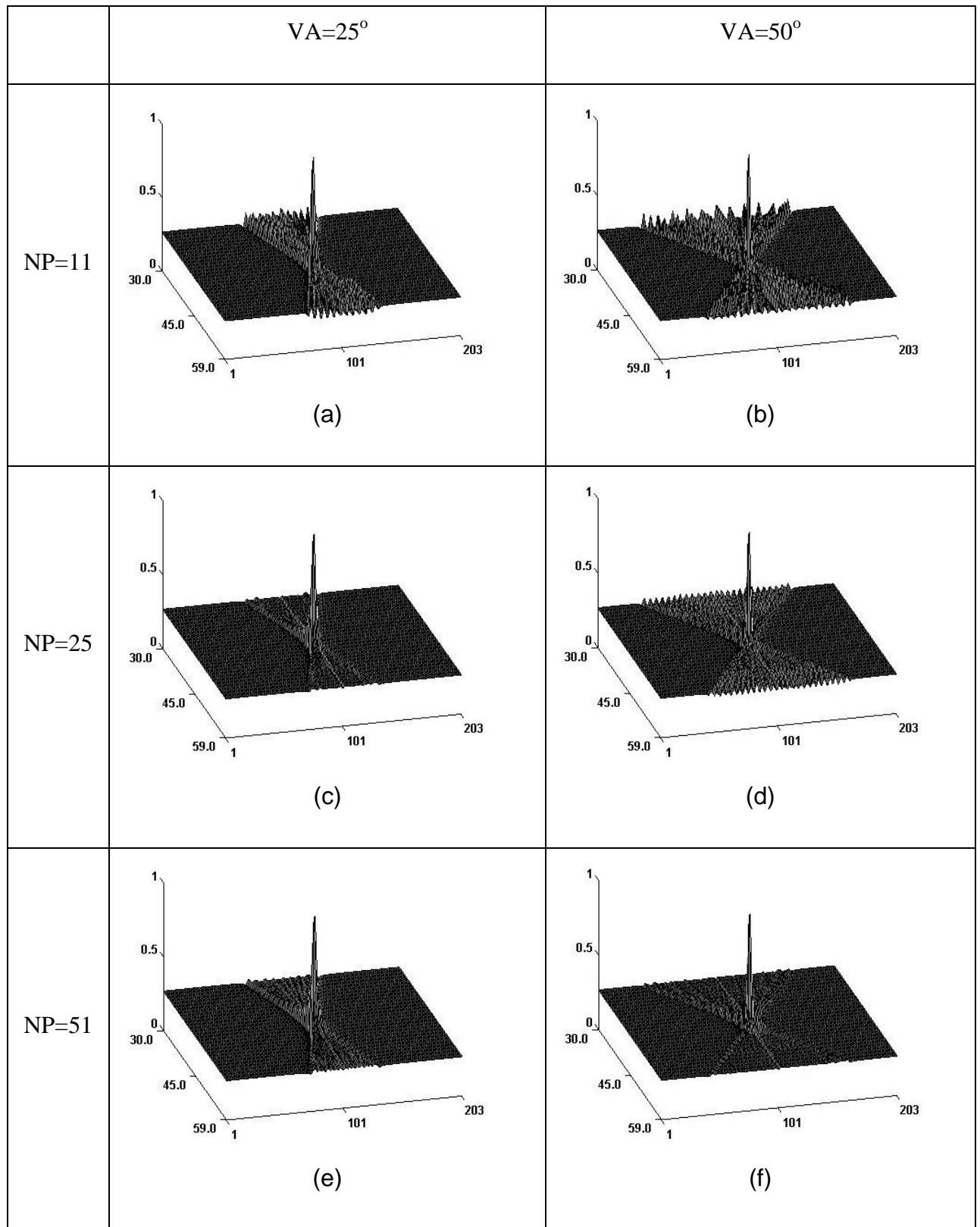


Figure 45. Impulse responses of wire simulation with FBP reconstruction.

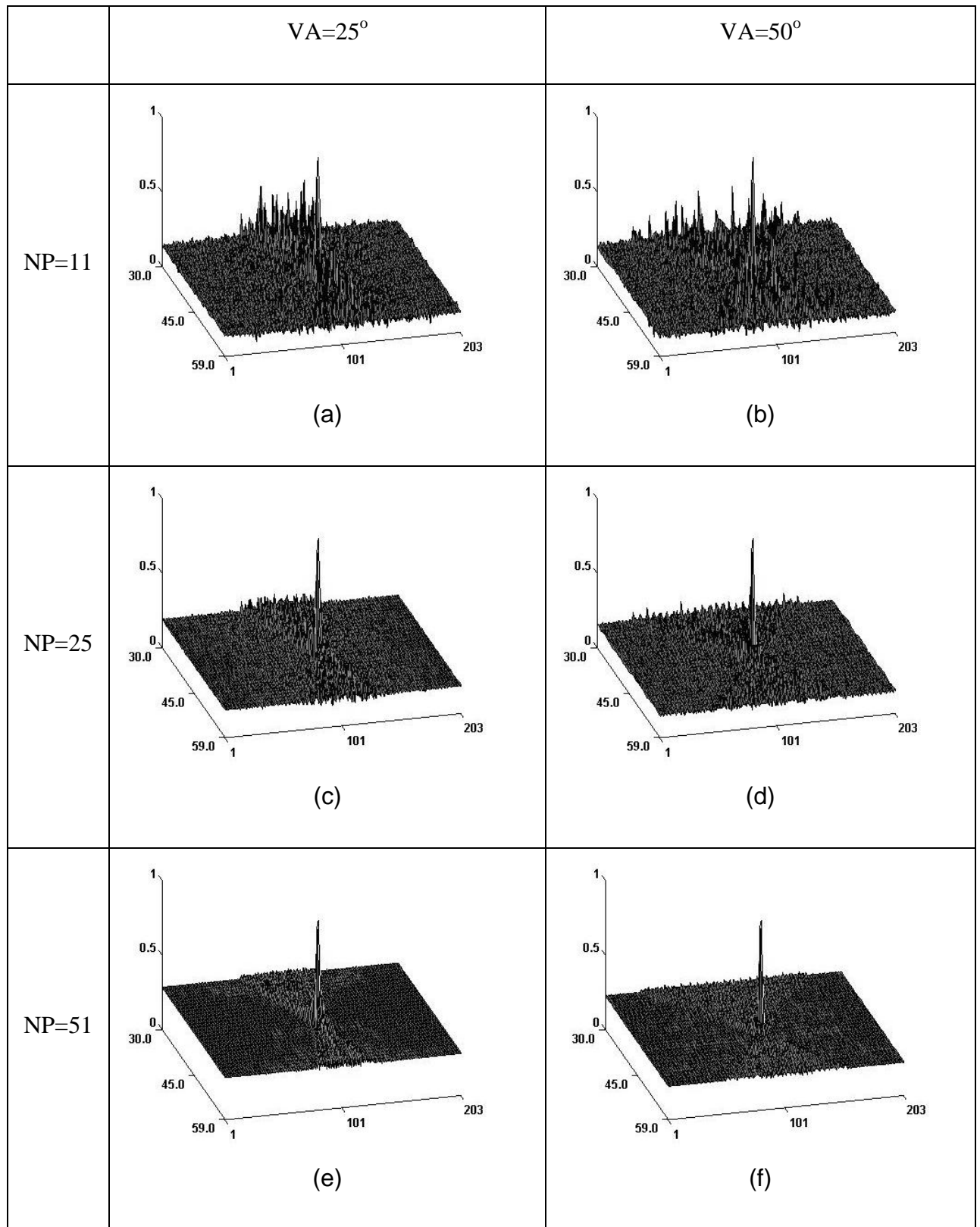


Figure 46. Impulse responses of wire simulation with MITS reconstruction.

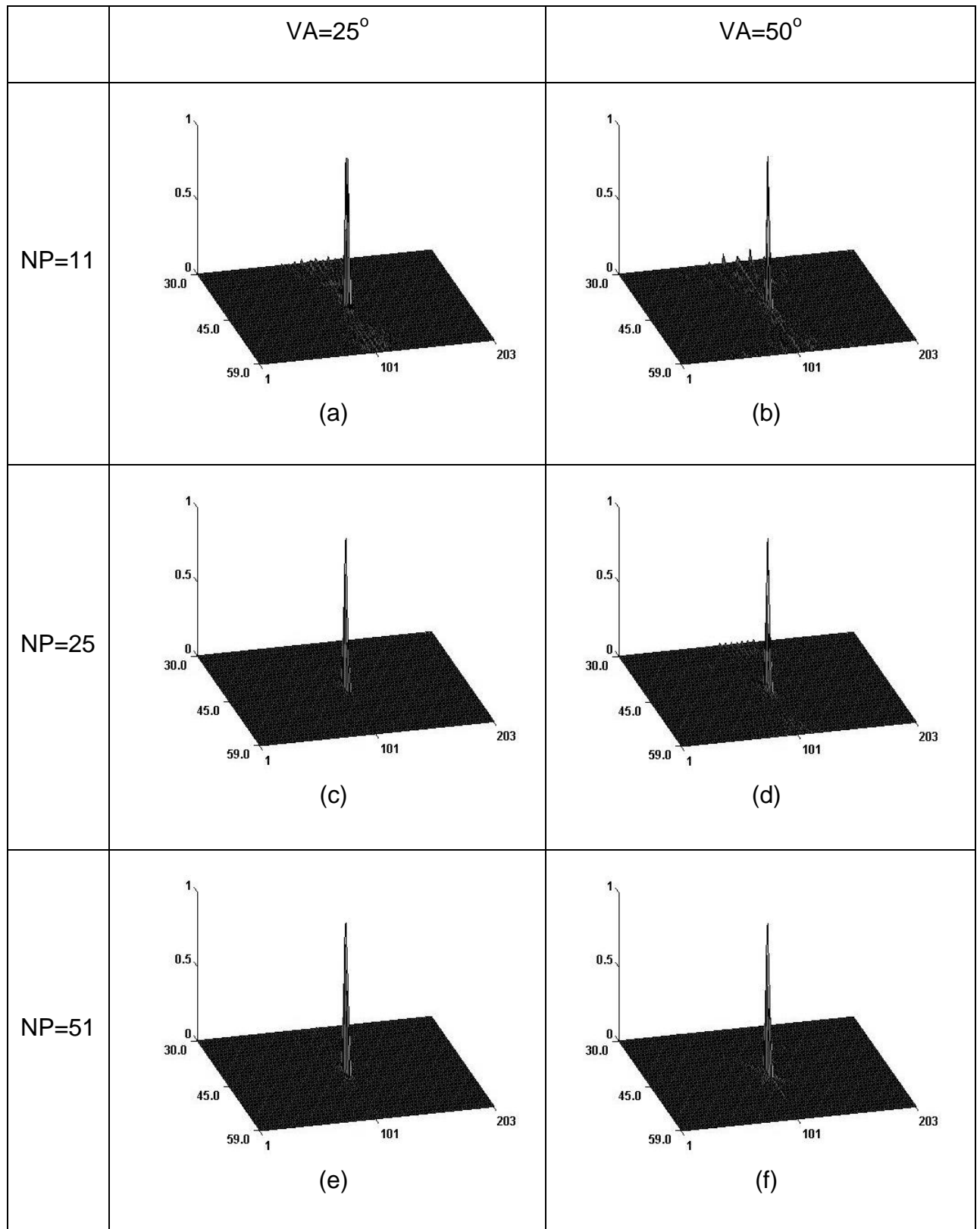


Figure 47. Impulse responses of wire simulation with MLEM reconstruction.

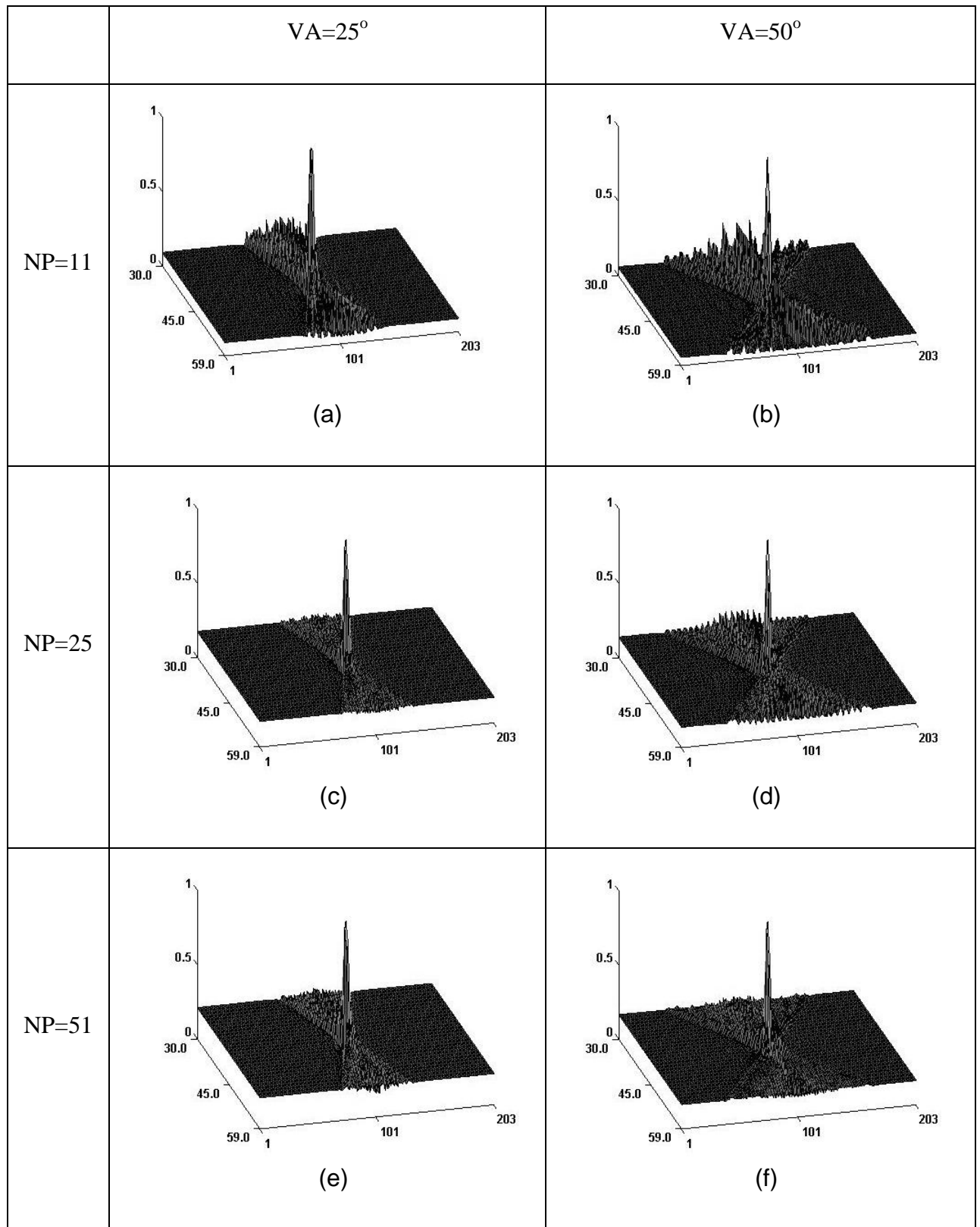


Figure 48. Impulse responses of wire simulation with SART reconstruction.

Normalized pixel intensities in the spatial domain are displayed as the three-dimensional impulse response plots. The  $x$  axis represents the sequential numbers of the reconstruction planes that are parallel to the detector surface plate as described in Figure 43. The  $y$  axis represents the pixel locations of the column containing simulated wire on the reconstruction plane that is located at the center of the simulated wire space (the wire spreads from  $z=30$  mm through  $z=59$  mm. The center is 45 mm away from the detector face plate). The  $z$  axis represents normalized pixel's intensities.

One can see that with smaller number of projection images, out-of-plane artifacts are obvious in all  $NP=11$  images by showing tails along  $x$  axis. With a bigger number of projection images, the out-of-plane artifacts are suppressed to a much lower level and sharper in-plane peaks occurs. In the results of Figure 45(e) and 48(e), because of the very big projection number and narrow view angle, the slight oscillation occurs which should be avoided. With wider angle of  $VA=50^\circ$ , the out-of-plane artifacts spread to wider range correspondingly. View angle and projection image number can benefit each other but it may bring more artifacts with wide view angle and small projection view number.

In summary, when number of projection images increases, algorithms performed better by showing sharper in-plane performance. MLEM shows better performance in removing the out-of-plane blur.

## CHAPTER 5

### RELATIVE NEQ(F) ANALYSIS OF A MULTI-BEAM PARALLEL DIGITAL BREAST TOMOSYNTHESIS PROTOTYPE SYSTEM

The noise-equivalent quanta NEQ(f) describes the minimum number of X-ray quanta required to produce a specified signal to noise ratio (SNR). It has an important physical meaning as it describes how well a low-contrast structure can be detected in a uniform noise-limited image by the ideal observer which is an indication of what can be visualized by a human observer under specified conditions (Wiki 2011). NEQ(f) has been accepted as measurement metrics of medical imaging systems. It is dependent on the overall system performance, including radiation dosage, imaging configuration, pulse width, detector and image reconstruction algorithm.

In frequency domain, the MTF describes the signal response of a system at a given frequency and the NPS describes the amplitude variance at a given frequency. The ratio of these factors presents information about the maximum available SNR as a function of frequency.

A set of optimization experiments based NEQ(f) analysis were used to evaluate our multi-beam parallel digital breast tomosynthesis system and find the optimal system design including reconstruction algorithms and imaging configurations. In our current digital breast tomosynthesis system, it has 29 X-ray beam sources. A digital flat-panel detector with the pixel pitch of 140  $\mu\text{m}$  was integrated into the prototype system. The image size is 2048 $\times$ 1664. Two imaging configuration modes were used: (1) View angle =14 $^\circ$ , number of projection images = 15 (Mode code: VA14NP15); (2) View angle =28 $^\circ$ , number of projection images =15 (Mode code: VA28NP15).

## 5.1. MTF

The Modulation Transfer Function (MTF) is used to analyze the resolution of imaging system in frequency domain. Technically, the “resolution” of a system is the minimum distance that two objects can be distinguished. In practice, an impulse function can be simulated to evaluate the response of the system or algorithm to be investigated. (Dobbins 2000).

The MTF is a handy descriptor of system spatial response because the stages of system response can be considered as “filters” as described in our linear system analysis in Section 4.1. Furthermore, the composite MTF of a tomosynthesis imaging system is the product of the MTFs coming from all individual stages including both image acquisition and image reconstruction (Chen, 2007c). In this section, we call the MTF from image acquisition as projection MTF  $MTF_{proj}(f)$  and the MTF from image reconstruction as reconstruction MTF  $MTF_{recon}(f)$ .

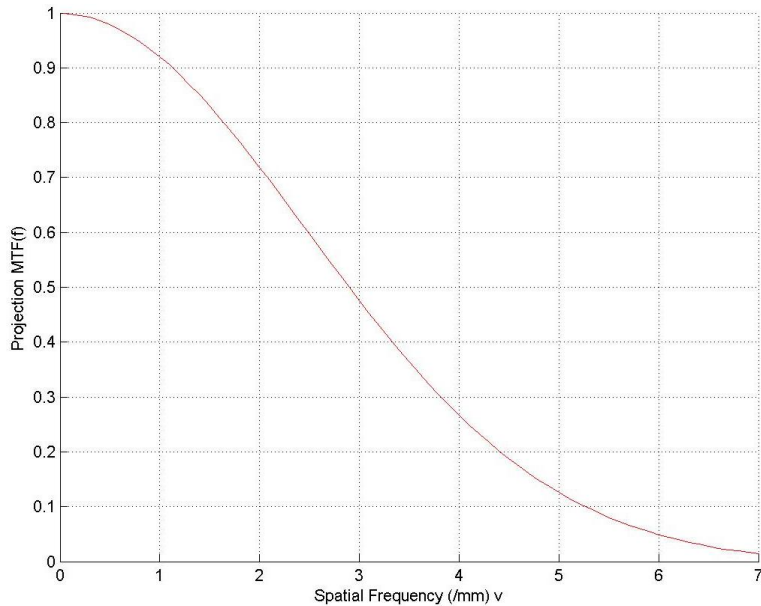


Figure 49. Projection MTF of our multi-beam parallel digital breast tomosynthesis system.

### 5.1.1. Projection MTF(f)

Let's discuss projection MTF as our first step. Two methods, slit method and edge method, are recommended (Dobbins 2000). The projection MTF of our breast tomosynthesis prototype system was tested with a slit method (Fujita 1992). Figure 50 shows the Projection MTF curve (Qian et al 2012).

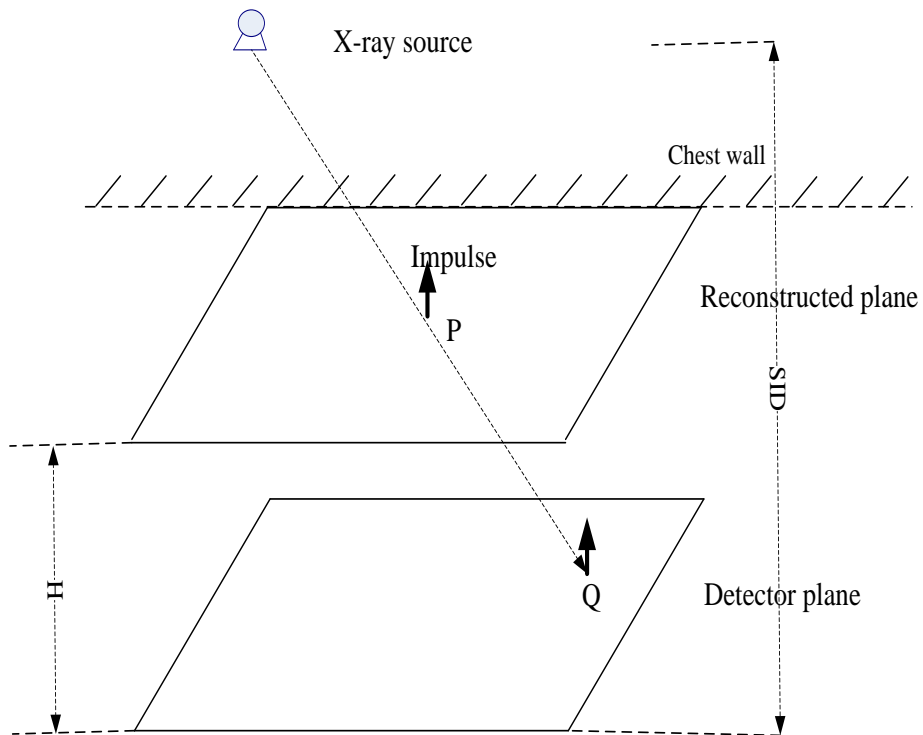


Figure 50. Impulse simulation based on ray-tracing method.

### 5.1.2. Reconstruction MTF

Reconstruction MTF presents the spatial frequency response with respect to different imaging configurations and reconstruction algorithms. A point spread function method with simulated impulse function as a standard signal input was used to test the reconstruction MTF(Chen, 2007c). The delta function (impulse) at location  $P$  was projected onto the detector at location  $Q$  when the X-ray source is located at the specific position.

Figure 50 shows the impulse simulation based on ray-tracing method. Tomosynthesis dataset of projection images of a single delta function at defined height of  $H$  above the detector was computer simulated.

The reconstruction MTF can be calculated as the Fourier Transform of the impulse response along the tube's alignment direction. It varies with the location of the simulated impulse. In our experiments, two areas were computer simulated with the imaging configuration of the prototype system. The first area "away-from-chest-wall" was used to mimic the object away from the chest wall. The second area "near-chest-wall" was used to mimic the object near chest wall. In each area, 25 impulses were evenly placed inside the pixel. Ray-tracing method was used to generate the projection images. The images were then reconstructed. In  $MTF_{recon}(f)$  calculation, the slice images, 45 mm above the detector, which was also the in-focus plane of the impulses, were selected. FFT transform of the images were used to extract frequency components and form the MTF curves.

Here we illustrate the experiments with the imaging configuration  $VA=14^\circ$ ,  $NP=15$ . Figure 51 shows the area locations on the reconstructed plane. Figure 52

shows the impulse locations inside the pixels. Figure 53 shows the  $MTF_{recon}(f)$  curves of BP reconstruction algorithm for the simulations with different impulse locations. Blue curves are the  $MTF_{recon}(f)$  results for different impulse locations. Red curves are the average  $MTF_{recon}(f)$  for the corresponding areas. Further comparisons will be conducted in the subsection “Relative NEQ analysis”.

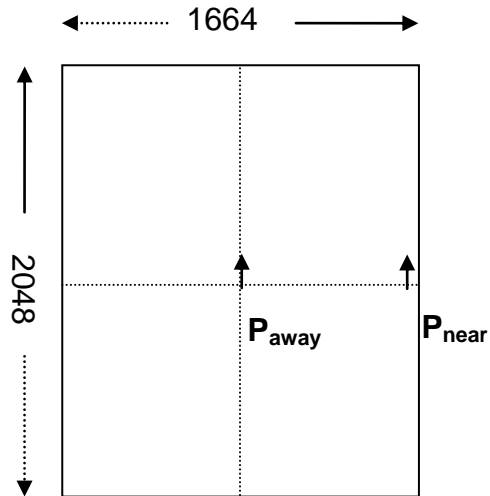


Figure 51. Area locations of simulated impulses for reconstruction MTF(f).

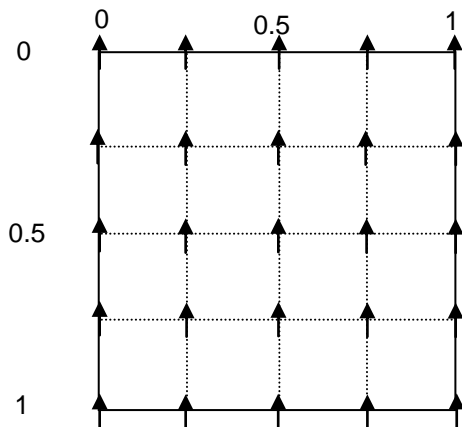
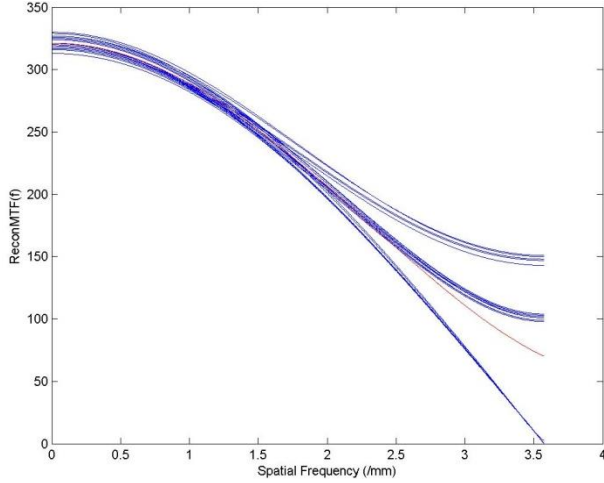
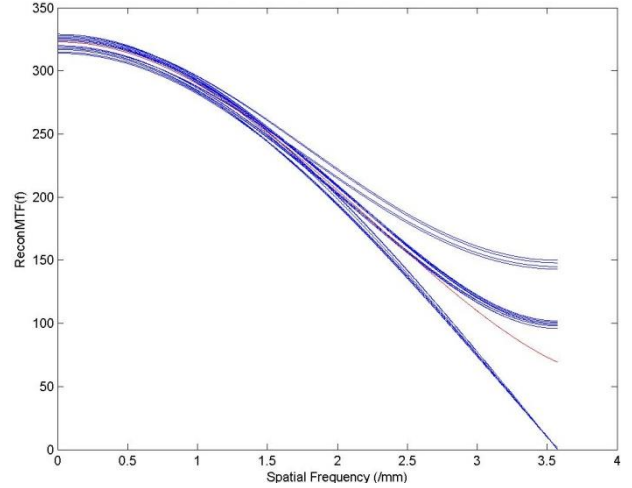


Figure 52. Impulse locations inside one pixel for two different area modes.



(a) away-from-chest-wall.



(b) near-chest-wall

Figure 53. Reconstruction MTF curves of BP in different experiments with different impulse locations. Blue curves are from different impulses. Red curves are the average.

## 5.2. NPS

The NPS is one of the most common metrics characterizing the noise property of imaging systems. The frequency-dependent NPS( $f$ ) is defined as the variance per frequency bin of a stochastic signal in the spatial frequency domain (Dobbins 2000). It can be directly computed from the squared Fourier amplitude of 2D imaging data by (Dobbins 2000):

$$\begin{aligned}
 NPS(w_x, w_y) &= \lim_{M, N \rightarrow \infty} (MN \Delta X \Delta Y) \langle |FT[I(x, y) - \bar{I}]|^2 \rangle \\
 &= \lim_{M, N \rightarrow \infty} \lim_{K \rightarrow \infty} \frac{MN \Delta X \Delta Y}{K} \sum_{k=1}^K |FT[I(x, y) - \bar{I}]|^2 \\
 &= \lim_{M, N, K \rightarrow \infty} \frac{\Delta X \Delta Y}{K \cdot MN} \sum_{k=1}^K \left| \sum_{i=1}^M \sum_{j=1}^N [I(x_i, y_j) - \bar{I}] e^{-2\pi i(w_x x_i + w_y y_j)} \right|^2
 \end{aligned}$$

(Eq. 32)

where,  $I(x_i, y_i)$  is the image intensity at the pixel location  $(x_i, y_i)$ .  $\bar{I}$  is the global mean intensity.  $w_x$  and  $w_y$  are the spatial frequencies conjugate to x and y axes.  $M$  and  $N$  are the numbers of pixels in the x and y directions of the digital image.  $\Delta X$  and  $\Delta Y$  are the pixel spacings in the x and y directions. And  $K$  is the number of ROIs used for analysis.

According to this equation, it is easy to implement a mean-subtracted NPS(f) measurement method. It has formed a methodology to assess the noise response of the system. In this methodology, noise propagation was evaluated by investigating the reconstructed slice images of a breast tissue equivalent phantom with the prototype system. In our experiments, a phantom, 40 mm thick, was placed on the surface of the detector. For each reconstruction algorithm, all the slice images with 1 mm slice thickness were reconstructed to cover the entire breast phantom.

In NPS calculation, regions of interest (ROIs) with the size of 1024\*1024 pixels were cut from the reconstructed planes with the same height above the detector. Each ROI was evenly divided into 8 blocks with a size of 128\*128 pixels. For each block, a line curve fitting through the ensemble-averaged NPS estimate was used to obtain an approximation to the greatest slope of the true NPS. Finally, we extracted the frequency components from each block and formed the smoothed NPS curves. Figure 54 illustrates the NPS curves of BP reconstruction algorithm by ten experiments. Blue curves are from the ten experiments. Red curve is the average. Further comparisons will be conducted in the subsection "Relative NEQ analysis".

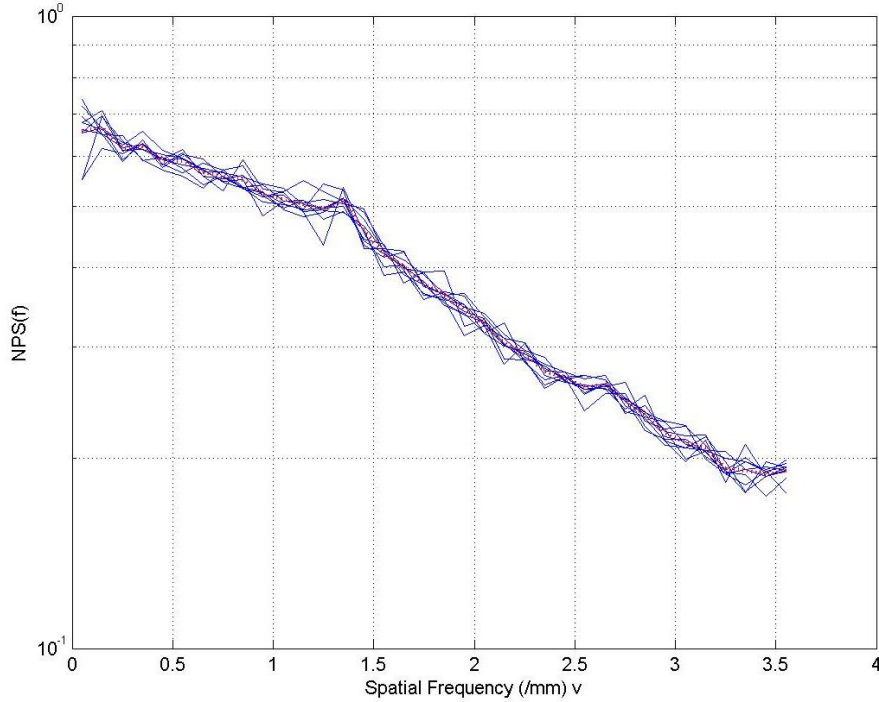


Figure 54. NPS curves of BP reconstruction with the imaging configuration VA14NP15.  $v$  is the direction of X-ray tube alignment.

### 5.3. RELATIVE NEQ ANALYSIS

A relative NEQ( $f$ ) measurement method is used in our experiments. The relative NEQ( $f$ ) combines the modulation transfer function (MTF) of signal performance and the noise power spectrum (NPS) of noise characteristics. The relative NEQ( $f$ ) can be expressed as

$$NEQ(f) = \frac{MTF_{proj}^2 \cdot MTF_{recon}^2}{NPS(f)} \quad (\text{Eq. 33})$$

The  $MTF_{recon}(f)$  is the relative MTF with the specific image reconstruction algorithm and imaging configuration parameters. The  $MTF_{proj}(f)$  is the measured MTF of the imaging system. The NPS ( $f$ ) is the mean subtracted NPS on the same reconstruction plane.

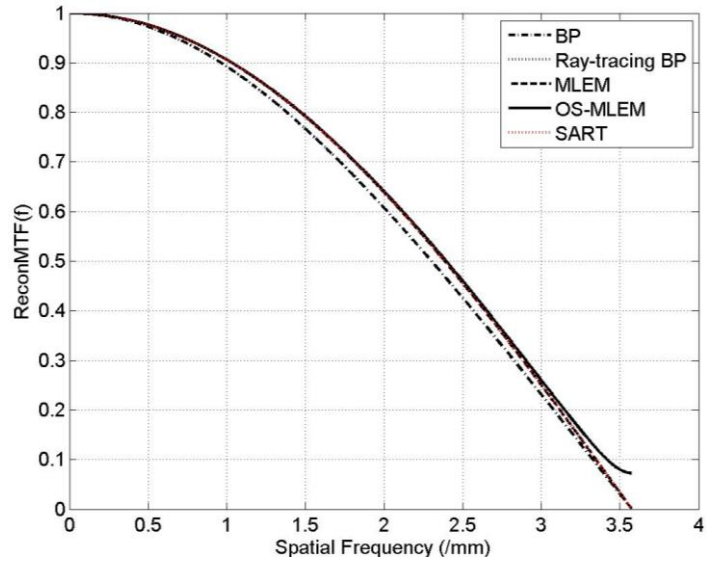
A complete analysis about different reconstruction algorithms and imaging configurations were conducted to form a systematic optimization methodology.

### 5.3.1 Relative NEQ(f) analysis for different reconstruction algorithms

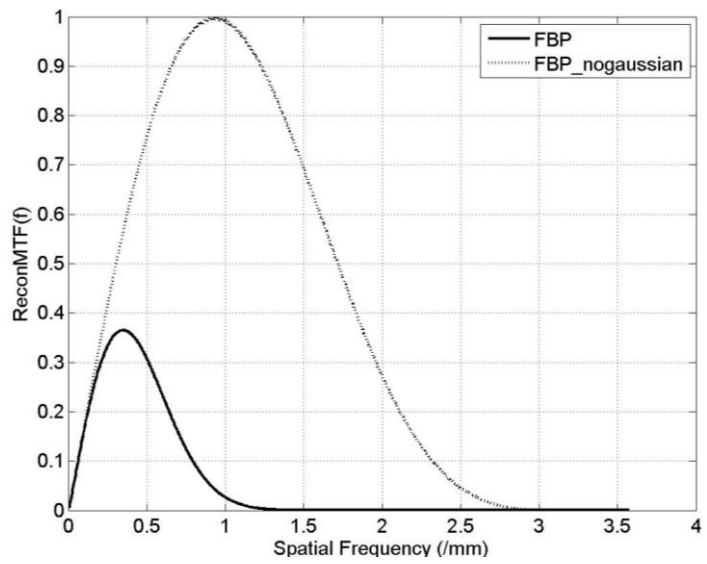
#### **Reconstruction MTF(f)**

Figures 55(a) illustrate normalized reconstruction MTFs of BP, Ray-tracing BP, MLEM, OS-MLEM and SART with the imaging configuration of VA14NP15 for simulating impulses. Based on the normalized  $MTF_{Recon}(f)$  analysis, point-by-point BP has the least high-frequency response. OS-MLEM has the maximal high frequency. The difference between iterative reconstruction algorithms is very small. According to the figure, OS-MLEM shows better high-frequency response. It may produce sharper edges in the imaging application.

Figure 55(b) shows reconstruction MTF curves of two FBP versions, FBP and FBP\_nogaussian. The difference is that there is no Gaussian filter in FBP\_nogaussian.. We can find high-frequency response was greatly compressed after we used Gaussian low-pass filter.



(a)



(b)

Figure 55. Reconstruction MTF (f) of different reconstruction algorithms. (a) BP, Ray-tracing BP, MLEM, OS-MLEM and SART. (b) FBP and FBP\_nogaussian.

## **NPS(f)**

In Figure 56, the normalized mean-subtracted NPS(f) curves for all the reconstruction algorithms are presented. We can observe some interesting facts:

(1) FBP has high dynamic range. It has the highest low-frequency noise, but least high-frequency noise. An assumption is that in our FBP implementation, one high-pass filter and two low-pass filters are applied, including ramp filter (a high-pass filter), Ham filter (a low-pass filter) and Gaussian filter (a low-pass filter). The two low-pass filters greatly suppress high-frequency noise.

(2) Both OS-MLEM and SART have the similar high-frequency noise. Their noise levels are higher than MLEM. Their iteration behavior of projection-by-projection update in OS-MLEM and SART greatly speed up the convergence. Iterative procedure has the effect of high-pass filter, so it increased the high-frequency noise.

(3) Ray-tracing BP and point-by-point BP have quite similar noise responses. Ray-tracing BP has a little lower NPS response.

(4) MITS has its unique noise propagation property. In low frequency, it has smaller noise response than iterative algorithms but has a little bigger noise response than MLEM.

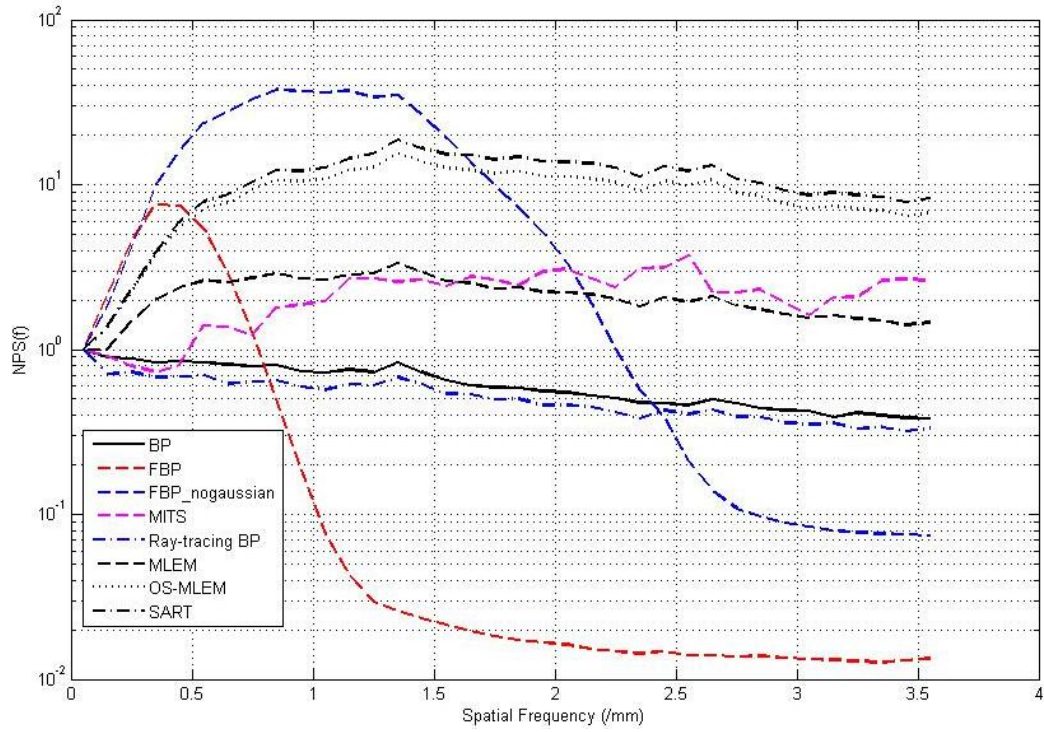


Figure 56. Curves of mean-subtracted NPS(f) analysis for different reconstruction algorithms.

## Relative NEQ(f)

Figure 57(a) shows the relative NEQ(f) curves of ray-tracing-based reconstruction algorithms, including ray-tracing BP, MLEM, OS-MLEM and SART with the same imaging configuration VA14NP15. It suggests that MLEM has better high-frequency efficiency. OS-MLEM provides a little better NEQ(f) response than SART. It deserves to apply OS-MLEM considering that it greatly saves running time.

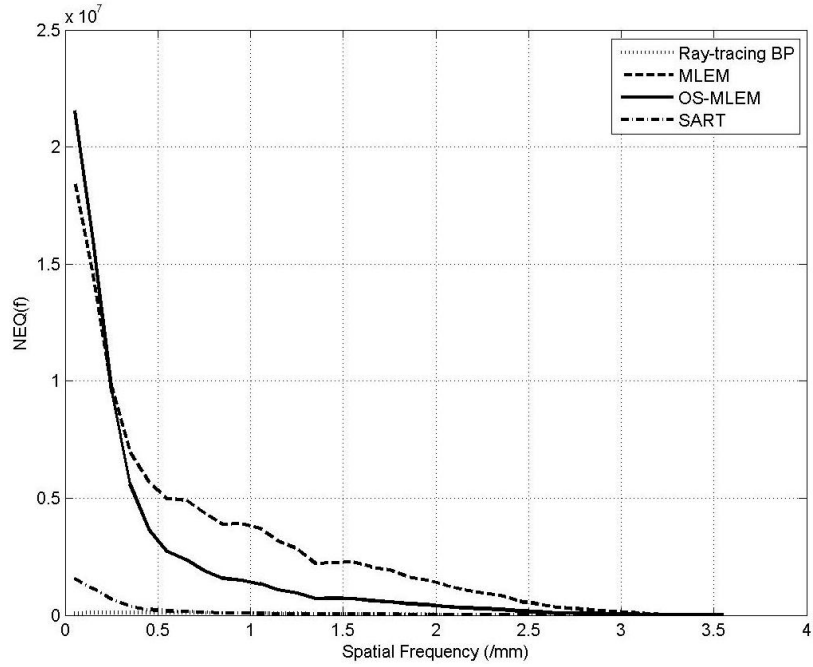
Figure 57(b) compare the NEQ(f) of two FBP versions of FBP and FBP\_nogaussian. Based on the curves, Gaussian filter decreases the high-frequency efficiency of incident X-ray.

### 5.3.2 Relative NEQ(f) analysis for different imaging configurations

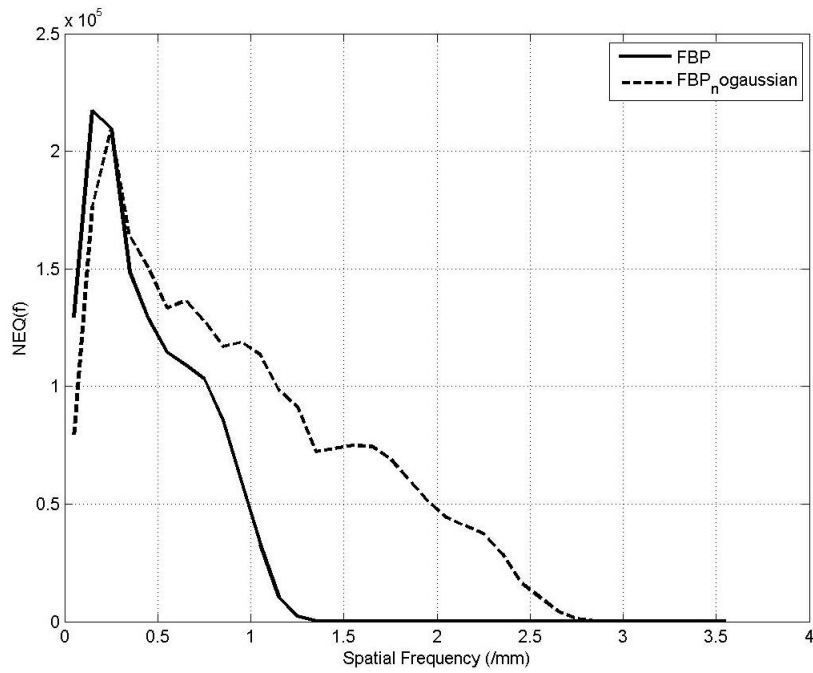
Two groups of imaging configurations were tested for our relative NEQ(f) analysis. For each imaging configuration, ten datasets of NPS phantom experiments were acquired. The dose was approximately 96 mAs for each set of data. The tube potential was 30 kVp. Figures 58 through 61 shows the ReconMTF(f), NPS(f) and NEQ(f) results of BP, FBP, OS-MLEM and SART reconstruction algorithm respectively. Two imaging configurations were tested: VA14NP15 and VA28NP15.

For reconstruction MTF(f), two reconstruction MTF(f) curves of BP for different imaging configurations are almost merged while the difference for other algorithms is bigger. Especially, in Figure 61, with the increase of view angle, frequency response is bigger so in FBP big view angle will contribute to the conspicuity of objects.

The NEQ(f) curves of two imaging configurations in BP and FBP are intertwined. There is no obvious trend. However, in both OS-MLEM and SART, big view angle benefits the low-frequency NEQ(f) response.



(a)



(b)

Figure 57. NEQ (f) of different reconstruction algorithms. (a) MLEM, OS-MLEM and SART. (b) FBP and FBP\_ogaussian.

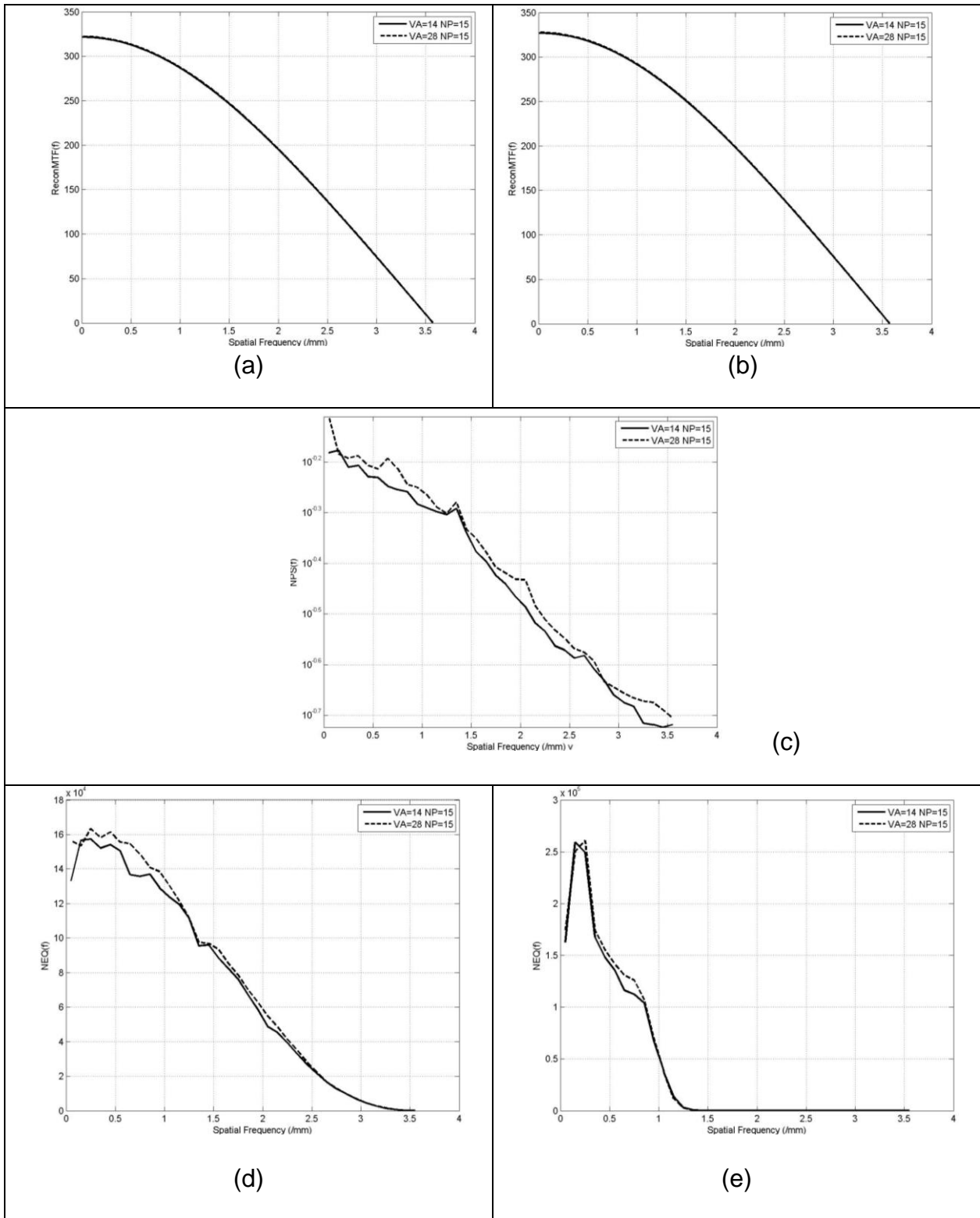


Figure 58. Relative NEQ(f) of BP reconstruction with different imaging configurations. (a) Reconstruction MTF of the mode away-from-chest-wall. (b) Reconstruction MTF of the mode near-chest-wall. (c) NPS. (d) NEQ of the mode away-from-chest-wall. (e) NEQ of the mode near-chest-wall.

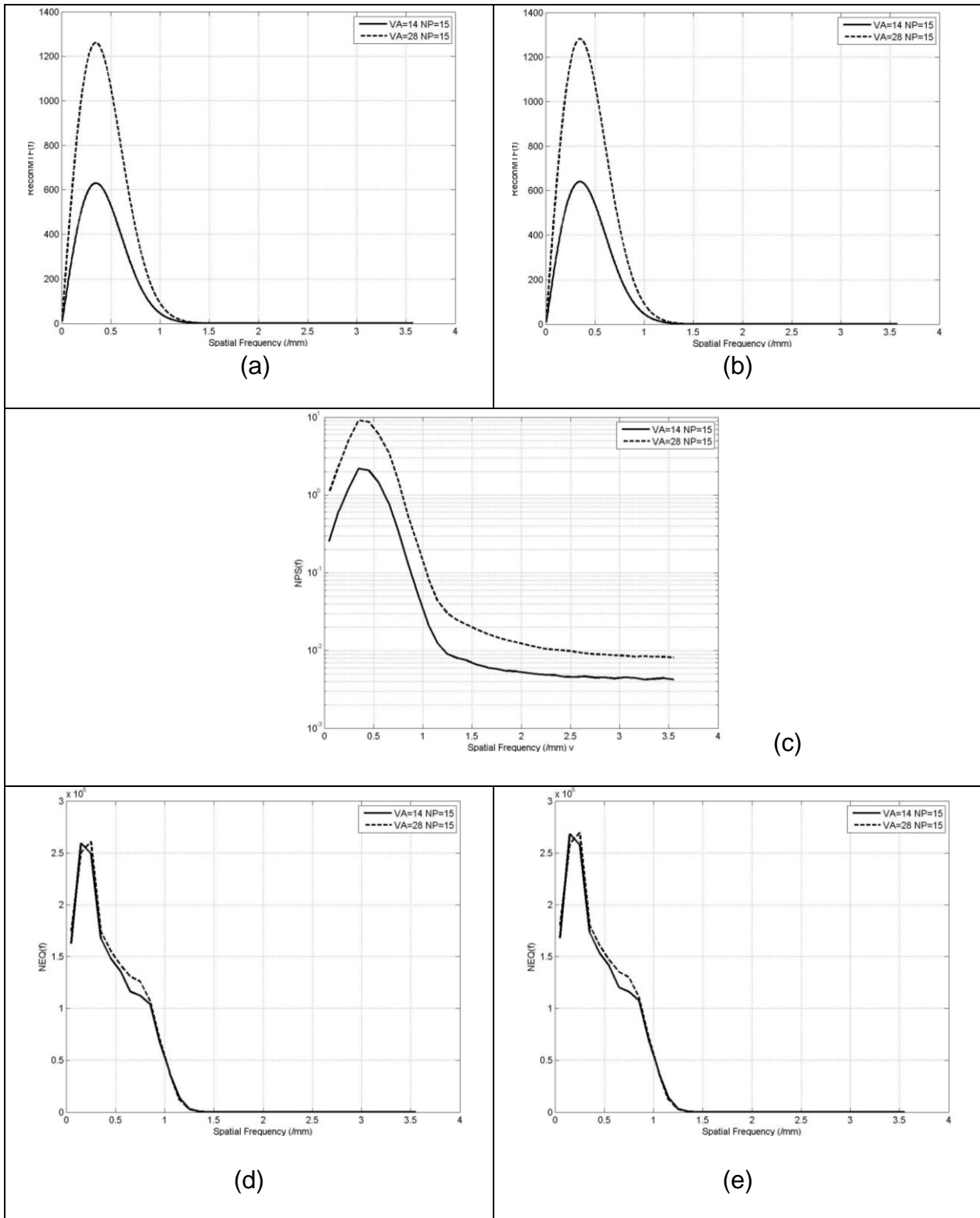


Figure 59. Relative NEQ(f) of FBP reconstruction with different imaging configurations. (a) Reconstruction MTF of the mode away-from-chest-wall. (b) Reconstruction MTF of the mode near-chest-wall. (c) NPS. (d) NEQ of the mode away-from-chest-wall. (e) NEQ of the mode near-chest-wall.

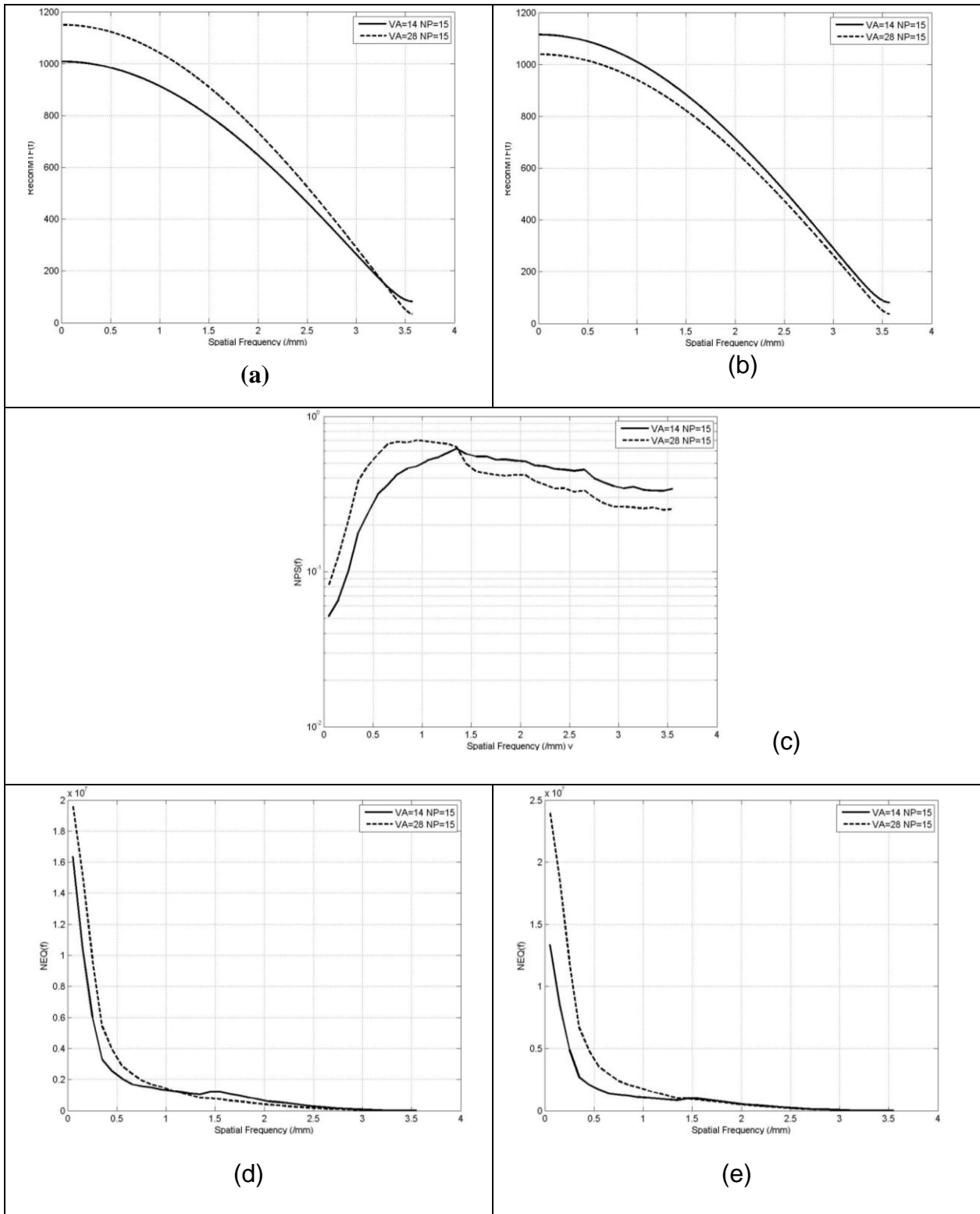


Figure 60. Relative NEQ(f) of OS-MLM reconstruction with different imaging configurations. (a) Reconstruction MTF of the mode away-from-chest-wall. (b) Reconstruction MTF of the mode near-chest-wall. (c) NPS. (d) NEQ of the mode away-from-chest-wall. (e) NEQ of the mode near-chest-wall.

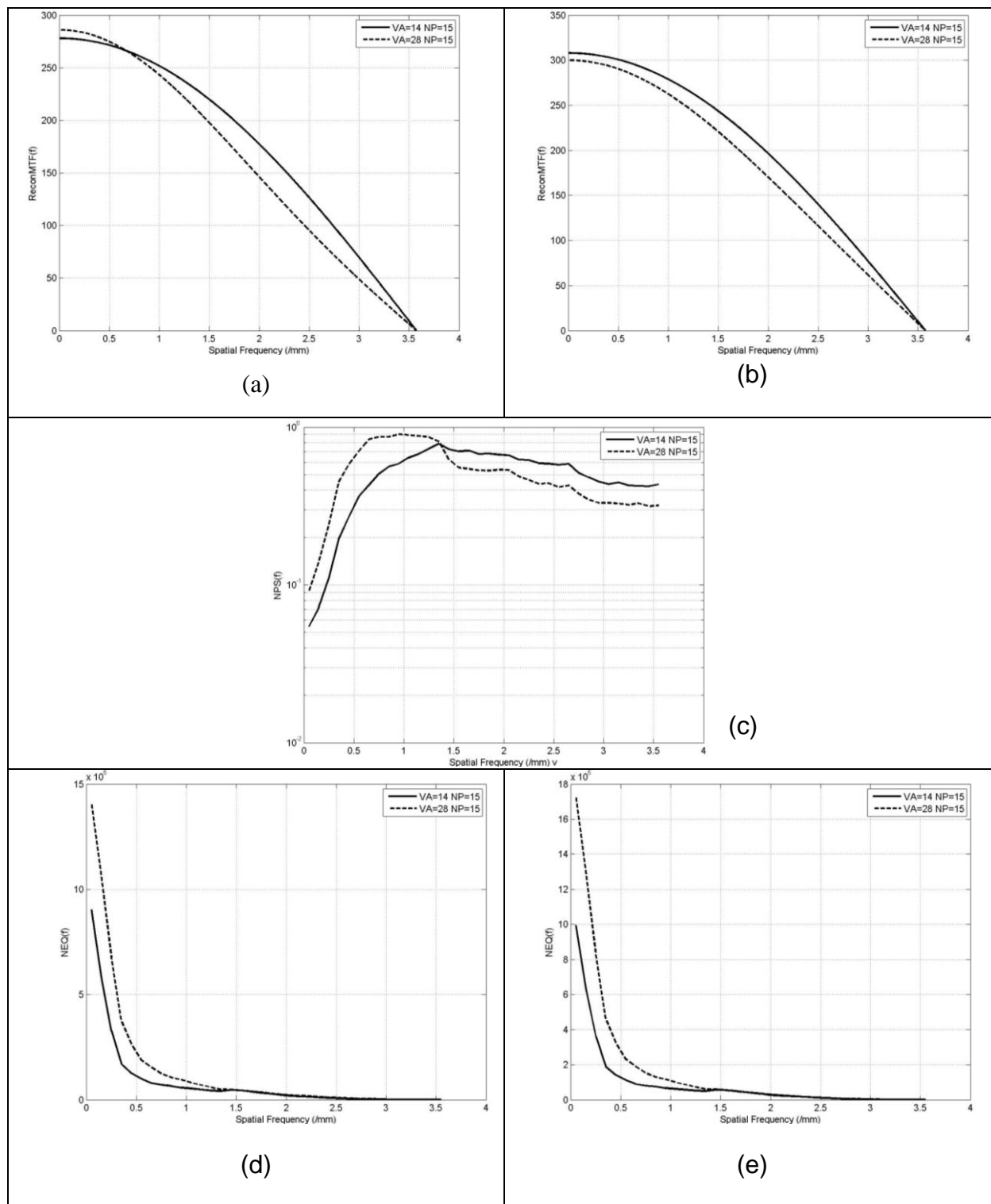


Figure 61. Relative NEQ(f) of SART reconstruction with different imaging configurations. (a) Reconstruction MTF of the mode away-from-chest-wall. (b) Reconstruction MTF of the mode near-chest-wall. (c) NPS. (d) NEQ of the mode away-from-chest-wall. (e) NEQ of the mode near-chest-wall.

## CHAPTER 6

### CONCLUSIONS

Most of breast tomosynthesis prototype systems are built upon the current digital mammography system design. The X-ray tube typically moves along an arc path above the detector. With a new nanotechnology enabled fast-speed multi-beam parallel breast tomosynthesis prototype system, it may potentially reduce the motion blur associated with X-ray tube's movement of typical prototype systems. We anticipate that this optimization project will be greatly helpful to improve digital breast tomosynthesis technology for early breast cancer detection. We were dedicated to working on image reconstruction and image configurations to optimize the new digital breast tomosynthesis prototype system.

Representative image reconstruction algorithms, including mathematical reconstruction methods, filter-based reconstruction methods, statistical reconstruction methods and algebraic reconstruction methods, were reviewed and some of them were improved in our design. A fast MLEM reconstruction algorithm was put forward. It can provide good image quality with less running time. Besides, two statistical reconstruction variants of BP were used to improve the performance of standard point-by-point BP reconstruction.

Combined with our multi-beam parallel prototype systems, the reconstruction algorithms were capable of providing three-dimensional information of the objects. Furthermore, the performance of the prototype system with different reconstruction algorithms and imaging configurations was measured by image quality. Contrast to

noise ratio (CNR) and artifact spread function (ASF) were used to evaluate image quality.

Four optimization methodologies were proposed to improve the system design. A linear analysis method modelling the signal propagation was used to evaluate frequency characterization of blurring-out reconstruction algorithms. Computer simulations of sphere and wire were used to compare reconstruction algorithms and imaging configurations. In frequency domain, noise equivalent quanta (NEQ(f)), composed of noise power spectrum (NPS(f)) and modulation transfer function (MTF(f)), was investigated.

The optimization experiments suggest that

- (1) Statistical reconstruction algorithms have better out-of-plane blurring removal;
- (2) Out-of-plane blurring can be reduced with the increase of view angle;
- (3) In-plane sharpness of objects will increase with the increase of number of projection images.

This is a continuing project which is expected to provide a new promising marketable breast imaging device. Effort is being put on the clinical experiments to evaluate with real human subjects.

## REFERENCES

- Altekruse, S. F., Kosary, C.L., Krapcho, M., et al. (2010). SEER Cancer Statistics Review, 1975–2007. Bethesda, MD: National Cancer Institute, 2010.  
<http://www.cancer.gov/cancertopics/factsheet/detection/probability-breast-cancer>.
- American Cancer Society. (2012a). Survival rates for breast cancer. Retrieved June 10, 2012, from: <http://www.cancer.org/Cancer/BreastCancer/OverviewGuide/breast-cancer-overview-survival-rates>.
- American Cancer Society. (2012b). For Women Facing a Breast Biopsy. Retrieved June 10, 2012, from:  
<http://www.cancer.org/Treatment/UnderstandingYourDiagnosis/ExamsandTestDescriptions/ForWomenFacingaBreastBiopsy/>.
- Andersen, A.H. , Kak, A.C.. (1984). Simultaneous algebraic reconstruction technique (SART): a new implementation of the ART algorithm. *Ultrasound Imaging*, 6: 81–94.
- Andersen, A. H. (1989). Algebraic reconstruction in CT from limited views. *IEEE Trans. On Medical Imaging*, 8 (1): 50-55.
- Andrew, R.B. (2002). *Intorduction to Biomedicla Imaing*. IEEE Press Series on Biomedical Engineering.
- Bachar, G., Siewerdsen, J.H., Daly, M.J., Jaffray, D.A., Irish, J.C. (2007). Image quality and localization accuracy in C-ary tomosynthesis-guided head and neck surgery. *Med. Phys.* 34(12): 4664-4677.

- Badea, C., Kolitsi, Z. and Pallikarakis, N. (2001). A 3D imaging system for dental imaging based on digital tomosynthesis and cone beam CT. *Proc. of the International Federation for Medical and Biological Engineering 2*: 739-741.
- Balla, A., Zhou, W., Chen, Y. (2010). Impulse Response Characterization of Breast Tomosynthesis Reconstruction with Parallel Imaging Configurations. *Proc. SPIE*, 76225K.1-8.
- Barrett, H.H., Myers K.J. (2004). *Foundation of Image Science*. John Wiley & Sons. Hoboken, New Jersey.
- Bassett, L.W., Jackson, V.P., Fu, K.L., Fu, Y.S. (2005) *Diagnosis of Diseases of the Breast*. 2nd ed, Elsevier Saunders, Philadelphia, Pennsylvania.
- Blue Cross Blue Shield of Rhode Island. (2012). Medical Coverage Policy Digital Breast Tomosynthesis. Available:  
[https://www.bcbsri.com/sites/default/files/polices/Digital\\_Breast\\_Tomosynthesis.pdf](https://www.bcbsri.com/sites/default/files/polices/Digital_Breast_Tomosynthesis.pdf).
- BreastCancer.org. (2012). Stages of Breast Cancer. Retrieved June 10, 2012, from:  
<http://www.breastcancer.org/symptoms/diagnosis/staging.jsp>.
- Chen, Y., Lo, J. Y. and Dobbins, J. T., III. (2004). *Matrix Inversion Tomosynthesis (MITS) of the Breast: Preliminary Results*. RSNA 90<sup>th</sup> Scientific Assembly.
- Chen, Y., Lo, J. Y. and Dobbins, J. T., III. (2007a). Importance of point-by-point back projection (BP) correction for isocentric motion in digital breast tomosynthesis: Relevance to morphology of microcalcifications. *Med. Phys.* 34(10): 3885-3892.
- Chen, Y., Lo, J. Y., Ranger, N. T., Samei, E., Dobbins, J. T., III. (2007b). Methodology of NEQ(f) analysis for optimization and comparison of digital breast

- tomosynthesis acquisition techniques and reconstruction algorithms. *Proc. SPIE* 6510: 65101-1.
- Chen, Y. (2007c). Digital breast tomosynthesis (DBT) – a novel imaging technology to improve early breast cancer detection: implementation, comparison and optimization. PhD diss., Duke University, 2007.
- Chen, Y., Zhou, W., Yang, G., Lu, J.P., and Zhou O. (2009). Breast tomosynthesis reconstruction with a multi-beam x-ray source. *Proc. SPIE* 7258, 725859-8 (2009).
- Chen, Y., Zhou, W., Dobbins, III J. T. (2011). Fourier-Domain Methods for Optimization of Tomosynthesis (NEQ). book chapter, in *Tomosynthesis Imaging*, ed. I. Reiser and S. Glick, Taylor & Francis, 2011 (Accepted).
- CIRS Company. (2010). Available at: <http://www.cirsinc.com/pdfs/013cp.pdf>.
- Dobbins, J. T., III, Powell, A. O. and Weaver, Y. K. (1987). Matrix inversion tomosynthesis: Initial image reconstructions. *Abstract Summaries of the RSNA* 165(P): 333.
- Dobbins, J. T., III. (1990). *Matrix Inversion Tomosynthesis improvements in longitudinal x-ray slice imaging*. U.S. Patent #4,903,204. Assignee: Duke University.
- Dobbins, J. T., III. (2000). Image quality metrics for digital systems. In *Handbook of medical imaging, Volume 1. Physics and Psychophysics*, ed. J. Beutel, H. L. Kundel, and R. L. Van Metter, 161-222. SPIE.
- Dobbins, J. T., III, Godfrey, D. J. (2003). Digital X-ray tomosynthesis: current state of the art and clinical potential. *Phys. Med. Biol.* 48: 65-106.

- Dobbins, J.T., Samei E., Ranger N.T., Chen Y. (2006). Intercomparison of methods for image quality characterization. II. Noise power spectrum. *Med. Phys.* 33(5): 1466-1475.
- Erdogan, H., Gualtieri, G., Fessler, J.A. (1998). An Ordered Subsets Algorithms for Transmission Tomography. *Proc. IEEE Nuc. Sci. Symp. Med. Im. Conf.*
- Fujita et al. (1992). Simple Method for Determining the Modulation Transfer Function in Digital Radiography. *IEEE Trans Med Imaging*, 1992. 11(1).
- Godfrey, D. J., Warp, R. L. and Dobbins, J. T., III. (2001). Optimization of matrix inverse tomosynthesis. *Proc. SPIE* 4320: 696-704.
- Godfrey, D. J. and Dobbins, J. T., III. (2002). Optimization of matrix inversion tomosynthesis via impulse response simulations. *RSNA 88<sup>th</sup> Scientific Assembly.*
- Godfrey, D. J., Rader, A. and Dobbins, J. T., III. (2003). Practical strategies for the clinical implementation of matrix inversion tomosynthesis. *Proc. SPIE* 5030: 379-390.
- Godfrey, D. J., McAdams, H. P., Dobbins, J. T., III. (2006). Optimization of the Matrix Inversion Tomosynthesis (MITS) impulse response and modulation transfer function characteristics for chest imaging. *Med. Phys.* 33(3): 655-667.
- Ghosh Roy D.N., Kruger R.A., Yih B., et al. (1985). Selective plane removal in limited angle tomographic imaging. *Med Phys.* 1985;12(1):65Y70.
- Gonzalez, R.C., Woods, R.E. (2008). *Digital Image Processing.* Prentice Hall.
- Grant, D. G. (1972). Tomosynthesis: a three-dimensional radiographic imaging technique. *IEEE Transactions on Biomedical Engineering.* BME-19: 20-28.

- Guimarães, L.T.G., Schiabel, H., Stemberg, D.R.M. (2009). Computer Simulation in Evaluating the Attenuation Coefficients Influence on Mammography Images Contrast. IFMBE Proceedings, 2009, Volume 25/2, 454-457, DOI: 10.1007/978-3-642-03879-2\_128.
- Hologic Inc. (2012). Breast Tomosynthesis – Selenia Dimensions. Retrieved June 10, 2012, from: <http://www.hologic.com/en/breast-imaging/selenia-dimensions-tomosynthesis/>.
- Kopans, D.B. (1997). Breast Imaging. 2nd ed, Lippincott Williams and Wilkins, New York.
- Hayes, J.C. (2012). Studies suggest new value for digital breast tomosynthesis. Retrieved June 10, 2012, from: <http://www.diagnosticimaging.com/conference-reports/ecr2009/article/113619/1385655#>.
- Highnam, R., Brady, M. (1999). Mammographic Image Analysis. Kluwer Academic Publishers, Dordrecht, The Netherlands.
- Lange, K. and Carson, R. (1984). EM reconstruction algorithms for emission and transmission tomography. *Journal of Computer Assisted Tomography*. 8(2): 306-316.
- Lange, K and Fessler, J. A. (1995). Globally convergent algorithms for maximum a posteriori transmission tomography. *IEEE Transactions on Image Processing*. 4(10): 1430-1438.
- Lalush, D. S., Quan, E., Rajaram, R., Zhang, J., Lu, J., Zhou, O. (2006). Tomosynthesis reconstruction from multi-beam x-ray sources. Proceedings of 2006 IEEE International Symposium on Biomedical Imaging, 1180-1183.

- Lauritsch, G. and Haerer, W. (1998). A theoretical framework for filtered back-projection in tomosynthesis. *Proc. SPIE* 3338: 1127-1137.
- Li, J., Jaszczak, R.J., Greer, K.L. and Coleman, R.E. (1993). Implementation of an accelerated iterative algorithm for cone-beam SPECT. *Phys. Med. Biol.* **39**(643) [doi:10.1088/0031-9155/39/3/025](https://doi.org/10.1088/0031-9155/39/3/025).
- Maidment, A. D., Ullberg, C., Lindman, K., Adelöw, L., Egerström, J., Eklund, M., Francke, T., Jordung, U., Kristoffersson, T., Lindqvist, L., Marchal, D., Olla, H., Penton, E., Rantanen, J., Solokov, S., Weber, N. and Westerberg, H. (2006). Evaluation of a photon-counting breast tomosynthesis imaging system. *Proc. SPIE* 6142: 89-99.
- Matsuo, H., Iwata, A., Horiba, I. and Suzumura, N. (1993). Three-dimensional image reconstruction by digital tomo-synthesis using inverse filtering. *IEEE Trans. Med. Imaging* 12: 307-313.
- Mertelemeier, T., Orman, J., Haerer, W. and Dudam, M. K. (2006). Optimizing filtered backprojection reconstruction for a breast tomosynthesis prototype device. *Proc. SPIE* 6142: 131-142.
- National Cancer Institute. (2012). Breast Cancer Home Page. Retrieved June 10, 2012, from: <http://www.cancer.gov/cancertopics/types/breast>.
- Niklason, L. T., Christian, B. T., Niklason, L. E., Kopans, D. B., Castleberry, D. E., Opsahl-Ong, B. H., Landberg, C. E., Slanetz, P. J., Giardino, A. A., Moore, R., Albagli, D., DeJule, M. C., Fitzgerald, P. F., Fobare, D. F., Giambattista, B. W., Kwasnick, R. F., Liu, J., Lubowski, S. J., Possin, G. E., Richotte, J. F., Wei, C. Y.,

- Wirth, R. F. (1997). Digital tomosynthesis in breast imaging. *Radiology* 205: 399-406.
- Nishikawa, R.M. (2011). The fundamentals of MTF, Wiener spectra, and DQE.  
Retrieved September 28, 2011, from:  
<http://www.aapm.org/meetings/99AM/pdf/2798-87374.pdf>.
- Park, J.M., Franken, Jr. E.A., Garg, M., Fajardo, L.L. , Niklason, L.T. (2007). Breast tomosynthesis: present considerations and future applications. *Radiographics*. 2007;27(Suppl 1):S231-240.
- Pisano, E.D., Yaffe, M.J., Kuzmiak, C.M. (2004). *Digital Mammography*. Lippincott Williams and Wilkins, Philadelphia.
- Qian, X., Tucker A., Gidcumb, E., Shan, J., Yang G., Calderon-Colon, X., Sultana, S., Lu, J., Zhou, O. (2012). High Resolution Stationary Digital Breast Tomosynthesis Using Distributed Carbon Nanotube X-Ray Source Array. *Medical Physics*. 39(4):2090-9.
- Radiological Society of North America Inc. (2012a). Breast Ultrasound. Retrieved June 10, 2012, from: <http://www.radiologyinfo.org/en/info.cfm?pg=breastus>.
- Radiological Society of North America Inc. (2012b). Breast MRI. Retrieved June 10, 2012, from: <http://www.radiologyinfo.org/en/info.cfm?pg=breastmr>.
- Radon, J. Über die bestimmung von funktionen durch ihrd intergralwerte l ängs gewisser mannigfaltigkeiten. (1917). *Ber. Verch Saechs. Akad. Wiss. Leipzig Math. Phys. Kl.* 69: 262-267.
- Rakowski, J. T. and Dennis, M. J. (2006). A comparison of reconstruction algorithms for C-arm mammography tomosynthesis. *Med. Phys.* 33(8): 3018-3032.

- Saunders, R. S. , Samei, E. (2003). A method for modifying the image quality parameters of digital radiographic images. *Med. Phys.* 30: 3006-3017.
- Saunders, R. S., Samei, E., Jesneck, J., Lo, J. Y. (2005). Physical characterization of a prototype selenium-based full field digital mammography detector. *Med. Phys.* 32(2): 588-599.
- Samei E., Ranger, N.T., Dobbins J.T., Chen, Y. (2006). Intercomparison of methods for image quality characterization. I. Modulation transfer function. *Med. Phys.* 33(5): 1454-1465.
- Siemens. (2010). Digital Breast Tomosynthesis (White Paper). Retrieved June 25, 2012, from:  
[http://www.medical.siemens.com/siemens/en\\_GB/rg\\_marcom\\_FBAs/files/news/2010\\_09\\_tomosynthesis/Whitepaper\\_DBT\\_Summary.pdf](http://www.medical.siemens.com/siemens/en_GB/rg_marcom_FBAs/files/news/2010_09_tomosynthesis/Whitepaper_DBT_Summary.pdf)
- Sprawls, P. (2012). Image Characteristics and Quality. Retrieved March 10, 2012, from:  
<http://www.sprawls.org/ppmi2/IMGCHAR/>.
- Stevens, G. M., Fahrig, R. and Pelc, N. J. (2001). Filtered backprojection for modifying the impulse response of circular tomosynthesis. *Med. Phys.* 28: 372-380.
- Suryanarayanan, S., Karellas, A., Vedantham, S., Glick, S.J., D'Orsi, C.J., Baker, S.P., Webber, R.L. (2000). Comparison of tomosynthesis methods used with digital mammography. *Academic Radiology*, 7(12): 1085-1097.
- Szepessy A. (2012). 7. Algebraic Reconstruction Algorithms. Retrieved June 10, 2012, from: <http://www.nada.kth.se/~szepessy/tomografi.pdf>.
- Warp, R. J., Godfrey, E. J. and Dobbins, J. T., III. (200). Applications of matrix inverse tomosynthesis. *Proc. SPIE* 3977: 376-383.

- Webb, A. (2003). Introduction to Biomedical Imaging. John Wiley & Sons, Inc.  
Hoboken, New Jersey.
- Wiki. (2011). Detective quantum efficiency. Retrieved September 24, 2011, from:  
[http://en.wikipedia.org/wiki/Detective\\_quantum\\_efficiency](http://en.wikipedia.org/wiki/Detective_quantum_efficiency).
- Wiki. (2012). Tomosynthesis. Retrieved June 14, 2012, from:  
<http://en.wikipedia.org/wiki/Tomosynthesis>.
- Wu, T., Moore, R. H., Rafferty, E. A. and Kopans, D. B. (2004). A comparison of reconstruction algorithms for breast tomosynthesis. *Med. Phys.* 9: 2636-2647.
- Wu, T., Stewart, A., Stanton, M., McCauley, T., Phillips, W., Kopans, D. B., Moore, R. H., Eberhard, J. W., Opsahl-Ong, B., Niklason, L., Williams, M. B. (2003). Tomographic mammography using a limited number of low-dose cone-beam projection images. *Med. Phys.* 30: 365-380.
- Yang, G., Rajaram, R., Cao, G., Sultana, S., Liu, Z., Lalush, D. S., Lu, J., Zhou, O. (2008). Stationary digital breast tomosynthesis system with a multi-beam field emission x-ray source array. *Proc. SPIE* 6913: 69131A.
- Zhang, Y., Chan, H., Sahiner, B., Wei, J., Goodsitt, M. M., Hadjiiski, L. M., Ge, J., Zhou, C. (2006). A comparative study of limited-angle cone-beam reconstruction methods for breast tomosynthesis. *Med. Phys.* 33(10): 3781-3795.
- Zhao, B., Zhao, W. (2008). Three-dimensional linear system analysis for breast tomosynthesis. *Med. Phys.* 35(12): 5219-5232.
- Zhao, W., Zhao, B., Hu Y.H. (2011). Latest advances in digital breast tomosynthesis. Retrieved September 24, 2011, from:  
<http://www.aapm.org/meetings/amos2/pdf/42-11930-81688-724.pdf>.

Zhou, W., Qian, X., Lu, J., Zhou, O., Chen, Y. (2010). Multi-beam X-ray source breast tomosynthesis reconstruction with different algorithms. Proc. SPIE 7622H: 1-8.

Ziedses des Plantes B. G. (1932). Eine neue methode zur differenzierung in der roentgenographie (planigraphie). Acta Radiologica 13:182-192.

VITA

Graduate School  
Southern Illinois University

Weihua Zhou

weihuazhou.ece@gmail.com

Wuhan University, China  
Bachelor of Engineering, Printing Engineering, June 2003

Wuhan University, China  
Master of Science, Computer Science, December 2007

Dissertation Paper Title:

Image reconstruction and imaging configuration optimization with a novel nanotechnology enabled breast tomosynthesis multi-beam X-ray system

Major Professor: Dr. Ying Chen

Publications:

1. Zhou, W., Chen, Y. Evaluation of Back-projection Methods for Breast Tomosynthesis Imaging Reconstruction. Submitted to *Journal of Digital Imaging*, 2012(under revision).
2. Zhou, W., Qian, X., Lu, J., Zhou, O., Chen, Y. Breast Tomosynthesis Parallel Imaging Configuration Optimization with a Nanotechnology Enabled Multi-beam X-ray Source. Submitted to *IEEE Transactions on Biomedical Engineering*, 2012(under review).
3. Cong, L., Zhou, W., Chen, Y. Effects of Slice Thickness Filter in Filtered Backprojection Reconstruction with the Parallel Breast Tomosynthesis Imaging Configuration. *Proc. IEEE-International Symposium on Intelligent Biological Medicine*, (2011).

4. Chen, Y., Zhou, W., Dobbins, J. T., III. Fourier-Domain Methods for Optimization of Tomosynthesis (NEQ). Book chapter, in *Tomosynthesis Imaging*, ed. I. Reiser and S. Glick, Taylor & Francis, 2011 (Accepted).
5. Rayford, C. E., II, Zhou, W., Chen, Y. Breast Tomosynthesis Imaging Configuration Analysis. *International Journal of Computational Biology and Drug Design*, Vol. 4(4), (2011).
6. Zhou, W., Xin, Q., Lu, J., Zhou, O., Chen, Y. Multi-beam X-ray Source Breast Tomosynthesis Reconstruction with Different Algorithms. *Proc. SPIE*, Vol. 7622, 7622H.1-8 (2010).
7. Chen, Y., Balla, A., Rayford, C. E. II, Zhou, W., Fang, J., Cong, L. Digital Tomosynthesis Parallel Imaging Computational Analysis with Shift and Add and Back Projection Reconstruction Algorithms. *International Journal of Computational Biology and Drug Design*, Vol. 3(4), 287-296 (2010).
8. Balla, A., Zhou, W., Chen, Y. Impulse Response Characterization of Breast Tomosynthesis Reconstruction with Parallel Imaging Configurations. *Proc. SPIE*, Vol. 7622, 76225K.1-8 (2010).
9. Chen, Y., Zhou, W., Yang, G., Lu, J., Zhou, O. Breast Tomosynthesis Reconstruction with a Multi-beam X-ray Source. *Proc SPIE*, Vol. 7258, 725859-8 (2009).
10. Zhou, W., Balla, A., Chen, Y. Tomosynthesis Reconstruction Using an Accelerated Expectation Maximization Algorithm with Novel Data Structure Based on Sparse Matrix Ray-Tracing Method. *International Journal of Functional Informatics and Personalised Medicine*, Vol. 1(4), 355-365 (2008).